ABSTRACT

CARBON NANOTUBE ELECTRONIC STRUCTURES AS ANTI-CORROSION COATINGS

by
Sreeya Sreevatsa

A new concept of corrosion prevention is considered in this study. Diode-like and transistor-like structures have been fabricated and analyzed in the study of ionic flow through the resulting potential barriers. The structures were made of functionalized carbon nanotubes. Carbon nanotubes are known for many remarkable properties among which is being chemically inert. Taking advantage of this property, a study of corrosion of steel was undertaken.

In the first case study, successive layers of functionalized carbon nanotubes were deposited to form *p-n* junctions on steel substrates. It was demonstrated that the corrosion was indeed impeded by the potential barrier formed across an electronic *p-n* junction. Potentiodynamic measurements, Raman spectroscopy, impedance measurements and scanning electron microscopy with energy dispersive x-ray spectroscopy were used to assess the corrosion process. It was found that the layer ordering (*p-n* or *n-p* with respect to the metal electrode) determined the corrosion rate in de-ionized (DI) water. Only temporary resistance was found in the presence of 3.5 wt% NaCl solution.

In the second case study, functionalized carbon nanotubes were drop-casted layer by layer to obtain transistor like *p-n-p* or *n-p-n* junctions. It was observed that the base voltage appreciably controlled the surface potential. The layer ordering determined the direction in which the surface potential of the steel substrate varied.

In the third case study, graphene was used as an intermediate layer between the steel substrate and the electronic *p-n* junctions. Graphene was also used as an intermediate layer between a steel substrate and a conductive polymer (polypyrrole) film. Here it was demonstrated that the monolayer thick graphene had a significant effect on the surface potential of the steel substrate. Also, graphene provided for an additional protection as determined by corrosion experiments.

In the fourth case study, bio-compatibility nature of carbon nanotubes was exploited. Single stranded deoxyribose nucleic acid was used to functionalize carbon nanotubes and obtain n-type semiconducting films. Electronic junctions were fabricated using these films as previously noted. The effect of bio-electronic *p-n* junctions was similar to the first case study, yet, by doing so, the potential for bio-ionic applications is made possible.

CARBON NANOTUBE ELECTRONIC STRUCTURES AS ANTI-CORROSION COATINGS

by
Sreeya Sreevatsa

A Dissertation
Submitted to the Faculty of
New Jersey Institute of Technology
and Rutgers, The State University of New Jersey – Newark
in Partial Fulfillment of the Requirements for the Degree of
Doctor of Philosophy in Applied Physics

Federated Physics Department

August 2009

APPROVAL PAGE

CARBON NANOTUBE ELECTRONIC STRUCTURES AS ANTI-CORROSION COATINGS

Sreeya Sreevatsa

Dr. Haim Grebel, Dissertation Advisor — Date
Professor, Department of Electrical and Computer Engineering, NJIT

Dr. John Fedrici, Committee Member — Date
Distinguished Professor, Department of Applied Physics, NJIT

Dr. Onofrio Russo, Committee Member — Date
Associate Professor, Department of Applied Physics, NJIT

Dr. Ken Ahn, Committee Member — Date
Assistant Professor, Department of Applied Physics, NJIT

Dr. Camelia Prodan, Committee Member — Date
Assistant Professor, Department of Applied Physics, NJIT

Dr. Daniel E. Murnick, Committee Member — Date
Professor, Department of Physics, Rutgers University

BIOGRAPHICAL SKETCH

Author: Sreeya Sreevatsa

Degree: Doctor of Philosophy

Date: August 2009

Undergraduate and Graduate Education:

- Doctor of Philosophy in Applied Physics,
  New Jersey Institute of Technology, Newark, NJ, 2009

- Master of Science in Electrical and Computer Engineering,
  New Jersey Institute of Technology, Newark, NJ, 2003

- Bachelor of Science in Electronics and Communication Engineering,
  People's Education Society Institute of Technology, Bangalore, India, 2001

Major: Applied Physics

Presentations and Publications:

Sreevatsa, S., and Grebel, H., "Permeable Electronic Structures as Anti-corrosion Coatings", *Journal of Electrochemical Society*, Submitted, August, 2009.

Sreevatsa, S., and Grebel, H., "Carbon Nanotube Structures as Ionic Barriers: A New Corrosion Prevention Concept", *ECS Transactions*, volume 19, 2009 *Journal of Electrochemical Society*, Accepted, and ECS seminar talk, San Francisco, CA, May, 2009.

Sreevatsa, S., Banerjee, A., and Grebel, H., "Graphene As A Permeable Ionic Barrier", *ECS Transactions*, volume 19, number 5, pp. 259-264, 2009 and poster presentation, San Francisco, CA, May 2009. Awarded the best poster award.

Sreevatsa, S., and Grebel, H., "Permeable Bio-Electronic Carbon Nanotube Structures", *NYBA poster presentation*, NY, NY, April, 2009.

Sreevatsa, S., and Grebel, H., "Permeable Bio-Electronic Carbon Nanotube Structures", *School level Dana Knox Research Showcase poster presentation,* NJIT, NJ, Spring, 2009.

Sreevatsa, S., "Electronic Nano-Structures as Ionic Barriers: A New Corrosion Prevention Concept", *APS seminar talk,* Pittsburgh, PA, March 2009.

Sreevatsa, S., and Grebel, H., "Corrosion Protection with Transistor-like Structures", *ECS Transactions*, volume 13, number 27, pp. 115-122, 2008.

Sreevatsa, S., and Grebel, H., "Control of Surface Chemistry by Electronic Structures", *School level Provost Research day poster presentation,* NJIT, NJ, Spring, 2008. 3rd place, student poster presentation award.

Sreevatsa, S., and Grebel, H., "Permeable Bio-Electronic Structures", *NYBA poster presentation,* NY, NY, April 2008.

Sreevatsa, S., Zhang, Y., and Grebel, H., "Control of Surface Chemistry by Electronic Structures", *MRS Poster Presentation*, Boston, MA, November 2007.

To my family, especially my parents, Sandhya and Sreevatsa

ACKNOWLEDGMENT

I am heartily thankful to my supervisor, Dr. Haim Grebel, whose encouragement, guidance and support enabled me to develop an understanding of the subject. His constant support and encouragement throughout the course of my doctoral studies has been invaluable. Special thanks to Dr. Huixin He for providing the necessary resources to perform some of the experiments. I would also like to express my gratitude to my Ph.D. dissertation committee members, Dr. John Federici, Dr. Onofrio Russo, Dr. Ken Ahn, Dr. Camelia Prodan and Dr. Daniel Murnick for constructive criticism and valuable comments. I am grateful for the financial support that Physics department provided me.

TABLE OF CONTENTS

TABLE OF CONTENTS
(Continued)

TABLE OF CONTENTS
(Continued)

LIST OF TABLES

LIST OF FIGURES

LIST OF FIGURES
(Continued)

LIST OF FIGURES
(Continued)

Figure **Page**

LIST OF FIGURES
(Continued)

LIST OF FIGURES
(Continued)

Figure **Page**

LIST OF FIGURES
(Continued)

Figure **Page**

LIST OF FIGURES
(Continued)

Figure **Page**

LIST OF SYMBOLS

X	Y
E_0	Standard potential
R	Universal Gas constant (8.314 $J.mole^{-1}.K^{-1}$)
T	temperature (in K)
F	Faraday's constant (96,490 $C.mole^{-1}$)
k	Boltzmann constant (1.38×10^{-23} m^2 kg s^{-2} K^{-1})
η for diode	Ideality factor
V_T	Volt-equivalent of temperature (26 mV)
Icorr	Corrosion current (A)
Ecorr	Corrosion potential or Open circuit potential (V)
βa, βc	Anodic and cathodic Tafel slopes
η in electrochemistry	Overpotential (V)
Rp	Polarization resistance (Ohms)
CNT	Carbon Nanotube
SEI	Semiconductor electrolyte interface
SCR	Space charge region
LPR	Linear polarization resistance
EIS	Electrochemical impedance spectroscopy
SEM	Scanning electron microscopy
EDX	Energy dispersive X-ray spectroscopy

CHAPTER 1

INTRODUCTION

Corrosion is defined as 'destructive attack on metal by chemical or electrochemical reaction with its environment' [1]. Rusting is a manifestation of corrosion of iron or, iron-based alloys with the formation of corrosion products consisting mainly of hydrous ferric oxide. According to a two year study released by the Federal Highway Authority in 2002, the direct cost to the US economy due to metallic corrosion was nearly $300 billion [2]! The harmful impact of metallic corrosion is multifold, namely economy, safety hazard and conservation of resources. Economically, losses due to corrosion are most visible in iron pipes, ships, tanks, bridges, etc. Failure of equipments might be proven fatal for human life. Replacing corroded metals is not only expensive, but also hazardous and put a burden on landfills. Finally, the act of constantly replacing metals depletes natural resources. Hence, it is imperative that corrosion be prevented.

Corrosion of metal is fundamentally an electrochemical process where an anodic metal loses its ions thereby, donating electron/s to its immediate environment. The electrons are absorbed at the cathode or, might react with oxygen in the atmosphere. The total rate of anodic reaction should be equal to the total rate of cathodic reaction in order to maintain charge neutrality when no external voltage is applied.

1.1 Electrochemical Theory of Corrosion

When a metal is placed in an electrolyte with ions, a dynamic equilibrium is achieved:

$$M^{n+} + ne^- \Leftrightarrow M$$

At equilibrium, this results in a potential difference between the metal and the electrolyte. Nernest equation dictates:

$$E = E_0 + \frac{RT}{nF} \cdot \ln(M^{n+})$$

Here E_0 is the standard potential (when metals are placed in an increasing order, the standard potential list forms the electrochemical series), R is the universal gas constant (8.314 $J.mole^{-1}.K^{-1}$), T is temperature (in K), F is Faraday's constant (96,490 $C.mole^{-1}$) and $[M^{n+}]$ is the concentration of metallic ionic species in the electrolyte at equilibrium. When two metals of different potentials are connected together (for example by an external wire) current flows to reduce the potential difference between them. It is important to note that the corrosion process involves three parts (Figure 1.1): The anode, which is corroded, the cathode where electrons are absorbed (a reduction process) and the external path through which electrons flow. All three must be present in order for the corrosion to occur. This is true for any redox reaction of the form

$$Ox + ne^- \Leftrightarrow Red$$

Where Ox is the oxidant and Red is the reductant. The potential is given by the corresponding Nernest equation as:

$$E = E_0 - \frac{RT}{nF} \ln\left(\frac{[Red]}{[Ox]}\right)$$

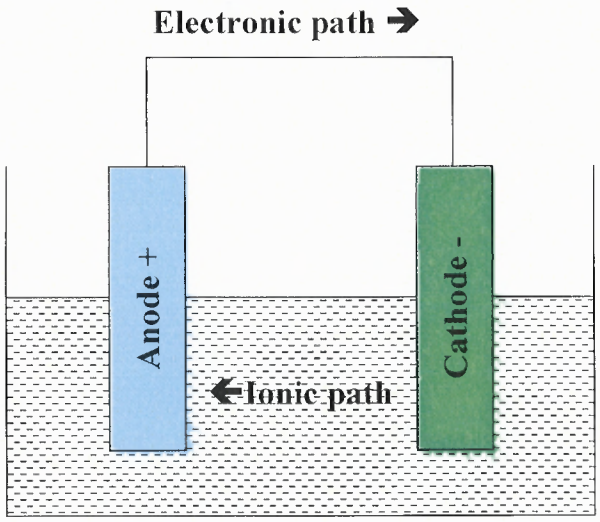

Figure 1.1 Basic electrochemical cell.

Where [Ox] and [Red] are concentrations of oxidant and reductant, respectively. An example of the overall corrosion reaction for iron in an aerobic environment is:

Corrosion or oxidation reaction at Anode:

$$Fe \rightarrow Fe^{2+} + 2e^-$$

$$E = -0.440 - \frac{RT}{2F} \ln\left(\frac{[Fe^{2+}]}{[Fe]}\right)$$

Where standard potential E_0 of Fe is -0.440 V and activity of [Fe]=1

Reduction reaction at the Cathode:

$$O_2\,(g) + 2H_2O + 2e^- \rightarrow 4OH^-$$

$$E = 0.40 - \frac{RT}{2F} \ln\left(\frac{[OH^-]^4}{p_{O_2}}\right)$$

Where standard potential for oxygen reduction is +0.40V and p_{O2} is fugacity of oxygen (in atmospheres)

The overall rust formation is

$$4Fe^{2+}(aq) + O_2(g) + 6H_2O(aq) \rightarrow 2Fe_2O_3.H_2O(s) + 8H^+(aq)$$

A metal will corrode if its oxidized form is preferential to its reduced form. In the above example, the standard potential for the reduction of oxygen is +0.40 V and the standard potential for the oxidation of iron is lower, –0.44 V, hence, corrosion of iron occurs.

There are two types of processes that occur at the metal/electrolyte interface: Faradaic and non-Faradaic process. Faradaic process involves charge (for example, electrons) transfer across the metal/electrolyte interface. This results in reduction and oxidation of different species as described above. Faraday's law states that the amount of chemical reaction due to flow of current is directly proportional to the amount of electricity passed. Since the charge transfer follows Faraday's law, it is called Faradaic process. Under some conditions a given metal/electrolyte does not transfer charges for a range of potential. However, adsorption/desorption can occur and the metal/electrolyte interface can change with the varying external potential. Such a process is called non-Faradaic process. This behavior is analogous to a capacitor. The charge on the metal could be positive or negative depending on the potential across the interface and the composition of the electrolyte, forming one side of the capacitor plate. On the electrolyte side, specific ions are adsorbed onto the metal surface forming the inner Helmholtz plane. This forms the other plate of the capacitor, with a very small separation distance (< 10 Å). The non-specifically adsorbed ions in the electrolyte forming the outer Helmholtz plane, has only long-range electrostatic force and hence the electrical double layer is essentially independent of the outer Helmholtz charge layer (Figure 1.2). Further out into the electrolyte, it is the diffuse layer which is charge neutral.

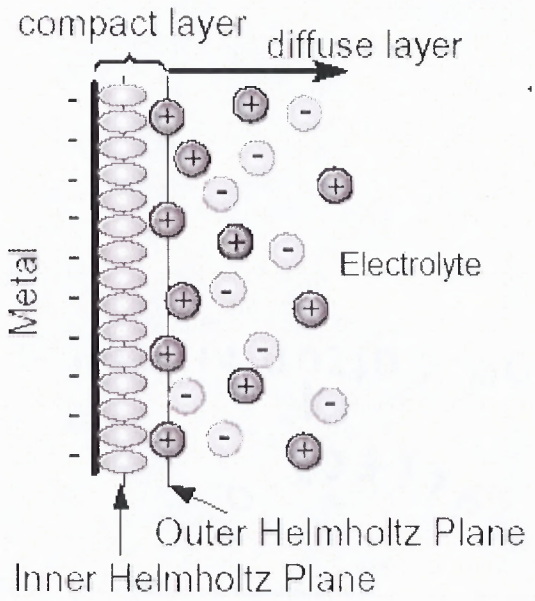

Figure 1.2 Schematic of the electric double layer at metal/electrolyte interface.

Corrosion damage is mainly thought of as rusting and tarnishing. This is not necessarily true as there are corrosion damage due to cracking, loss of ductility and pitting. There are five main types of corrosion:

1. Uniform attack - This includes the commonly occurring rusting. Corrosion rate is a measurement of the corrosion expressed in material lost depth per unit time (also called penetration rate). In SI units, corrosion rate is measured in millimeters per year (mm/yr). For example ordinary steel corrodes at nearly 0.01270 mm/yr. The initial rate of attack is usually higher than the final rate. Hence, the duration of exposure should also be mentioned. Other examples of uniform attack are tarnishing of silver, fogging of nickel and high temperature oxidation of metals.
2. Pitting- This is a localized attack where rate of corrosion is higher at some points compared to the entire metal surface. If the area of attack is relatively small then the pits formed are said to be deep. If the area of attack is wide and not so deep, it

is said to be a shallow pit. Depth of pitting is expressed using a pitting factor, which is the ratio of the deepest penetration to the average pit depth. If the factor is 1 then the pitting is uniform. Pitting typically occurs in iron buried in soil, steel immersed in seawater, copper and brass condenser tubes.

3. Dezincification and Parting - Dezincification occurs with zinc alloys where the zinc corrodes preferentially. This reduces the metal's tensile strength and ductility (a metal's ability to be drawn, stretched or formed without breaking). Parting is similar to dezincification where one or more components corrode preferentially and leave a porous residue of the metal behind. This occurs in more noble metal alloys like gold-copper and gold-silver.
4. Intergranular corrosion - This is localized corrosion at grain boundaries of a metal resulting in loss of strength and ductility. Examples are improperly heat treated 18-8 stainless steel or duralumin type alloys. The attack is rapid and catastrophic.
5. Cracking - When a metal subjected to constant tensile stress cracks in a corrosive environment, the failure is called stress corrosion cracking. Almost all structural materials are subject to stress corrosion cracking. For example, carbon and low alloy steels, brass, stainless steel, titanium alloys, nickel alloys and many others. This type of corrosion can be reduced by restricting fewer corrosive chemical species in the environment. In some cases, the necessary stresses are sufficiently high that it limits the failure from happening.

There are several ways of preventing corrosion. The electrochemical corrosion prevention falls into two broad categories are:

1. Cathodic protection
2. Anodic protection

Cathodic protection is achieved by impressed current, where the metal to be cathodically protected is made to be the cathode by applying current. This will make the metal less active and hence protect it. Cathodic protection can also be achieved by coupling the metal that need to be protected with a relatively active metal. The application of cathodic protection can be seen in oil pipelines and ship hulls [4, 5]. On the other hand, anodic protection is achieved by a formation of passivation layer due to impressed current. Anodic protection is more limited compared to cathodic protection in the sense that not all metals can be protected by this method. It was first implemented in 1954 for a petrochemical plant [6] and has applications in acid storage vessels, etc. In the following section a detailed history of iron/ steel corrosion prevention are provided.

1.2 History of Corrosion Prevention for Iron and Steel

There are three main types of coatings for corrosion prevention: Metallic coatings, inorganic coatings and organic coatings. Metallic coating can be further classified as noble and sacrificial. Galvanization is the most popular sacrificial metal coatings. Galvanization of iron and steel has existed since the 18^{th} century. In 1741 French chemist Melouin attempted to coat iron with zinc by a dipping process. In 1800, Johann Ritter used Volta's battery to electroplate zinc onto iron. In 1824, Sir Humphrey Davy showed the rudiments of cathodic protection where ship's hulls made of copper were protected by coupling with zinc or iron. In 1836, Sorrel in France received a patent for coating iron by dipping it in molten zinc and coined the term galvanizing. Sendzimir process was the first

commercially viable coating process of zinc on iron. It was installed and was proven sound by Armco Steel Corporation in Butler, PA in 1936. Advantages of zinc coatings are many. The material is inexpensive compared to nickel and chrome. It is non-toxic compared to lead and cadmium. Zinc coatings are relatively thick, pin hole free and last longer. Disadvantages include low resistance to wear and tear and susceptibility to attacks by acid and water [8].

Organic coatings are another means of corrosion prevention. In 1913, Norman A. Dubois conducted a study on corrosion of iron and steel with intent to discuss the essential properties for paint. He pointed out that there were several possible reasons for iron and steel to corrode and any paint requires that it would be relatively impervious to corroding gases like carbon-di-oxide, oxygen and moisture [7]. In 1952, Sadrabin and Marks proposed cathodic protection for steel immersed in water as a combination of metal protective coating and maintaining a current to prevent corrosion at the vinyl coating flaws [9]. In 2000, Alan MacDiarmid shared the Nobel Prize in chemistry for his work on organic conducting polymers. He demonstrated anodic protection of steel with polyaniline [10]. Shinji Fujimoto used the semiconducting property of conducting polymers to prevent corrosion of iron based alloys [11]. Inorganic coatings include vitreous enamel coating and Portland cement coatings. These coatings have been in use since the beginning of the 19^{th} century. Their main disadvantage is that they are susceptible to damage by mechanical and thermal shock.

In this study a new approach to the old problem of corrosion is employed. Carbon nanotube (CNT) electronic junctions are used to prevent corrosion of steel substrates. Unlike paint, carbon nanotube coatings are permeable. These coatings have a directional

potential barrier. The structure may be biased to change the surface potential of the metal. Before proceeding further, the properties of carbon nanotubes and its electrochemical applications are briefly considered.

1.3 Carbon Nanotubes and its Applications

Carbon nanotubes (CNT) are macromolecular forms of carbon with unique properties and with great potential for practical applications. They can be visualized as cylinders formed from seamlessly rolling of graphene sheets. Graphene is a monolayer of graphite having hexagonal lattice symmetry with carbon atoms at the corner of each hexagon. CNTs can be characterized as single wall carbon nanotubes (SWCNT) or multi wall carbon nanotubes (MWCNT) [12, 13]. SWCNT has a single layer of graphene forming one cylinder. MWCNT are made of many layers of graphene forming concentric cylinders (Figure 1.3). Depending on the rolling vector (n,m), SWCNTs can be further classified as armchair (n,0), zig-zag (n-m= modulus of 3) or, chiral type (Figure 1.4) [14]. The armchair and zig-zag tubes are semiconducting and the chiral type is metallic. Hence, a third of tubes of as-produced CNTs are metallic. There are three main methods of producing CNTs:

1. Electric arc discharge - In this method, current is passed between an anode and a cathode producing a bright arc of electricity that vaporizes carbon atoms. The carbon plasma at the anode re-condenses at the cathode, thus forming carbon nanotubes.
2. Chemical vapor deposition - Metal catalyst particles are placed on a surface and heated to high temperatures in the presence of hydrocarbon gases. The catalysts

acts as seed anchor for dissociated carbon atoms and promotes the formation of nanotubes.

3. Laser Ablation - High power laser is used to vaporize carbon atoms from graphite surface. The resulting soot has carbon nanotubes in it.

Carbon nanotubes have many remarkable properties such as high electrical conductivity, high chemical stability and extremely high mechanical strength and modulus.

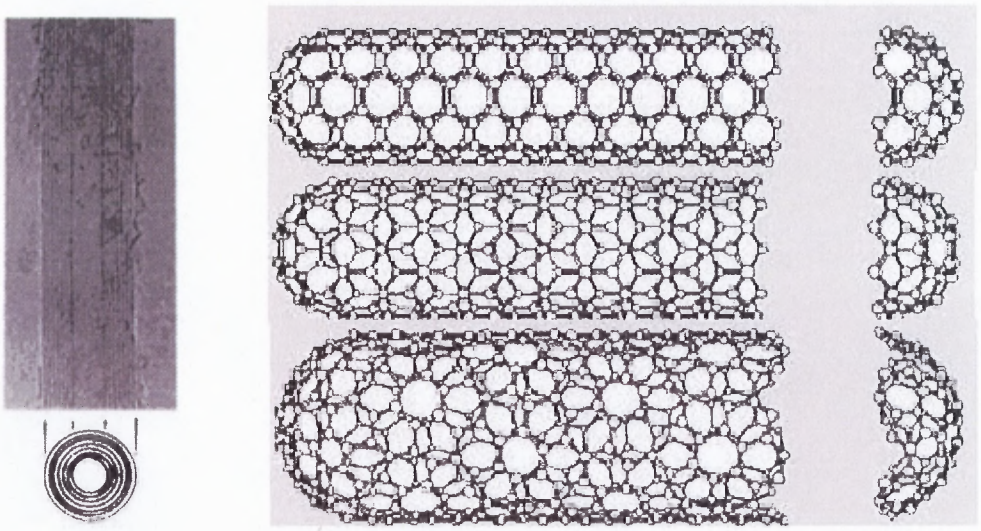

Figure 1.3 Multiwall and Single wall carbon nanotubes.

Carbon nanotubes are in the forefront of electrochemical research. In comparison to other semiconducting material, carbon is less likely to oxidize and therefore, are suitable for corrosion protection. MWCNT composites are shown to have anti-corrosive properties [19]. Other electrochemical properties of SWCNTs as electrode materials have been investigated [15-18]. Study of several redox couples have shown the beneficial use of the high aspect ratio and high conductivity of SWCNTs in the enhancement of measured signals.

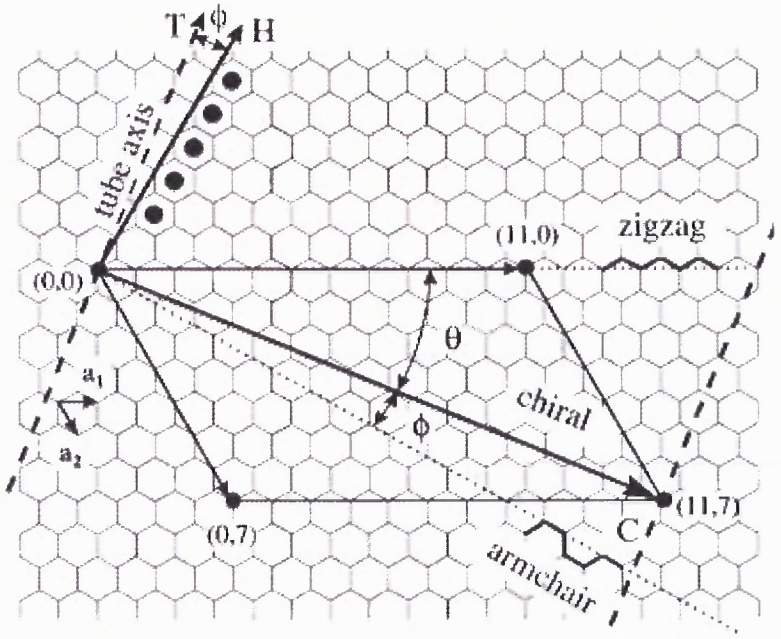

Figure 1.4 Relation between hexagonal lattice and chirality of CNTs.

1.4 Semiconductor-Electrolyte Interface

Electronic properties of solid materials are described in terms of band model. When isolated atoms which have filled and vacant orbitals are brought together, they form new molecular orbitals. These orbitals form continuous bands: The filled bonding orbitals form the valence band and the vacant orbitals form the conduction band. These bands are separated by a band gap Eg. If Eg << kT, where k is Boltzmann constant ($1.38*10^{-3}$ J/K) and T is the temperature (in K), then the conduction and valence band overlap. These materials are good conductors of electricity (examples are iron, gold, and copper). When Eg is large (between 1 to 4eV), then the conduction band is almost vacant and the valence band is almost full (Figure 1.5 (a)). The only carriers arise due to thermal excitation of electrons from valence band (which is left with holes) to conduction band (Figure 1.5 (b)). Such materials are called intrinsic semiconductors. Electrons in conduction band and

holes in valence band can also be introduced by doping the semiconductor, producing extrinsic semiconductor material. A dopant is said to be a donor if an excess electrons results and the material doped with a donor species is called an n-type semiconductor, (Figure 1.5 (d)) which has electrons as majority carriers and holes as minority carriers. Similarly, an acceptor dopant generates excess of holes in the semiconductor material and the material is called p-type semiconducting material (Figure 1.5 (c)). An important concept in semiconductor material is the Fermi energy level (E_F) which is defined as the energy where probability of a level being occupied is ½ (probability of being occupied is equal to probability of being vacant). For an intrinsic semiconductor E_F is midway in the energy gap. For n-type material, E_F is closer to conduction band (E_c) and for p-type material, E_F is closer to valence band (E_v).

The space charge region formed as a result of a semiconductor-electrolyte interface (SEI) is of particular interest for the electrochemical processes considered in this study. An example of n-type semiconductor in contact with an electrolyte is discussed here. If the redox potential (E_{redox}) of the electrolyte is strongly oxidizing, then the semiconductor material will have a strong tendency to donate electrons. The alignment of Fermi energy level (E_F) in the semiconductor with the redox potential leads to an upward band bending of the conduction band (E_c) and valence band (E_v) energy levels in the semiconductor, creating a space charge region within the semiconductor as shown in Figure 1.6. The region of the semiconductor around SEI has less electrons compared to the bulk of the semiconductor. This region is called the space charge region (SCR).

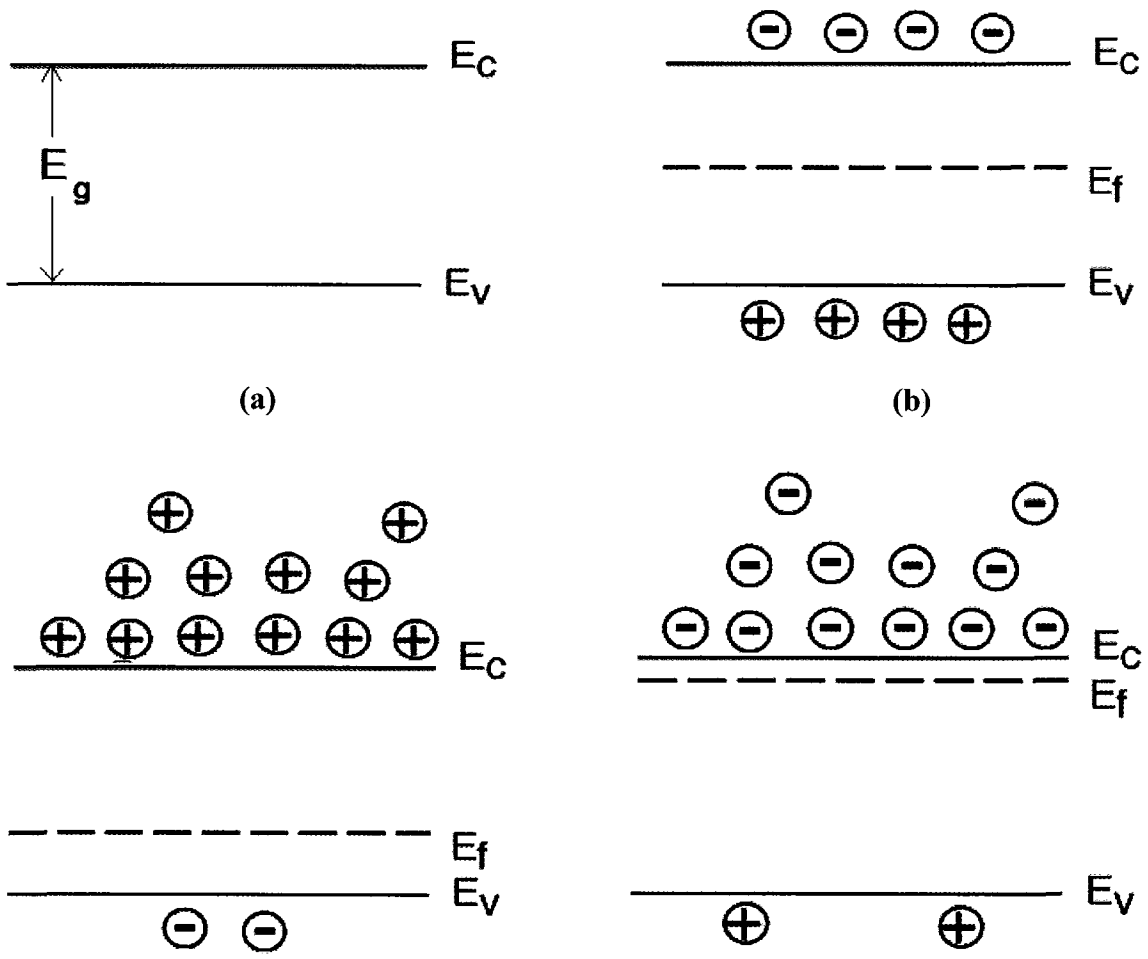

Figure 1.5 Two-dimensional energy band diagram representation for (a) an intrinsic semiconductor at absolute zero, (b) intrinsic semiconductor at temperatures where there are thermally excited carriers, (c) p-type extrinsic semiconductor and (d) n-type extrinsic semiconductor material.

The SCR may occur through three different mechanisms

- Depletion layer (no degenerate doping) - immobile and uncompensated donor ions (as shown in Figure 1.6)
- Accumulation layer – as a result of mobile electrons (Figure 1.7(a))
- Inversion layer – as a result of mobile holes (Figure 1.7(b))

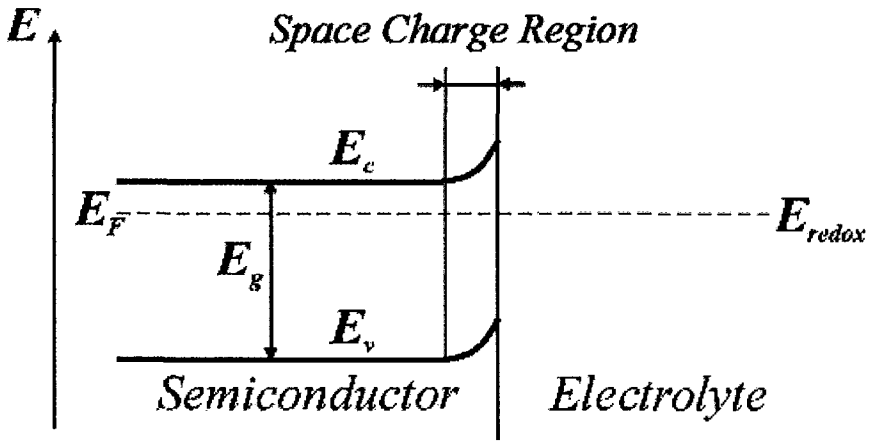

Figure 1.6 Schematic of the energy band diagram for n-type semiconductor-electrolyte interface.

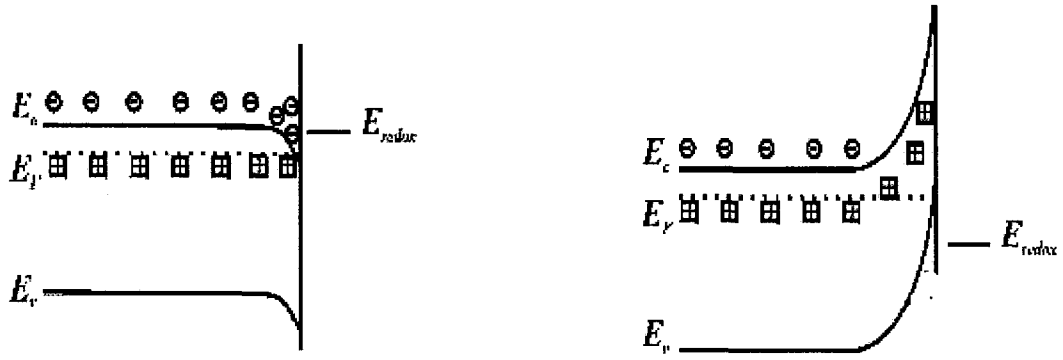

Figure 1.7 Types of charged layers in n-type semiconductor interacting with an electrolyte (a) Accumulation layer and (b) Inversion layer.

From electrochemical point of view, the type of SCR determines whether an external applied voltage drops the voltage across the SCR, the electrolyte or, distributes it amongst both. Typically, for SCR overlapping with the depletion region, the SEI behaves as a Schottky contact. There, the width of the SCR decreases with the increase in the donor (dopant) concentration as given in the equation below.

$$W = \sqrt{\frac{2 \cdot \varphi \cdot \varepsilon}{q \cdot N_D}}$$

Where W is the width of SCR, φ is the applied voltage, ε is dielectric permittivity of the semiconductor material, q is charge and N_D is donor concentration. So, in the depletion region all the voltage drops across the SCR. Also, the capacitance of the SCR is very high due to a typically large W of about 1000 Å compared to the width of the double layer capacitance of less than 10 Å (explained in section 1.1). In the accumulation and the inversion layer modes, the semiconductor behaves as a metal and all the applied voltage drops across the electrolyte. A few aspects are identified here:

1. The energies of conduction band and valence band are fixed. Band bending occurs to match the Fermi energy level in the semiconductor with the redox potential of the electrolyte. This results in electron transfer to or, from the electrolyte depending on the direction of band bending and independently of the external applied voltage.
2. The energy levels in a semiconductor may be controlled by doping.

These unique properties of semiconductor materials enable the study of charge transfer between the electrode and electrolyte as discussed in the discussion sections of chapters 4 and 5.

1.5 Diode and Transistor Structures

Electronic structures can be formed by the semiconducting p-type and n-type materials. A diode (or a p-n junction) is a two terminal device which allows current to flow in one direction (forward biased condition) and prevents it in the opposite direction (reverse biased condition). For a p-n junction, the current I is related to the applied voltage V_a by the equation

$$I = I_0(e^{\frac{V_a}{\eta V_T}} - 1)$$

Here, I_0 is the reverse saturation current; η is the ideality factor; V_T is volt-equivalent of temperature and has a value of 26 mV at room temperature (300 ^{o}K). The diode is forward biased when V_a is positive, indicating that the p-side of the junction is connected to positive of voltage supply with respect to the n-side. Under forward bias, four regions of operation may be identified (Figure 1.8) [20]. First, there is the ideal diode region where current increases by one order of magnitude for every 60 mV of applied voltage. This region has an ideality factor of one. Since the applied voltage is several times of V_T, the current has an exponential dependence on voltage given by

$$I = I_0 e^{\frac{V_a}{\eta V_T}}$$

The ideality factor may be obtained by the slope of the semi-logarithmic curve by

$$\eta = \frac{\frac{1}{slope}}{59.6\ mV/decade}$$

where 1/slope is in units of V/decade.

To the left of the ideal diode region is the depletion recombination region, where the external voltage reduces the barrier potential and the current is the result of trap assisted recombination of charges. The ideality factor for this region is expected to be two. To the right of the ideal diode region, the current becomes limited due to high injection effects and series resistance. High injection occurs when the injected minority carriers exceed the doping concentration. At further high currents the diode behaves as a resistor and the current increases linearly rather than exponentially with the applied voltage.

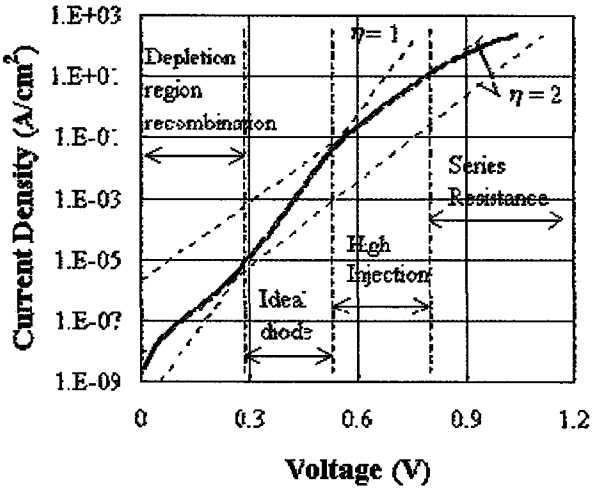

Figure 1.8 I-V characteristics of a silicon diode (p+-n) under forward bias with $N_d = 4 \times 10^{14}$ cm^{-3}, $\tau_p = 10$ μs, and $\mu_p = 450$ cm^2/V-s.

A Bipolar Junction Transistor (BJT) consists of two back to back p-n junctions with a common middle region called base. It is a three terminal device with contacts to the two outer regions called collector and emitter and the third contact is to the base. It is called bipolar since its operation involves movement of both the electrons and the holes. Transistor is a semiconductor device used to switch or, amplify electronic signals. The current from the emitter (I_E) is the sum of currents through the base (I_B) and collector (I_C). Transport factor α is defined as the ratio of collector and the emitter current and the gain β is defined as the ratio of collector and the base currents. In this study transistors are used in common emitter mode, the biasing for which is as indicated in figure 1.9.

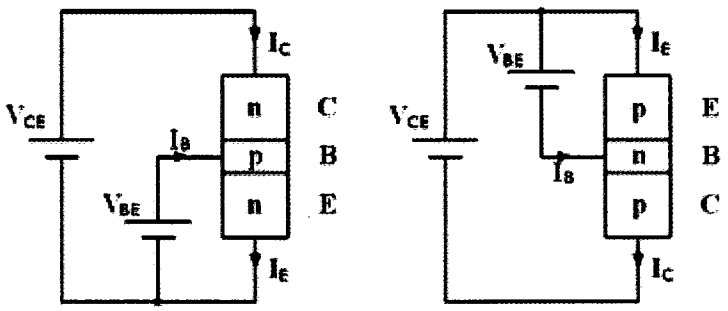

Figure 1.9 Common-emitter mode configuration of *n-p-n* and *p-n-p* transistors.

In this work, a new concept of anti-corrosion path where electrochemical principles with the carbon nanotube based electronic devices are combined. Carbon nanotube synthesis is quite established and their functionalization is well known [21-26]. The percentage of semiconducting tubes increases substantially by functionalizing the tubes [27-31]. Improved semiconducting properties were obtained by imbedding the functionalized tubes in the like of polyurethane and poly(methyl methacrylate), thus achieving robust protecting films. Such electronic barriers were introduced between the electrolyte and steel substrates. Hypothesis here is that the electronic barriers impede diffusion of corrosive ions towards the metal surface. As a consequence, the sequence of the junction, namely, metal-*p-n* or, metal-*n-p*, matters (for details see chapter 4). In the case of transistor like structures metal-*p-n-p* or metal-*n-p-n*, the base provided a control by means of which the surface potential could be controlled as discussed in chapter 5.

Let us consider the following coatings and their corrosion rates. For weathering steel, which is used in bridges, the formed rust layer provides for passivation. The corrosion rate for such steel does not exceed 7.5 μm/yr, otherwise it should not be used. In the case of paint coatings, the life-span is given in years. Two coats of red iron oxide paint have durability of 3 years. By using different surface finish techniques such as sand

blasting, or, pickling (treating the surface to be painted with aggressive acids, such as a mixture of nitric and hydrofluoric acid and dissolve heavy scale, weld oxides and other surface contaminates; passivation, on the other hand, is made with milder solutions, such as citric or nitric acid and is intended to clean the surface and leave the oxide behind). Durability in such cases may be increased to 6 years. The base metal corrosion rate where liquid coatings are used should not exceed 1300 μm/yr [56]. The disadvantage here is that a breach in the paint results in a rapid lift-off (pealing) of the entire coating. When chromate inhibitors are used, the corrosion rate for mild steel is nearly 2.54 μm/yr (without the inhibitor the corrosion rate would be, approximately, 533 μm/yr). For synthetic sea water, the corrosion rate with chromate inhibitor is 43 μm/yr and 610 μm/yr without it [1]. A combination of conducting polymer coatings (polyaniline/polypyrrole) showed that carbon steel corroded at a rate of 707 μm/yr and 304L corroded at the rate of 200 μm/yr in NaCl solution [60]. The corrosion rate was attributed to the oxidation of the polymer coatings. The metal was protected as long as the coating was not consumed. The benchmark for this study is to achieve lower corrosion rates than the ones mentioned here. Unlike conductive polymers, there are no active oxidants to be consumed and therefore, the life expectancy of junctioned coating would be measured in years.

CHAPTER 2

ELECTROCHEMICAL TEST METHODS

Corrosion monitoring has many purposes that include:

1. Understanding the mechanism and controlling of corrosion
2. Evaluation of corrosion alternatives and different materials
3. monitoring corrosion rate to predict component lifetime and optimize component replacement, maintenance and repair schedules

The advantages of electrochemical test methods are:

1. results are obtained in minutes or hours
2. corrosion behavior can be measured over a wide range of conditions in a single environment
3. many of the tests can be applied in the laboratory or in process plants

Electrochemical monitoring techniques are based on the premise that corrosion is an electrochemical process. It relies on accurate measurement of current and voltages to characterize a process. The electrochemical test methods that are relevant to this thesis are Linear polarization resistance (LPR) and Electrochemical impedance spectroscopy (EIS) which are discussed in detail in the following subsections. The standard procedure for cleaning and preparing a test sample is given in ASTM G1. The standard terminology relating to corrosion and corrosion testing is given in ASTM G15.

Potential, current and resistance are the primary determining factors of a corrosion process in any environment. The potential difference between anode and cathode drives the metal dissolution or corrosion. Potential is measured with respect to a reference

electrode. A reference electrode is a metal immersed in an electrolyte that has an electrochemical potential that does not vary with time. There are several available standard reference electrodes, such as Standard Hydrogen Electrode (SHE), Standard Calomel Electrode (SCE) and Silver/ Silver Chloride Electrode (Ag/AgCl). Current is a measure of number of electrons that flow per second from the anodic sites to the cathodic sites. Current provides the rate at which the reactions are proceeding.

Potentiostat is the device used to control the potential of the test sample called the working electrode with respect to a reference electrode. The basic component of a potentiostat is a voltage feedback operational amplifier. The op-amp drives enough current so that the voltage difference between the inverting and non-inverting terminals is zero. A schematic of the setup is shown in Figure 2.1 [32].

2.1 Linear Polarization Resistance Theory

The standards for this test method are given in ASTM G5, G59 and G102. According to the standards the potential of the working specimen is scanned or stepped 1 hour after the specimen immersion in the electrolyte. The polarization plot is plotted on semilogarithmic graph. Polarization resistance is related to the corrosion rate of the metal measured at or near the corrosion potential. Corrosion potential is the potential of a corroding surface in an electrolyte under open circuit conditions. A small potential scan ΔE defined with respect to corrosion potential is applied to the metal sample. The resultant currents are recorded. Then the polarization resistance Rp is defined as:

$$Rp = \frac{\Delta E}{\Delta I}$$

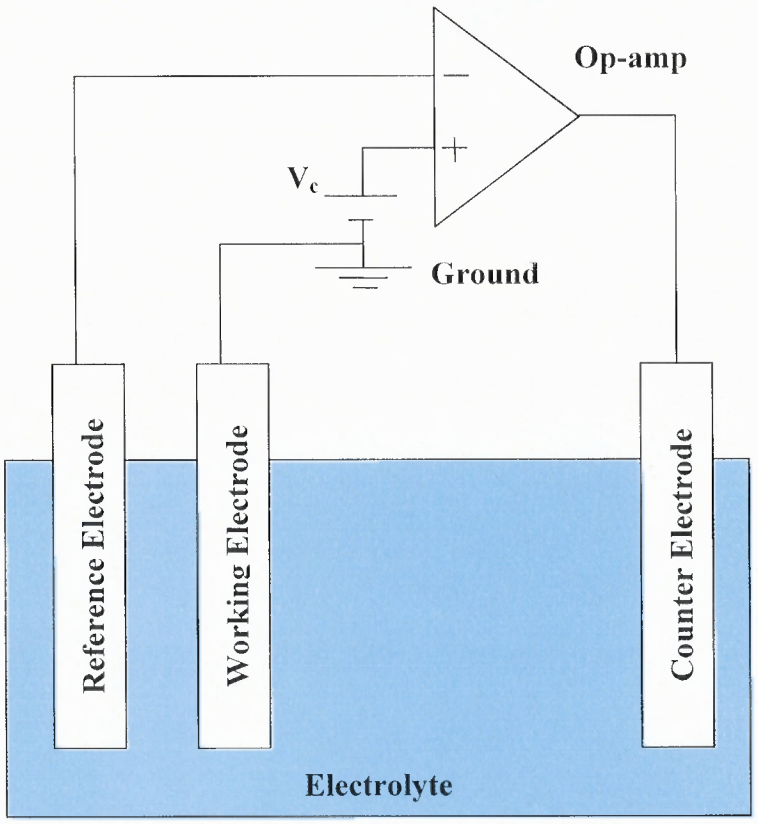

Figure 2.1 Schematic of a potentiostat.

The corrosion current density Icorr is related to polarization resistance by the Stern-Geary coefficient B by the relation:

$$Icorr = 10^6 \frac{B}{Rp}$$

Rp is in Ω-cm^2, Icorr is in μA/cm^2 and B is in V

The Stern-Geary coefficient is related to the anodic βa and cathodic βc slopes by the relation:

$$B = \frac{\beta a \cdot \beta c}{2.303(\beta a + \beta c)}$$

Where the slopes are in units of V/decade when current-voltage characteristics are plotted on a semi-logarithmic scale.

The corrosion rate of the corroding specimen is determined in μm/yr by the relation:

$$CR = 3.1510^{7} \cdot \left(\frac{Icorr \cdot M}{F \cdot Z \cdot D} \right)$$

Icorr is the corrosion current in A/m^2; M is the molecular weight of iron; F= 96490 C/equivalent is the Faraday's constant; Z is the valence state of metal in oxidized form and D is the density of iron metal in g/cm^3.

LPR method may be understood by mixed potential theory. Mixed potential theory provides a basis of understanding electrochemical rates. The theory has two premises. One is the conservation of electrical charges where anodic current should be equal to cathodic current in the electrochemical cell. The second is that the anodic reaction and cathodic reaction can be treated separately. The driving force in any electrochemical cell is the potential difference between cathode and anode. The total resistance (R) throughout the cell is the resistance of anode, the ionic path, the cathode and the electronic path. The potential (E) and current (i) in the cell is related by the simple Ohm's law:

$$E = i \cdot R$$

Different types of polarization define the different resistance elements throughout the corrosion cell. Two types of polarization behavior are discussed here: Activation polarization and concentration polarization.

Let us consider an example of iron reaction in hydrochloric acid.

Oxidation (anodic) reaction: $Fe \rightarrow Fe^{2+} + 2e^{-}$

Reduction (cathodic) reaction: $2H^{+} + 2e^{-} \rightarrow H_2$

The system can lower its free energy (ΔG) by oxidation of metal to form metal ion. The driving force for this corrosion reaction is the reduction in free energy change. Free energy is equivalent to an electrochemical overpotential given by Nernest equation. The rate of the reaction can be expressed as current, or, the number of electrons generated per unit time.

$$Current = A \cdot e^{\left(-\frac{\Delta G}{RT}\right)}$$

$$Current = A \cdot e^{\left(\frac{\eta n F}{RT}\right)}$$

Where A is a constant, R is the Universal gas constant, T is the temperature, η (or ΔE) is the overpotential, n is the number of electrons generated per ion and F is the Faraday's constant. An electrochemical cell which behaves as described here is said to be controlled by activation polarization. Activation polarization simply means that the driving force of the reaction (overpotential) is proportional to logarithm of the reaction rate (current). The relation for anodic and cathodic processes under activation polarization are defined as

$$\eta_a = \alpha_a + \beta_a \log i_a$$

$$\eta_c = \alpha_c + \beta_c \log i_c$$

Where η is the overpotential, α and β are Tafel constants, a and c indicate anodic and cathodic variables. The slopes are determined by properties of both the metal surface and the electrolyte. Mixed potential theory deals with anodic and cathodic reactions separately and then the reactions are coupled by the fact that sum total of all anodic currents should be equal to sum total of all cathodic currents. The activation polarization curve for the example of iron dissolution in hydrochloric acid is shown in Figure 2.2 [56]. It can be observed that oxidation increases as the anodic overpotential becomes more positive. Similarly, reduction reaction increases as the cathodic overpotential becomes

more negative. The mixed potential theory is satisfied at the point of intersection of the anodic and cathodic curves. The potential of this intersection is called the corrosion potential Ecorr and the current icorr (Figure 2.3). Ecorr is also known as free corroding potential and open-circuit potential. At potentials more positive than Ecorr, more electrons are generated resulting in a larger anodic current than the cathodic current. At potentials more negative than Ecorr, more electrons are consumed resulting in a greater cathodic current. At Ecorr, no net electron consumption or generation happens. To maintain a system away from Ecorr, current must be supplied from an external source.

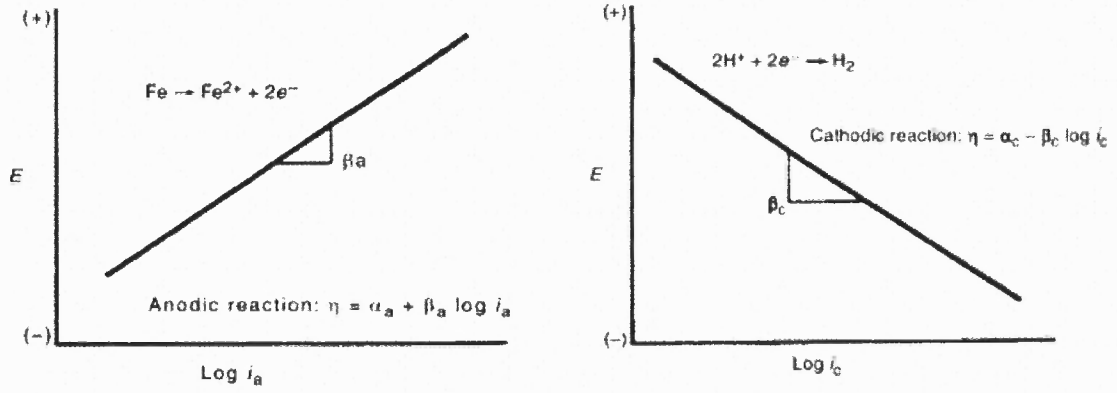

(a) **(b)**

Figure 2.2 Activation polarization curves for (a) anodic and (b) cathodic reactions.

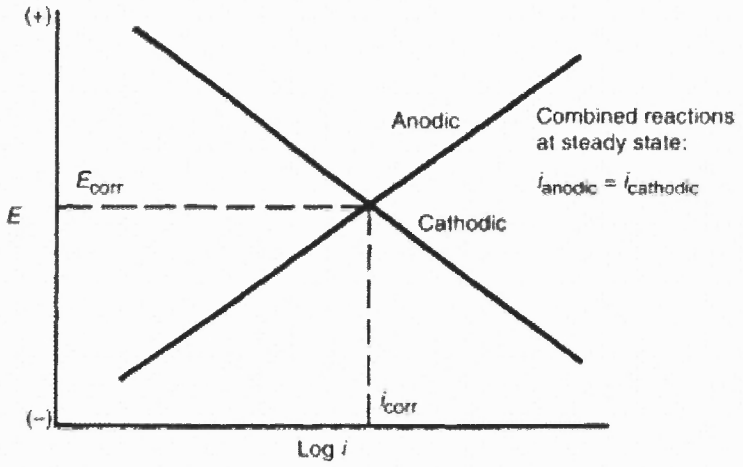

Figure 2.3 Activation polarization curve for combined anodic and cathodic reactions, indicating the corrosion potential Ecorr and corrosion current icorr.

Concentration polarization is due to mass transfer, or, diffusion limited process at the metal surface. For cathodic Tafel slope, as the overpotential becomes more negative, the reduction reaction increases. A point is reached when this increase in the driving force (overpotential) no longer increases the reduction reaction. This region is the concentration polarization region (Figure 2.4).

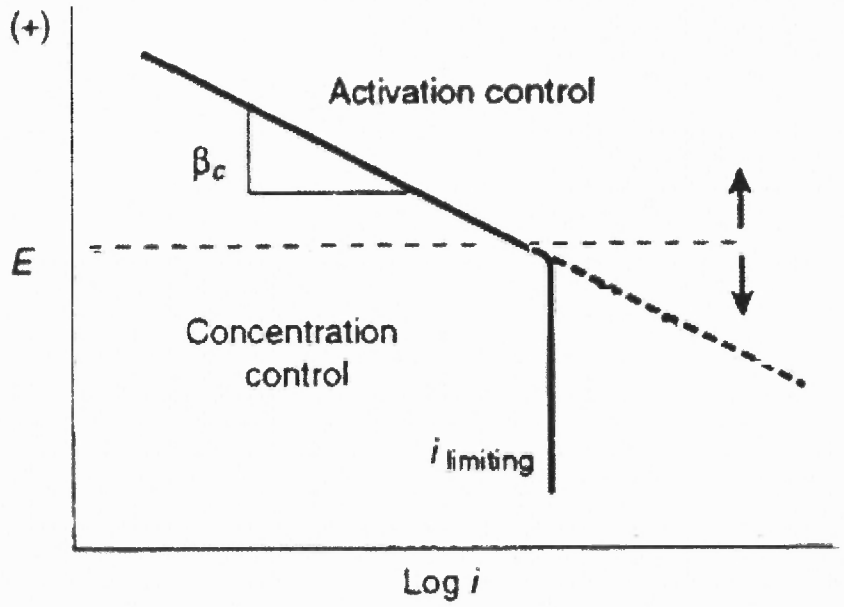

Figure 2.4 Concentration polarization curve for cathodic reaction.

For an active-passive metal such as the one considered in this study (steel), the polarization curve is indicated in the Figure 2.5. The effect of increasing the cathodic reaction rate effectively reduces the corrosion current and hence the corrosion rate as indicated in Figure 2.6. If the initial conditions result in Ecorr(1) and icorr(1), then increasing the cathodic reaction rate as shown by a shift in the cathodic curve, results in Ecorr(2) and icorr(2) resulting in a lower corrosion current. Hence, for an active-passive metal, increasing the cathodic reaction rate can significantly reduce the corrosion rate.

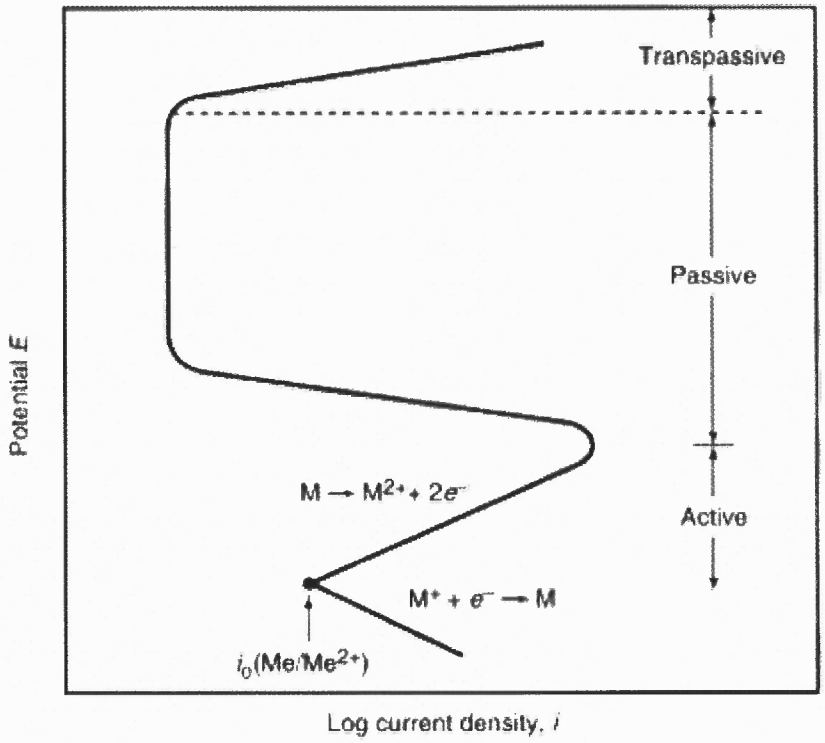

Figure 2.5 Typical polarization curve for an active-passive metal, such as steel.

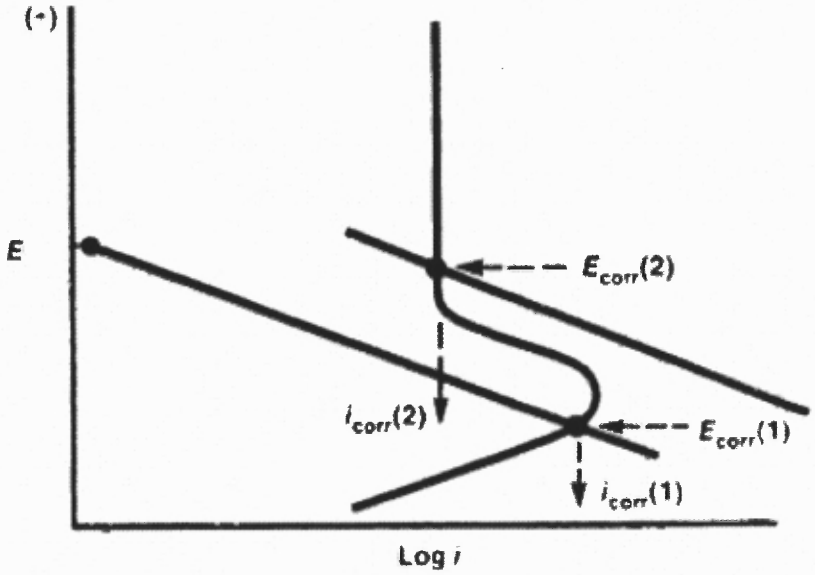

Figure 2.6 Effect of increasing cathodic reaction rate decreases the corrosion current from icorr(1) to icorr(2).

Corrosion rates are usually assessed helping us choosing protective films (passivity). To be effective, the passive film must keep the corrosion current on the surface of the metal minimal. An effective film is one that resists breaching (or breakdown) of the passive film. Breakdown causes localized corrosion and leads to corrosion failure, pitting, intergranular and crevice corrosion. Passive films should not only resist breakdown, they must also be capable of re-passivating at a rate sufficiently high so that exposure to corrosive environment is reduced.

2.2 Electrochemical Impedance Spectroscopy Theory

Electrochemical Impedance Spectroscopy (EIS) can be used to analyze the equivalent impedance of an electrochemical cell. It employs a small AC signal to perturb a specimen over a wide frequency range and monitors the response of the cell to it. The advantages of EIS over LPR are:

1. it allows separation and evaluation of different components of the system, for example, separation of solution resistance from polarization resistance
2. EIS can be used to study coated surfaces more effectively
3. It can be used to determine the properties of surface layers

The analysis of EIS data is rather complex and may not provide a clear picture for many applications. A flow diagram of the EIS steps is shown in Figure 2.7. Experimentally obtained EIS data for a given electrode system may be analyzed by using an exact mathematical model based on plausible physical theory. This gives the theoretical impedance Ztheo(ω). The experimentally obtained impedance could also be analyzed with an empirical equivalent circuit denoted by Zec(ω). In either case, the

experimental impedance data Ze(ω) can be compared to the predicted impedance data Ztheo(ω) or Zec(ω) by fitting the data using reduction of errors between experimental and fitted data.

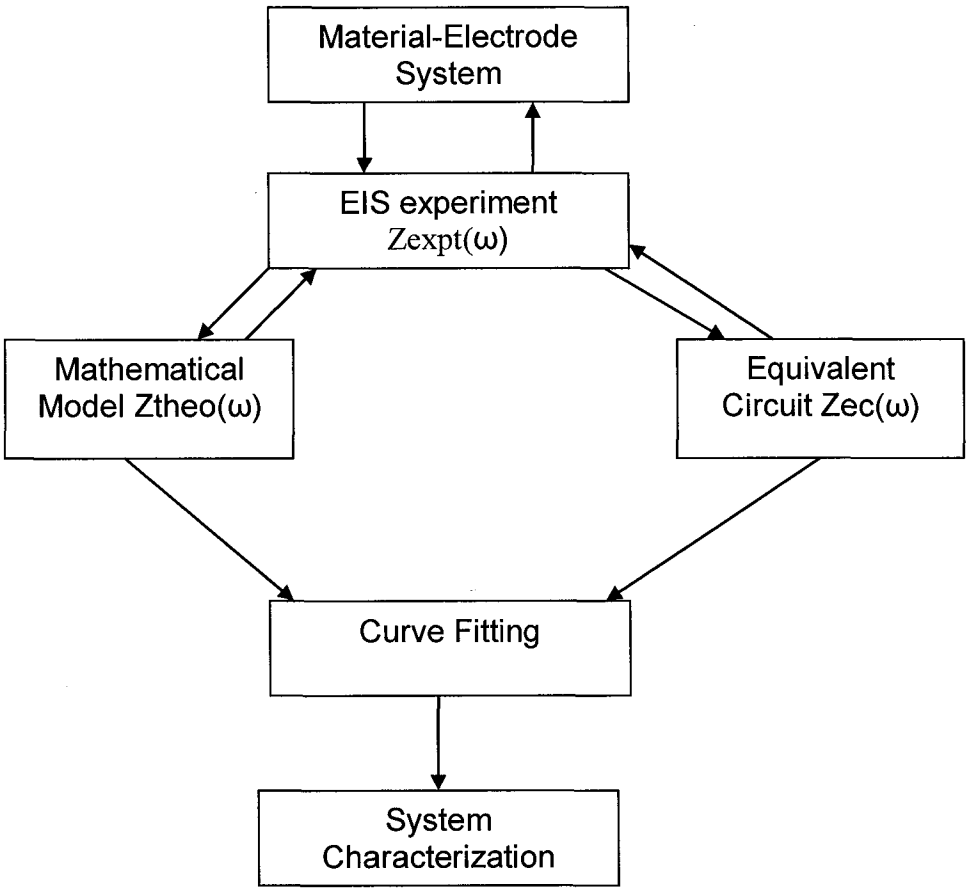

Figure 2.7 Flow diagram for measurement and characterization of a material-electrode system.

When a specimen is placed in an electrolyte and under steady state conditions, the surface potential of the specimen approaches the corrosion potential. If an external perturbation voltage is applied to the system, a net current can be observed. If the perturbation signal is small, then the observed response is approximately proportional to the applied potential. There are three types of perturbation signals that may be applied: A

step voltage, white noise and sinusoidal bias. The most common approach is to apply a single frequency bias and measure the real and imaginary parts of the resulting current by using either an analog circuit, or, a fast Fourier transform analysis of the response. Commercial equipments are available, which automatically assess the impedance of a system as a function of frequency in the frequency range of 1 mHz to 1 MHz. Therefore, if the voltage perturbation signal is

$$v(t) = V_0 \cos(\omega t)$$

And the corresponding current response is

$$i(t) = I_0 \cos(\omega t - \varphi)$$

with v(t), the impressed potential with respect to Ecorr; V_0, the magnitude of impressed potential in V; ω, the frequency of the sinusoid in radian per second; t is the time; i(t), the current response; I_0, the magnitude of the current response; φ, the phase difference between the current and the voltage, then the equivalent impedance Z is defined as:

$$Z = \frac{v(t)}{i(t)} = \frac{V_0}{I_0} \cdot \exp(j\phi)$$

In general, the impedance is denoted as:

$$Z(\omega) = Z_0(\omega)\exp[j\phi(\omega)]$$

There are two methods for graphical representation of the related impedance: Nyquist plots and Bode plots. Nyquist plot is a plot of the real part versus the imaginary parts of the effective impedance. Bode plot is the plot of the magnitude versus the frequency and separately, the phase versus the frequency of the related impedance components. For example, let us consider a Randle's cell whose impedance is given by,

$$Z(\omega) = Rs + \frac{Rp}{1 + j\omega C Rp}$$

The Nyquist diagram is shown in Figure 2.4 and the Bode plots are shown in Figure 2.5. The topology of the impedance and the value of resistors may be obtained by either of the graphs. But, the value of the capacitor can be obtained only by the Bode plot since the Nyquist plot has lost all frequency information [34-37].

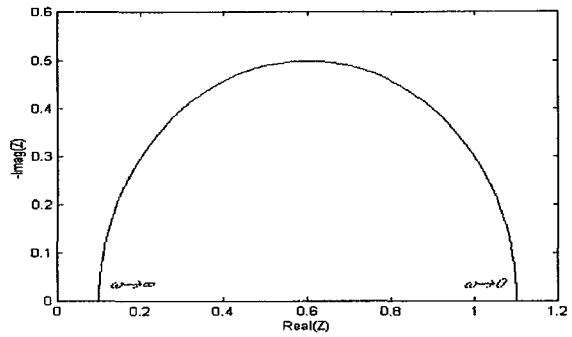

Figure 2.8 Example of a Nyquist plot.

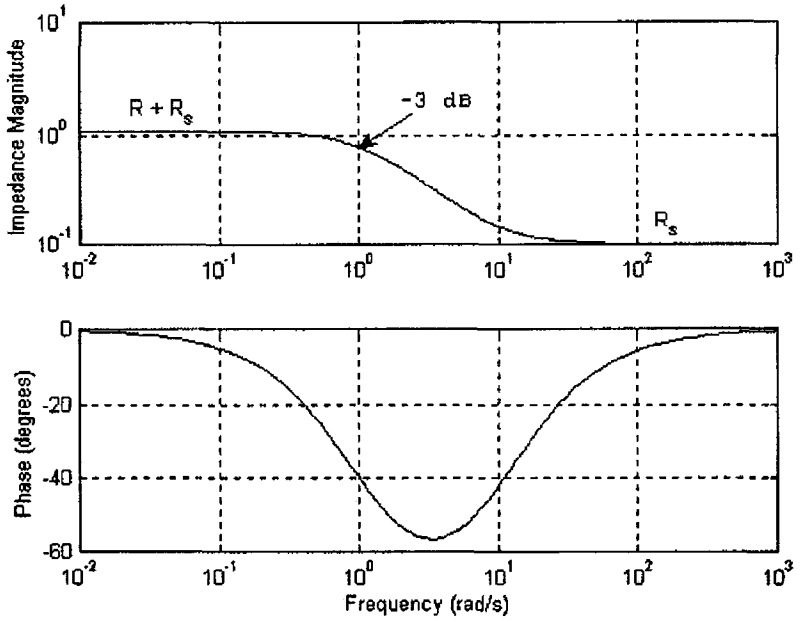

Figure 2.9 Examples of Bode plots.

The elements of the EIS measurements are related to physical properties of the cell. Some of the common components are:

1. Solution resistance - The resistance of an ionic electrolyte depends on the ion concentration, type of ions and temperature. It also depends on the geometry of the electrochemical cell and the path of the current flow.
2. Double layer capacitance - This capacitance is formed at the interface of the test specimen and the surrounding electrolyte. It forms when the ions in the electrolyte attaches to the surface resulting in a separation of charges between electrolytic ions adsorbed to the electrode surface and electrons in the electrode. The separation between these charges is in the order of Angstroms. The value of double layer capacitance depends on electrode potential, temperature, concentration of ions, types of ions, oxide layer, polish of the surface etc.
3. Polarization resistance - An electrode becomes polarized whenever its potential is changed from its open circuit potential value. Polarization results in current due to electrochemical reactions at the electrode surface. The rate of current flow is controlled by kinetics of the reactions and diffusion of reactants. When there are two simple kinetically controlled reactions, the Butler-Volmer relation between current and potential may be used

$$i = I_0 \exp\left[\frac{E - E_0}{\beta a}\right] - I_0 \exp\left[-\frac{E - E_0}{\beta c}\right]$$

Where I is the current through the cell; I_0 is the corrosion current; E_0 is the open circuit potential of the electrode; E is the potential of the electrode; βa and βc are the tafel slopes of the anodic and cathodic reactions respectively.

The corrosion current may be estimated by fitting the Butler-Volmer relation with the experimentally obtained potential-current curve from LPR. Equating the gradient of the potential-current curve about the corrosion potential from the Tafel plot to the gradient of Butler-Volmer equation, results in the Stern-Geary relation:

$$\frac{\Delta V}{\Delta I} = Rp = \frac{\beta a \, \beta c}{2.303(\beta a + \beta c) I_0}$$

The above equation can be used to estimate corrosion current I0, if the tafel slopes and the polarization resistance are known.

4. Charge transfer resistance - When there is a single kinetically controlled electrochemical reaction present, it gives rise to a charge transfer resistance. When the electrochemical system is at equilibrium, the gradient of overpotential η with respect to exchange current density i_0 about the equilibrium potential is given by the relation

$$Rct = \frac{RT}{nFi_0}$$

Hence the exchange current density can be calculated when charge transfer resistance Rct is known.

5. Diffusion Impedance - Diffusion of ions between metal and bulk solution results in an apparent impedance called the Warburg impedance. At high frequencies Warburg impedance is small since the diffusing reactants do not need to move very far. At lower frequencies the Warburg impedance is high as the reactants have to diffuse farther into the electrolyte.

6. Coating capacitance- The capacitance of the capacitor separated by a dielectric material is given by

$$C = \varepsilon_0 \varepsilon_r \frac{A}{d}$$

Here ε_0 is the permittivity of free space; ε_r is the dielectric constant; A is the area of the parallel plates; D is the separation between plates.

The elements of electrochemical impedance discussed above occur in different series and parallel electronic element combinations and depend on the type of the process. A typical Randles circuit with one time constant for a metal/electrolyte interface is shown in Figure 2.6. The meaning and calculations of the circuit components for a coated metal surface are discussed in a later section.

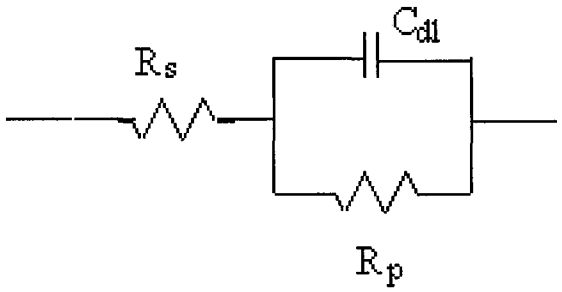

Figure 2.10 Typical Randles circuit.

CHAPTER 3

GENERAL EXPERIMENT PROCEDURES

3.1 Functionalization of Carbon Nanotubes

The as-is produced single wall carbon nanotubes were purchased from Carbolex (AP grade) and refluxed in a dilute solution of nitric acid for 24 hours to remove metal catalyst particles. It was then filtered out and repeatedly washed using a 10 micron Millipore PTFE filter. After drying, the CNTs were functionalized in a vibration cell with a horn probe sonicator. Negatively doped (n-type) tubes were obtained by functionalizing the tubes with PEI (Ethylene imine polymer solution, Mr 600000- 1000000, Fluka). Carbon nanotubes are naturally positively doped (p-type) and functionalization of the tubes was made with SDS (Sodium dodecyl sulfate, FW 288.38, Fisher scientific) [22, 23]. The latter procedure helped separating the tubes from one another, as well. The n- and p- type were embedded in a polymer matrix of PMMA (Poly(methyl methacrylate), intrinsic viscocity 4.0, Polysciences inc) and polyurethane (Waterborne polyurethane varnish, Sherwin Williams), respectively. PMMA was dissolved in toluene (HPLC grade, 99.7% min, Alfa Aesar). P-type tubes were suspended in ethanol (reagent, anhydrous denatured, Sigma Aldrich) and n-type tubes were suspended in DMSO (Dimethyl sufoxide, certified, Fisher scientific). An alternate n-type CNT were obtained using ssDNA (30T single stranded oligo nucleotide in standard desalting, IDT DNA) suspended in DMSO. The DNA wrapped CNTs were subjected to a centrifuge at 5000 rpm for 1 hr followed by several cycles of dialysis at 3000 rpm to remove the excess DNA.

3.2 Thermo-Electric Test

The CNT films were drop-casted on glass slides and tested for their effective doping. The schematic for the thermo-electric (TE) tests is shown in Figure 3.1.

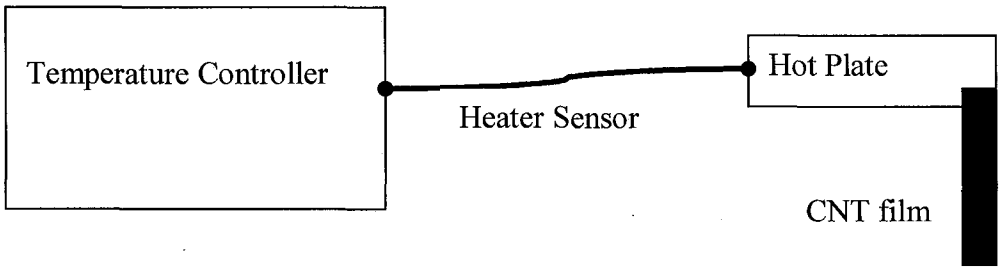

Figure 3.1 Schematic of thermo-electric test setup.

The underlying principle for these tests is called Seebeck effect. In a semiconductor material, there exist free carriers of both types: holes and electrons. In a temperature gradient where one end is hot and the other is cold, excess free charges tend to flow towards the lower temperature. The build up of charges at the cold end develops an electric potential such that there is a repulsive electrostatic force. In steady state conditions, the temperature gradient is counteracted by electrostatic force, so there is no net flow of charge carriers. The electric potential produced by a temperature gradient is called the Seebeck effect. Hence, if the material is p-type, positive charge will build up on the cold side, which leads to a positive potential at the cold end with respect to the hot side. Similarly, if the material is n-type, then negative charge build up at the cold end results in a negative potential at that end with respect to the hot side [38, 39].

3.3 Raman Spectroscopy

Raman spectroscopy is an optical technique used to study vibrational, rotational and other low frequency modes of a molecule. It relies on Raman scattering of a monochromatic light, usually a laser light. The scattered laser light from the molecule is frequency shifted due to the molecular vibrations in direct correlation with the vibration frequency.

Typical Raman spectra for SWCNT have markedly three different characteristic regions (Figure 3.2). One is the high frequency range (1500-1600 cm^{-1}), attributed to tangential vibrational modes of the CNT. Second is in the intermediate-frequency range (1000-1500 cm^{-1}) and due to disordered graphite mode. The third one is in the low frequency range (100-400 cm^{-1}) and is associated with radial breathing mode of vibration. The peak intensities in the low-frequency range correspond to the chirality of the nanotubes [21]. The peak intensities in the high frequency range indicate whether SWCNT is metallic or semiconducting [40].

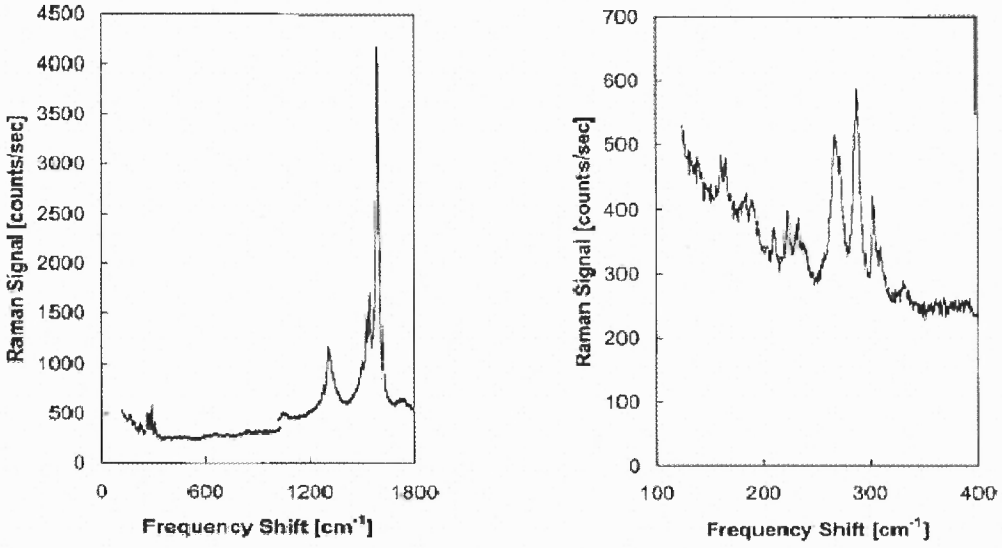

(a) **(b)**

Figure 3.2 Raman Spectra in (a) High and intermediate frequency range (b) Low frequency range.

Experimentally, the spectra were obtained with a back scattering geometry in a confocal arrangement (Figure 3.3). Argon ion laser at 514.5 nm (power density of about 1 kW/cm^2), a 75 cm long SPEX spectrometer equipped with 1200 g/mm grating and an Andor DV401 cooled CCD detector array was used. The spectral resolution of the system was 0.9 cm^{-1}. The laser spot size was 5 μm and the acquisition time was 10 s averaged over 10 scans.

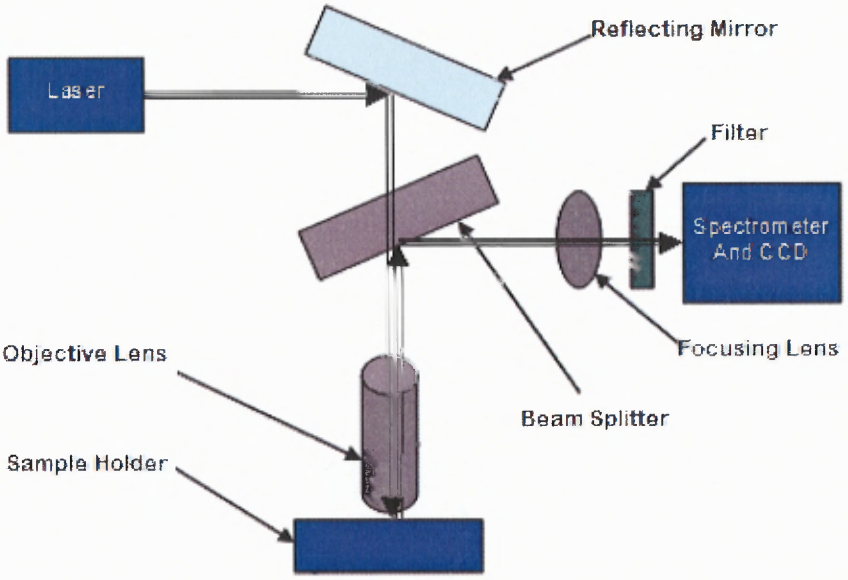

Figure 3.3 Schematic of experimental setup used for Raman spectroscopy.

3.4 Corrosion Test

Four different coatings for AISI 4340 steel substrate were considered. Chapter 4 describes steel coatings with electronic p-n junctions. Chapter 5 deals with electronic transistor-like structures. In chapter 6 graphene as an intermediate layer is described and finally Chapter 7 discusses the bio-electronic structures.

CHAPTER 4

DIODE-LIKE ELECTRONIC STRUCTURE COATINGS

4.1 Introduction

A new concept of anti-corrosion coating is considered. Successive layers were placed on the metal to be protected, such that an electronic *p-n* junction was formed. The resultant electronic barrier was made by layering one type of functionalized semiconducting carbon nanotube over another. Electrochemical current was impeded, at least in part, by the formation of such barrier. Potentiodynamic measurements, Raman spectroscopy, impedance measurements and scanning electron microscopy with energy dispersive x-ray spectroscopy were used to assess the corrosion process. The layer ordering (*p-n* or *n-p* with respect to the metal electrode) determined the corrosion rate in de-ionized (DI) water. Only temporary resistance was found in the presence of 3.5 wt% NaCl solution.

In the past, passive films with semiconducting properties were considered [11, 50]. These were oxide films, typically on metal such as Cr, which exhibit various degree of *n*-type doping depending on the method of formation used (typically, by applying a biasing potential during oxidation). Conducting polymers as corrosion protecting films over steel substrates have also been used [10]. CNT metal composites have been used as anti-corrosion coatings [19] due to their adsorbability, nanoscale effects and electrical conductivity. A different approach is undertaken here: CNT based electronic structures were deposited on the metal to be protected. Hence, the surface morphology of the metal is not changed. The coatings remain *p*- and *n*-types irrespective of applied voltage due to

functionalization of CNTs. The fabrication methods are simple, may be applied on a large scale and the concept is general.

4.2 Experiment

4.2.1 Current-Voltage Characteristics of *p-n* Junctions

A *p*-type CNT film was deposited on a glass slide and was topped with an *n*-type CNT film (Figure 4.1). Keithley 2400 source meter, interfaced with a computer was used to measure the current-voltage characteristics. The voltage was varied from -2 V to +5 V at steps of 20 mV. The corresponding current values were then collected.

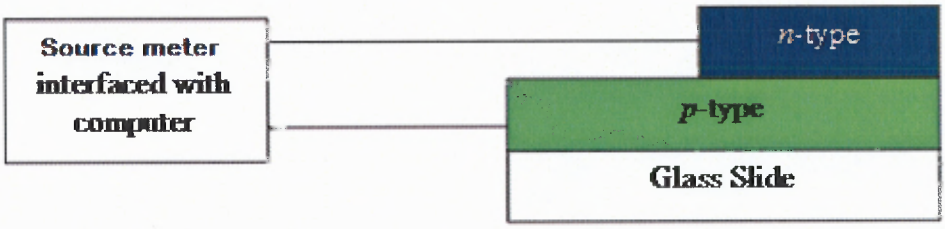

Figure 4.1 Schematic to measure current-voltage characteristics for *p-n* junction.

4.2.2 Substrate Preparation

AISI 4340 steel pieces of dimension 1.2cm X 1.2cm X 0.5cm served as working electrodes. The steel substrates were polished by emery paper of different grades and finally with 1200 grit, until a fairly smooth surface was obtained. It was then put in an acetone (≥99.5% A.C.S. reagent, Sigma Aldrich) sonicator bath for 20 minutes to remove the adhered grit and washed with DI water (ASTM type II, Aqua solutions). Successive films were each drop-casted and let dry out before laying out the next film on top of it to obtain steel-*p*-*n* and steel-*n*-*p* structures. The electrolyte used was either DI water of very

high resistivity and pH varying between 5 and 7 or, 3.5 wt% NaCl solution with low resistivity and pH of 5.5.

4.2.3 Electrochemical Tests

Schematic of the experimental setup is shown in Figure 4.2. It is a conventional three-terminal cell with coated steel substrate serving as the working electrode, platinum wire serving as the counter electrode and Ag/AgCl reference electrode. The bottom of the electrochemical cell has a circular opening with a contact area of 0.28 cm^2 interfacing the working electrode with a Kalrez O-ring.

Polarization measurements were carried out using EG&G Princeton Applied Research model 273 potentiostat/galvanostat system. The potential of the working electrode was scanned from -1000 mV to +500 mV at steps of 10 mV/sec. AC impedance tests were performed using CHI 760C electrochemical workstation. Measurements were carried out in 1 Hz- 100 KHz frequency range with an AC perturbation signal of 5 mV. Current-voltage characteristics of the diode and transistor-like structures were measured using Keithely 2400 source meter. Samples were also assessed by scanning electron microscope (SEM) along with energy dispersive X-ray (EDX) spectroscopy.

4.3 Results

Thermo-electric potentials are indicated in Table 1. CNT embedded in polyurethane matrix exhibits a greater thermal voltage developed for 52 ^{o}C temperature difference compared to the regular PVP wrapped CNT films. Negative type films (*n*-type) for PEI wrapped CNT, which were imbedded in PMMA matrix, exhibited a larger thermo-

electric voltage than only PEI wrapped CNT, probably due to a larger resistance of the film. DNA wrapped CNT exhibited the largest thermo-electric voltage among the three n-type films.

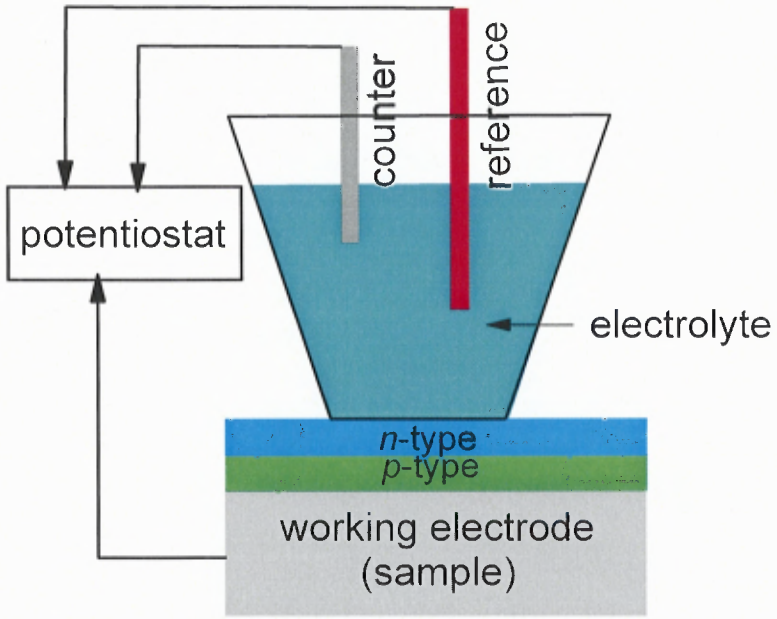

Figure 4.2 Block diagram of the measurement and control setup: polarization characterizations were performed using a potentiostat. Data acquisition and control was simultaneously provided by a computer.

Raman spectra of the CNT coated working electrode are shown in Figure 4.3. They exhibited G^+ peaks at 1593.57 cm^{-1} and 1594.74 cm^{-1}, for *p*-type and *n*-type, respectively. This peak was not shifted for the various types, as expected. The G^- peaks indicate semiconducting characteristics (1569 cm^{-1} and 1566 cm^{-1} for *p*-type and *n*-type, respectively) with a small down-shift for the more negatively charged *n*-type tubes [44].

Current-voltage characteristic of *p-n* junction on a glass substrate is shown in Figure 4.4. The junction was fabricated by overlaying functionalized CNT, which were dispersed in a polymer matrix, on one another (Figure 4.1). The curve exhibits typical junction characteristics, thus demonstrating a fairly good step-junction with a depletion region ideality factor of 1.7 (see Section 1.5). It also exhibits a large diode resistance.

Table 4.1 Thermo-electric Measurements at ΔT=125 °F on *p*- and *n*-type CNT

	*p*CNT	*n*CNT
Non-refluxed carbolex	-0.075 mV/cm	0.144 mV/cm
Refluxed carbolex	-0.179 mV/cm for SWCNT/PVP -0.323 mV/cm for SWCNT/Polyurethane	0.049 mV/cm for SWCNT/PEI 0.067 mV/cm for SWCNT/PEI/PMMA 4.843 mV/cm for SWCNT/ssDNA

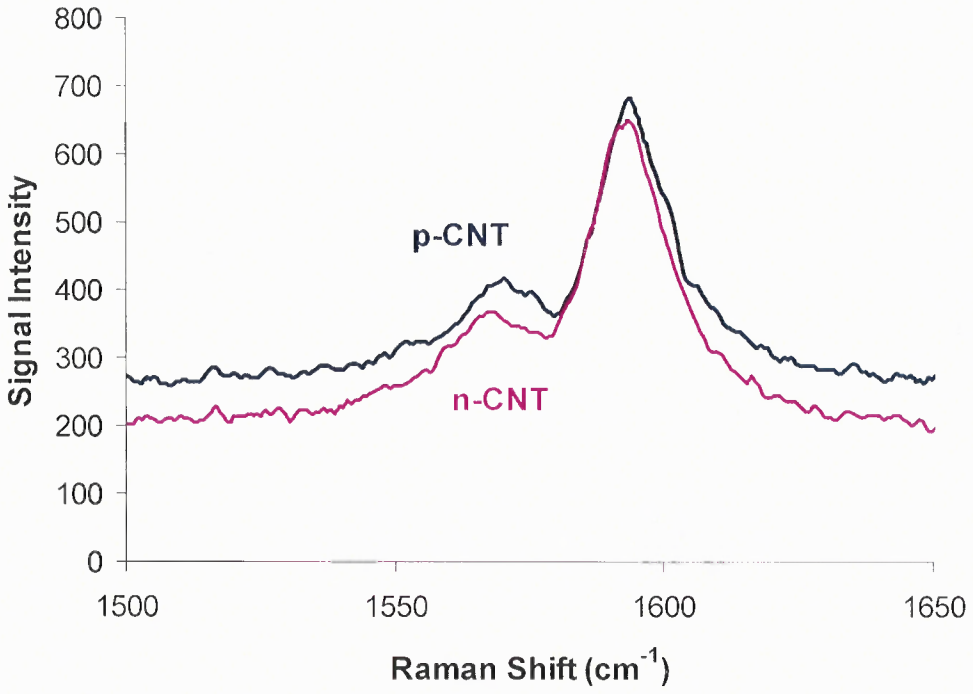

Figure 4.3 Raman spectra for *p*- and *n*- type CNT.

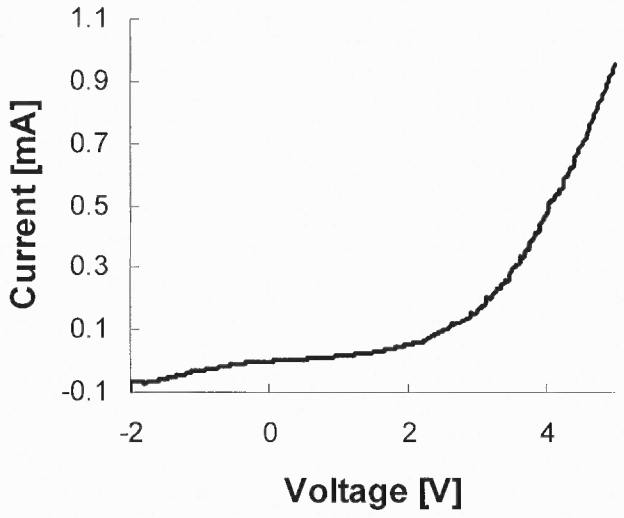

Figure 4.4 Current-voltage characteristics of a *p-n* junction on glass.

Anodic reaction (corrosion) took place at the working electrode as seen in Figure 4.5. Shown are optical microscope pictures for the steel-*p*-*n* and steel-*n*-*p* cases. Spots of rust on the steel surface covered the sample of steel-*n*-*p*. This is in contrast to the case of steel-*p*-*n*, where no, or, minimal rusting was observed. Scanning electron microscope (SEM) images with related energy dispersive X-ray (EDX) spectroscopy are provided in Figure 4.6.

Tafel plots (Figure 4.7) for steel-*n*-*p* indicated that the corrosion potential was Ecorr=–440 mV, similar to the corresponding value for bare steel (see also Table 4.2).

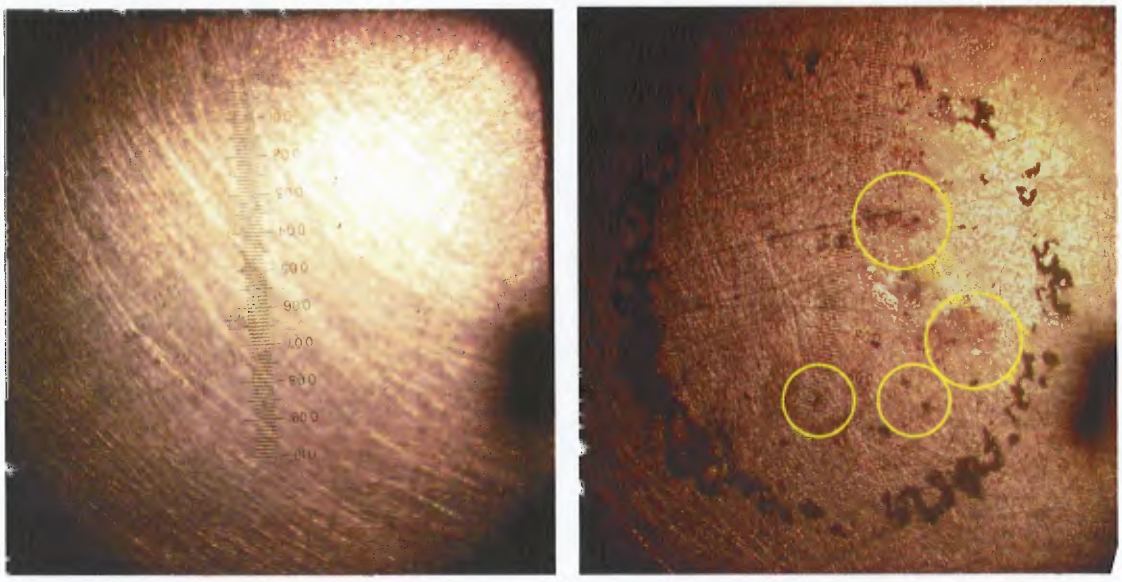

(a) (b)

Figure 4.5 Optical Microscope pictures of (a) steel-*p*-*n* (steel-CNT/PVP-CNT/PEI) and (b) steel-*n*-*p* (steel-CNT/PEI-CNT/PVP): electrolyte was DI water. Corrosion spots are marked by circles. (Scale 0.01 division =1 mm).

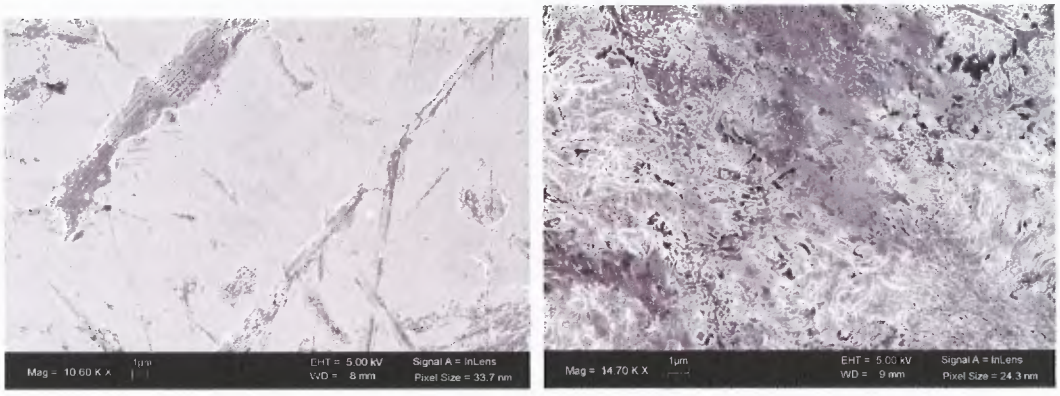

Steel-*p*-*n*		
Element	Weight%	Atomic%
C	2.98	11.21
O	5.13	14.48
Fe	91.89	74.32
Total	100.00	

(a)

Steel-*n*-*p*		
Element	Weight%	Atomic%
C	3.34	13.05
O	2.75	8.06
Fe	93.91	78.88
Total	100.00	

(b)

Figure 4.6 SEM and EDX results of (a) steel-*p*-*n* (steel- CNT/PVP- CNT/PEI) and steel-*n*-*p* (steel- CNT/PEI- CNT/PVP) in DI water.

This is not the case for steel-*p*-*n* where Ecorr= +8 mV. As indicated by Table 4.2, Ecorr values for either *p*-type or *n*-type on glass were positive. The value for either coating on steel was also more positive than for bare steel.

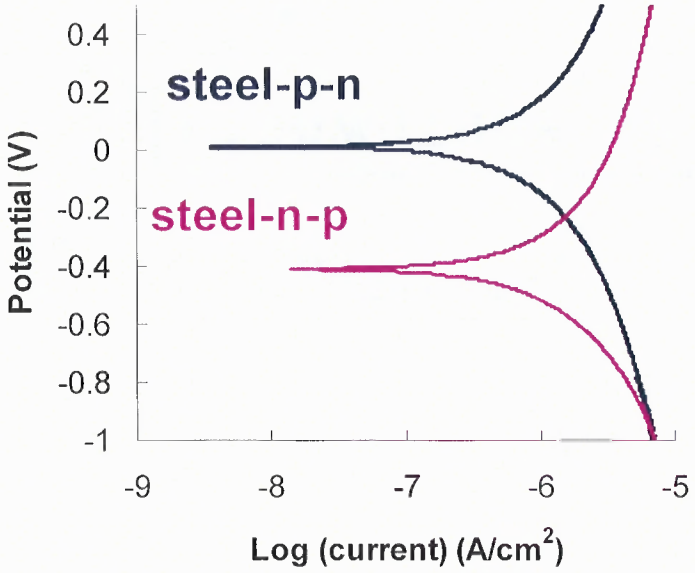

Figure 4.7 Tafel plots of steel-*p*-*n* (steel-CNT/PVP-CNT/PEI) (blue curve) and steel-*n*-*p* (steel-CNT/PEI-CNT/PVP (pink curve) in DI water. Corrosion potential of steel-*p*-*n* is more positive compared to corrosion potential of steel-*n*-*p*.

The situation is clearer when the CNT films are loaded into inert polymeric matrices, such as polyurethane (for p-type CNTs) and mix the CNT with PEI and poly(methyl methacrylate) (PMMA) for n-type films (see also Table 4.1 for film quality). The optical microscope pictures, corresponding SEM/ EDX results are shown in Figures 4.8 and 4.9. Optical microscope picture shows corrosion spots on steel-n-p in comparison to steel-p-n. Tafel plots are shown in Figure 4.10. The corrosion potential of steel-p-n is anodic to the corrosion potential of steel-*n*-*p*.

Table 4.2 Corrosion Potentials of Coated Glass or Steel in DI and 3.5% NaCl Solutions

	Ecorr for DI water	Ecorr for 3.5 wt% NaCl
Glass-p	+274 mV	-377 mV
Glass-n	+122 mV	-115 mV
Glass-p-n	-56 mV	-228 mV
Glass-n-p	+66 mV	-154 mV
Steel-p	-139 mV	-790 mV (Ic@-440 mV)
Steel-n	+162 mV	-814 mV (Ic@-480 mV)
Steel-p-n	+8 mV (CNT/PVP-CNT/PEI)	-773 mV (Ic@-480 mV)
Steel-n-p	-410 mV (CNT/PVP-CNT/PEI)	-775 mV (Ic@-555 mV)
Steel-polyurethane-PMMA	-669 mV	-974 mV (Ic@-573 mV)
Steel-PMMA-polyurethane	-694 mV	< -1000 mV
Steel-p-n	-385 mV (CNT/polyurethane – CNT/PEI/PMMA)	-928 mV (Ic@-504 mV)
Steel-n-p	-400 mV (CNT/polyurethane - CNT/PEI/PMMA)	-885 mV (Ic@-445 mV)

Note: The top portion is non-imbedded CNT films. The lower portion is for CNT imbedded polymeric films.

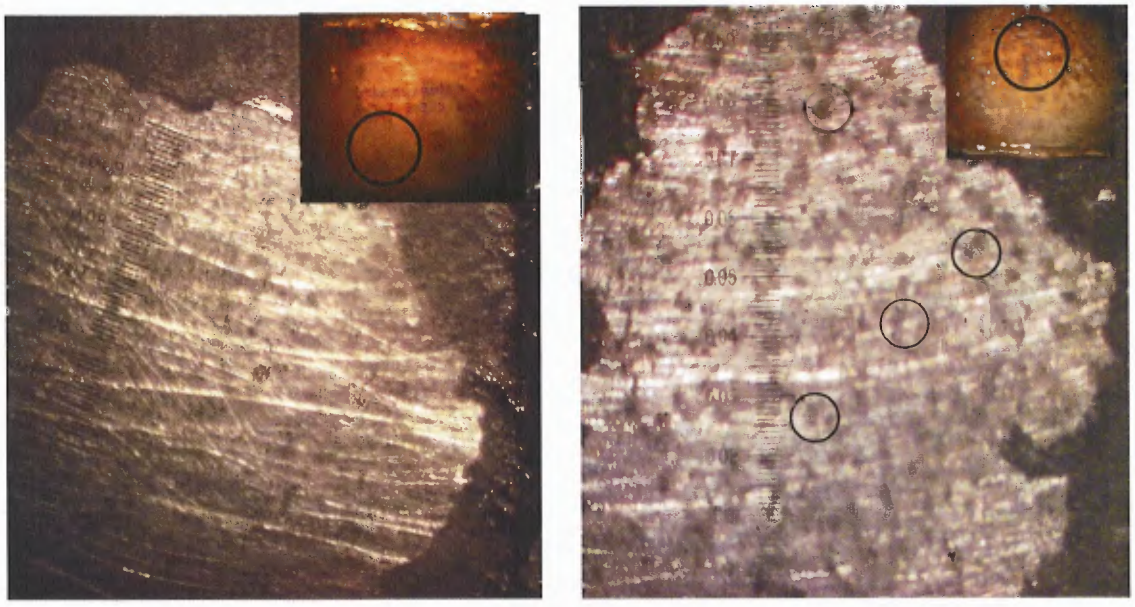

(a) **(b)**

Figure 4.8 Optical Microscope pictures of (a) steel-*p-n* (steel-CNT/Polyurethane-CNT/PEI/PMMA) and (b) steel-*n-p* (Steel-CNT/PEI/PMMA-CNT/Polyurethane): electrolyte was DI water. Corrosion spots are marked by circles. Insets: (a) steel-polyurethane-PMMA. (b) steel-PMMA-polyurethane. (Scale 0.01 division =1 mm).

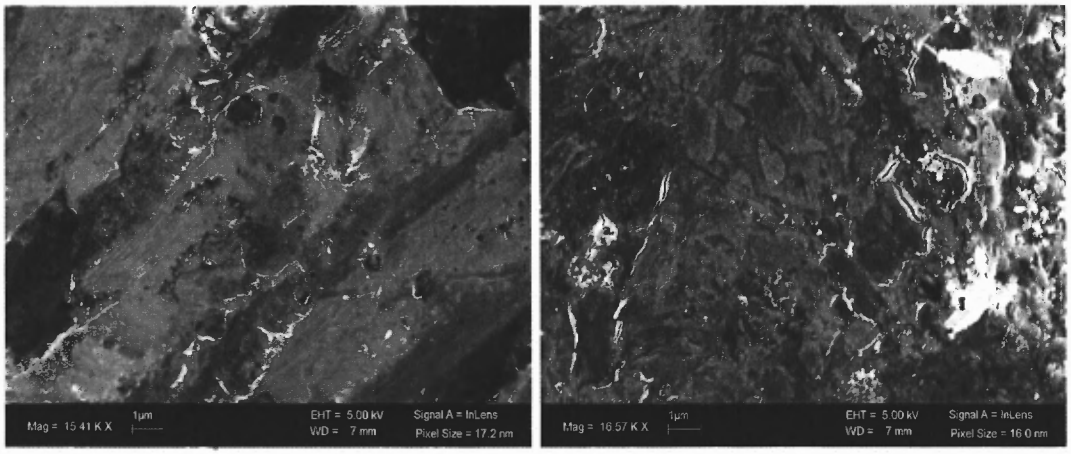

Steel-*p*-*n*		
Element	Weight%	Atomic%
C	3.36	11.95
O	7.47	19.93
Fe	89.16	68.12
Total	100.00	

(a)

Steel-*n*-*p*		
Element	Weight%	Atomic%
C	8.64	22.10
O	20.18	38.75
Fe	71.18	39.15
Total	100.00	

(b)

Figure 4.9 SEM and EDX results of (a) steel-*p*-*n* (steel- CNT/polyurethane - CNT/PEI/PMMA) and steel-*n*-*p* (steel- CNT/PEI/PMMA- CNT/polyurethane) in DI water. An increase in oxygen percentage observed for steel-*n*-*p*.

The situation with 3.5 wt% NaCl solution was more complex. Grayish pitted surface was observed for both steel-*p*-*n* and steel-*n*-*p* samples. However, optical microscope pictures indicated that the steel-*n*-*p* sample suffered heavier corrosion compared with the steel-*p*-*n* sample (Figure 4.11) [45]. SEM/ EDX pictures and Tafel plots are shown in Figures 4.12 and 4.13. Here, the corrosion potential of steel-*p*-*n* is more positive compared to corrosion potential of steel-*n*-*p* similar to the previous case. In the polymer embedded CNTs, the steel-*n*-*p* corrosion potential was more positive compared to steel-*p*-*n* (Figure 4.16). The corresponding SEM/EDX results are shown in Figures 4.14 and 4.15.

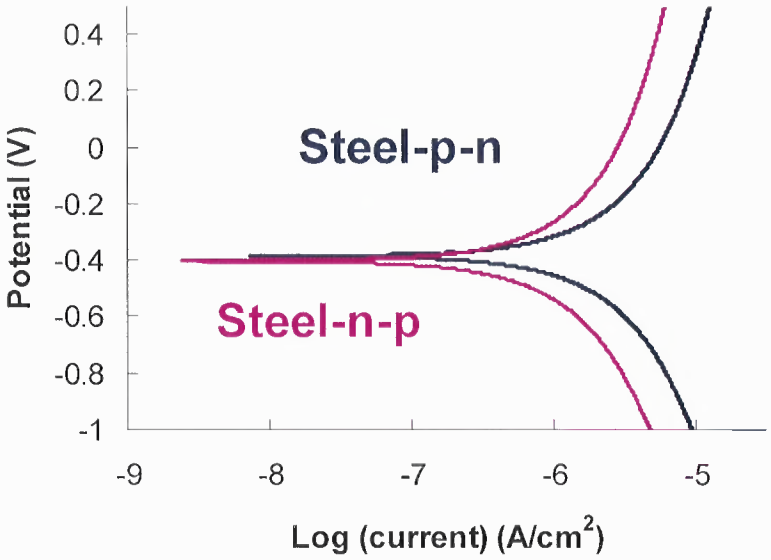

Figure 4.10 Tafel plots of steel-*p*-*n* (steel-CNT/Polyurethane-CNT/PEI/PMMA), blue graph and steel-*n*-*p* (steel-CNT/PEI/PMMA-CNT/Polyurethane), pink graph in DI water. Steel-*p*-*n* corrosion potential is anodic compared to steel-*n*-*p*.

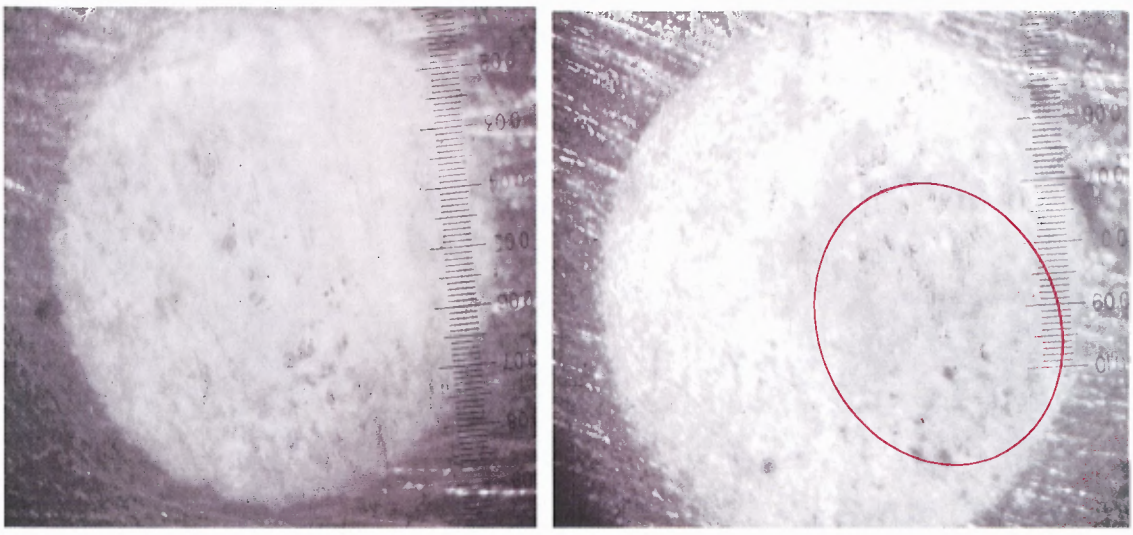

(a) **(b)**

Figure 4.11 Optical microscope pictures of (a) steel-*p*-*n* (steel-CNT/PVP-CNT/PEI) and (b) steel-*n*-*p* (steel-CNT/PEI-CNT/PVP) in 3.5% NaCl Solution. Steel-*n*-*p* has an underlying dark hue indicated by the arrow. (Scale 0.01 division =1 mm).

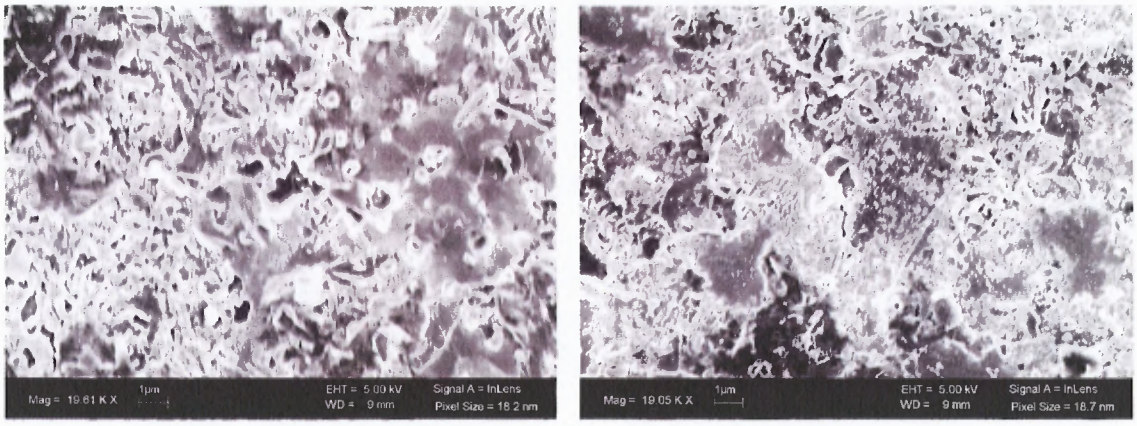

Steel-*p*-*n*		
Element	Weight%	Atomic%
C	4.67	18.06
O	1.31	3.80
Fe	94.02	78.14
Total	100.00	

(a)

Steel-*n*-*p*		
Element	Weight%	Atomic%
C	15.02	37.42
O	12.76	23.87
Fe	72.22	38.70
Total	100.00	

(b)

Figure 4.12 SEM and EDX results of (a) steel-*p*-*n* (steel- CNT/PVP - CNT/PEI) and steel-*n*-*p* (steel- CNT/PEI - CNT/PVP) in 3.5 wt% NaCl solution. An increase in oxygen percentage observed for steel-*n*-*p*.

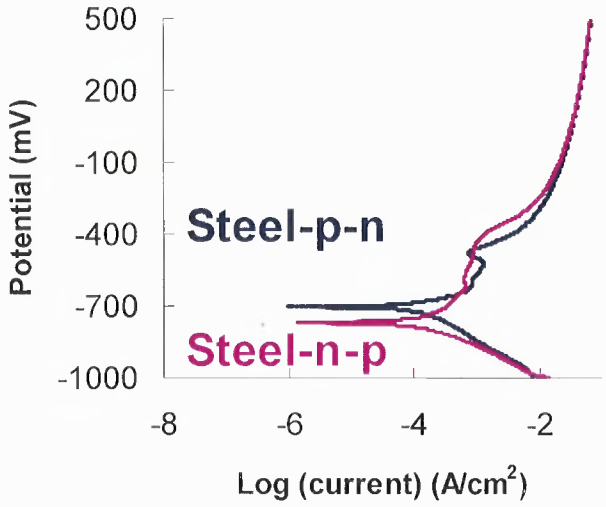

Figure 4.13 Tafel plots of steel-*p*-*n* (steel-CNT/PVP-CNT/PEI), blue graph and steel-*n*-*p* (steel-CNT/PEI-CNT/PVP), pink graph in 3.5 wt% of NaCl solution. Steel-*p*-*n* corrosion potential is anodic compared to steel-*n*-*p*.

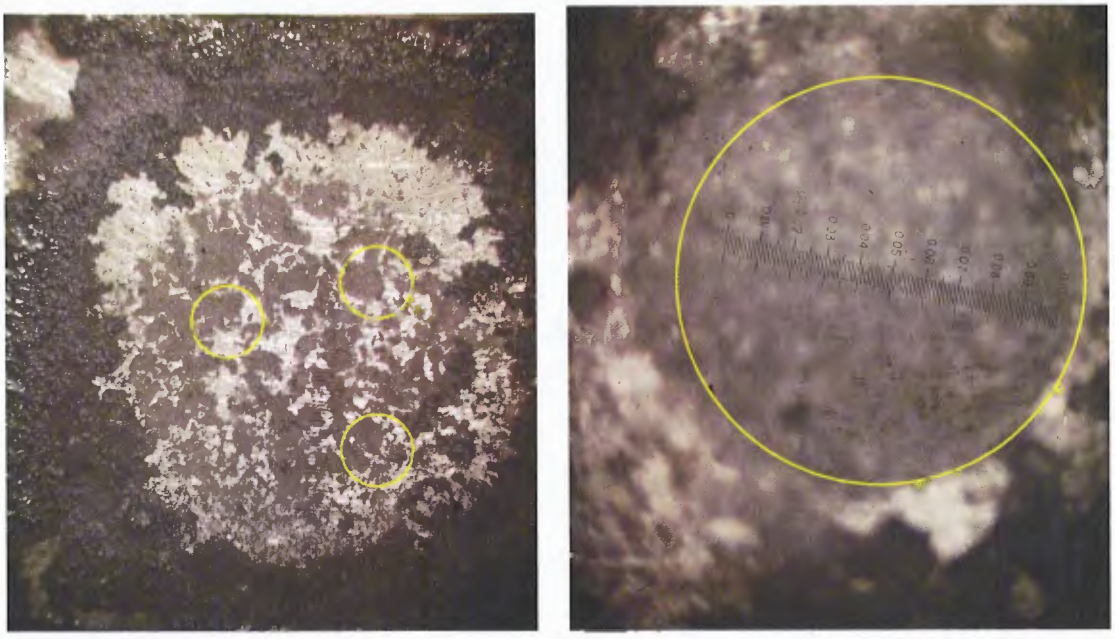

(a) **(b)**

Figure 4.14 Optical microscope pictures of (a) steel-*p*-*n* (steel-CNT/polyurethane - CNT/PEI/PMMA) and (b) steel-*n*-*p* (steel-CNT/PEI/PMMA-CNT/polyurethane) in 3.5% NaCl Solution. Corrosion spots are marked by circles. (Scale 0.01 division =1 mm).

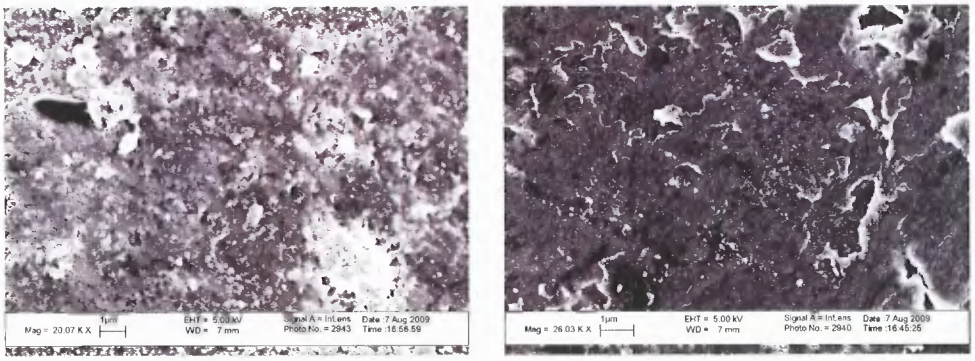

Steel-*p*-*n*		
Element	Weight%	Atomic%
C	64.90	77.67
O	20.74	18.63
Fe	14.37	3.70
Total		

(a)

Steel-*n*-*p*		
Element	Weight%	Atomic%
C	47.91	67.83
O	21.50	22.85
Fe	30.58	9.31
Total		

(b)

Figure 4.15 SEM and EDX results of (a) steel-*p*-*n* (steel- CNT/polyurethane - CNT/PEI/PMMA) and steel-*n*-*p* (steel- CNT/PEI/PMMA - CNT/polyurethane) in 3.5 wt% NaCl solution. An increase in oxygen percentage observed for steel-*n*-*p*.

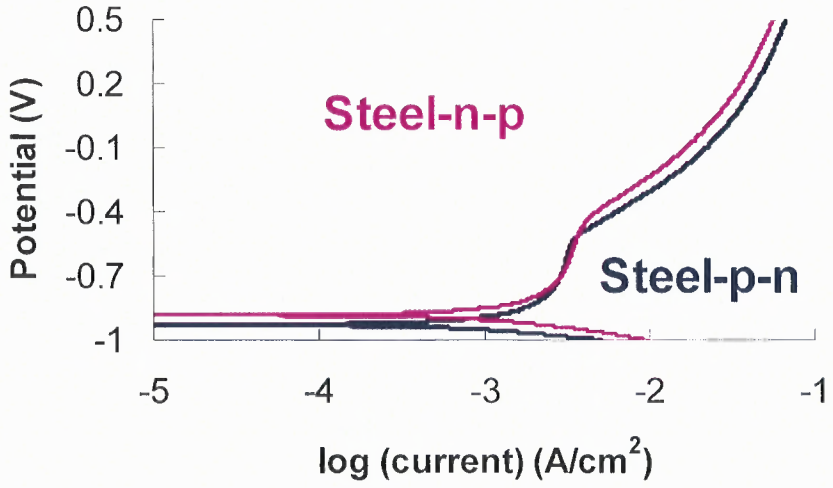

Figure 4.16 Tafel plots of steel-*p*-*n* (steel-CNT/polyurethane -CNT/PEI/PMMA), blue graph and steel-*n*-*p* (steel-CNT/PEI/PMMA-CNT/polyurethane), pink graph in 3.5 wt% of NaCl solution. Steel-*p*-*n* corrosion potential is anodic compared to steel-*n*-*p*.

4.4 Discussion

The anodic and cathodic Tafel slopes were obtained from graphs in Figures 4.7 and 4.10. The corrosion current was obtained following Equation 4.1.

$$Icorr = \frac{\beta a \cdot \beta c}{2.303(\beta a + \beta c) \cdot Rp} \qquad [4.1]$$

Here βa is the Tafel slope of the anodic reaction in V/decade, βc is the Tafel slope of cathodic reaction in V/decade and Rp is the polarization resistance in $\Omega.cm^2$. Equation 4.2 was used to obtain the corresponding corrosion rate CR,

$$CR = 3.1510^{7} \cdot \left(\frac{Icorr \cdot M}{F \cdot Z \cdot D} \right) \qquad [4.2]$$

Here the corrosion rate CR is in μm/y; Icorr is the corrosion current in A/m^2; M= 55.847 g/mole is the molecular weight of iron; F= 96490 C/equivalent is the Faraday's constant; Z=2 is the valence state of iron metal in oxidized form and D= 7.874 g/cm^3 is the density of iron metal.

Calculated corrosion currents (shown in parentheses) for the cases of steel-*p*-*n* and steel-*n*-*p* are tabulated in Table 4.3 for DI water. One immediate striking data is the larger corrosion rates exhibited by some coated samples compared to the bare steel. This not only defies the intuition but also is in clear contradiction to the experiments. This issue may be explained by understanding the various semiconductor/electrolyte interfaces.

Table 4.3 Corrosion Current and Corrosion Rate Comparison of Diode-like Coatings in DI Water

	Corrosion current Icorr (in nA/cm^2)	**Corrosion rate CR (in μm/yr)**
Bare Steel	58	0.67
Steel-p (PVP/CNT) - n(PEI/CNT)	4 (86)	0.05 (0.99)
Steel-n(PEI/CNT) - p(PVP/CNT)	3.7 (61)	0.04 (0.7)
Steel-Polyurethane - PMMA	96	1.1
Steel-PMMA - Polyurethane	127	1.5
Steel-p(Polyurethane/CNT) - n(PMMA/PEI/CNT)	2.5 (328)	0.03 (3.8)
Steel-n(PMMA/PEI/CNT) - p(Polyurethane/CNT)	4.7 (174)	0.06 (2)

Note: The uncorrected values are indicated in the parentheses. The fitting error for all values, with the exception of steel-polyurethane-PMMA and steel-PMMA-polyurethane, was ±5%. The measurement error in these two cases was ±20%. The scattering of the Tafel slopes was remarkably small, within 5%.

Surface studies have shown that *n*-type semiconductors in the form of naturally occurring oxide on metal surfaces are able to impede the migration of anions (OH^-) towards the metal surface [49-50]. The negatively-doped film effectively increases the negative charges at the metal surface thus, impeding an anodic reaction of the form, Fe

$\rightarrow Fe^{2+} + 2e^-$. Likewise, a positively doped semiconductor layer at the metal surface might increase the corrosion as the number of negatively charged carriers is effectively reduced. Such considerations may be observed by the changes in the surface potential for DI water when the metal is coated with either *p*-type or, *n*-type semiconductor films (Table 4.2). Instead of a single semiconductor layer, a case may be made for a junction of choice, which will be fabricated on the metal surface to further impede the corrosion process. Such junction would be independent of the naturally occurring contact between a metal and *n*-type oxide film (for example between chromium oxide and chromium). This is the core idea of the present study.

The corrosion current values should not be attributed to only corrosion of the metal electrode. The junction itself contributes to the current, as well as to the surface potential, as it may observed by the Ecorr values for *p-n* junction on glass. The band diagram for metal/semiconductor interface is shown in Figure 4.17 and the effective band diagram for a steel-*p-n* junction is shown in Figure 4.18. The *n*-type CNT film is in contact with the electrolyte. The electrons redistribute away from the *n*-type/electrolyte interface resulting in an increase of the space charge region. The accumulation of these electrons at the *n-p* junction increases the double layer capacitance between the metal and film (Table 4.3), thus increasing the capacitive (non-Faradaic) current. Such excess charge concentration inhibits (screens) the anodic reaction $Fe \rightarrow Fe^{2+} + 2e^-$ and the reduction of oxygen O_2 (g) + $2H_2O$ + $2e^- \rightarrow 4OH$. Overall, the corrosion process is decreased; there might be a possibility for localized corrosion due to imperfect films and migration of harmful anions such as OH^- towards the metal surface [50]. On the other hand, in steel-*n-p* configuration, holes at the space charge region near the *p*-

type/electrolyte interface, experiences band lowering thus providing electrons to the reduction of oxygen. Here, the current may be attributed to the corrosion of metal. Similar arguments apply to steel-*n* and steel-*p*. Steel-*n* has exhibited smaller number of rust spots than steel-*p* (also attributed to its larger Ecorr value), yet overall, both coatings may deem ineffective compared to steel-*p*-*n*.

For DI water, the *p*-type film has more positive (larger) Ecorr compared to *n*-type film when on glass interfacing the water. The situation is reversed when placed on steel. The impact of the film order on the surface potential in water further suggests its impact on the corrosion of the metal underneath it. The situation for 3.5% NaCl is mixed and when on steel, the Ecorr value is almost independent of the order of the films, again suggesting that the barrier is ineffective when the ion concentration is large.

Rust was evident underneath the thin polyurethane and PMMA coatings of steel regardless of the film ordering (Figure 4.8 insets). On the other hand, when wrapping the CNT, the polymeric films were strong and uncompromised. It is noted that the unlike the passive films, both the non-imbedded and the imbedded structures are porous, with pore size estimated at a few tens of nm. Therefore, it is clear that steel-*p*-*n* structures may not suppress corrosion in DI water by simply blocking transport of all ions. Overall, larger corrosion currents were associated with the junctioned films in comparison with its passive counterparts. This is in contrast to the optical and SEM pictures.

Let us attempt to exclude the non-Faradaic effects. The latter have been measured directly when placing the junctions on glass. It is assumed that to the first order of approximation, the Faradaic and non-Faradaic components contribute linearly to the corrosion process. One cannot simply subtract corrosion currents or, rates because these

depend on the particular samples used. Instead, it is observed that the kinetics of the corrosion process is in the coefficient β below. As noted earlier, these coefficients were similar for pH of water between 5 and 7. Starting with equation 4.1, where the anodic and cathodic tafel slopes can be written as,

$$\beta a=\beta a1+\beta a2; \quad \beta c=\beta c1+\beta c2. \qquad [4.3]$$

Here βa1 and βa2 are the anodic slopes for the Faradaic and non-Faradaic components, respectively. Likewise, βc1 and βc2 are the cathodic slopes for the Faradaic and non-Faradaic components, respectively. Experimentally, βa was assessed for the steel samples and βa2 was assessed for junctions placed on glass (and likewise, βc and βc2). Such considerations do not take band bending effects between films and metal, yet, do implicitly take band bending at the film/electrolyte interface into account. One is able to consider the 'net' Faradaic effect by evaluating βa1 and βc1 through Equation 4.3 and plugging its values in Equation 4.1. The value for Rp is assessed from the AC impedance measurements as typically made [37]. The corresponding corrosion rate is then calculated using equation 4.2 with the corrected value for corrosion current. The corrected corrosion rates are given in Table 4. The advantage of the junctioned films over bare steel is clear. Moreover, the corrosion protection of imbedded *p-n* on steel over just passive polymers is also evident.

The situation with 3.5 wt% NaCl solution was more complex. Grayish pitted surface was observed for steel-*p-n* and steel-*n-p* samples (Figure 4.11, 4.14) for both the non-imbedded and imbedded forms. SEM pictures (Figure 4.12, 4.15) also show a large number of pits. The EDX data exhibited large content of carbon and oxygen as if the steel

electrode was masked by a carbon-based and oxide species. This is clearer for the polymer-imbedded junctions.

Tafel plots are presented in Figures 4.13 and 4.16. As expected, there are two corrosion peaks: one for the critical current at the steel surface potential (–440 mV), indicating a thick passive layer formation and the other representing the corrosion potential at –750 mV [61]. The film on glass did not show oxidation characteristics: these plots are attributed to non-Faradaic effects. Correcting the data for non-imbedded films with the related data for films on glass yielded: 20 μm/yr for steel-*p*-*n* (32 μm/yr uncorrected); 9 μm/yr for steel-*n*-*p* (16 μm/yr uncorrected) and 987 μm/yr for bare steel. The data indicates the advantage of coated steel in comparison with bare steel. The correction seems to imply an advantage of steel-*n*-*p* samples, which could not be fully verified by the optical microscope, or SEM pictures.

In the presence of large ion concentration, as is the case for 3.5% NaCl solution, the screening potential across the *p*-*n* junction is less effective. Therefore, the corrosion appears to be uniform and less localized in comparison with DI water. Optical pictures qualitatively allude to the advantage of steel-*p*-*n* structures, and specifically, the polymer imbedded structures over steel-*n*-*p*. Correcting the data for the non-Faradaic effects was not as effective as for the case with the DI water: corrosion rates quantitatively alluded to the advantage of steep-*n*-*p* compared with steel-*p*-*n*.

In summary, unlike conventional passive protecting films, junction based structures impede corrosion through electronic barriers rather than blocking of all ion species. While not fully optimized at this stage, such construction opens the door for new corrosion protection methods and electronic monitoring of breach in the protecting films.

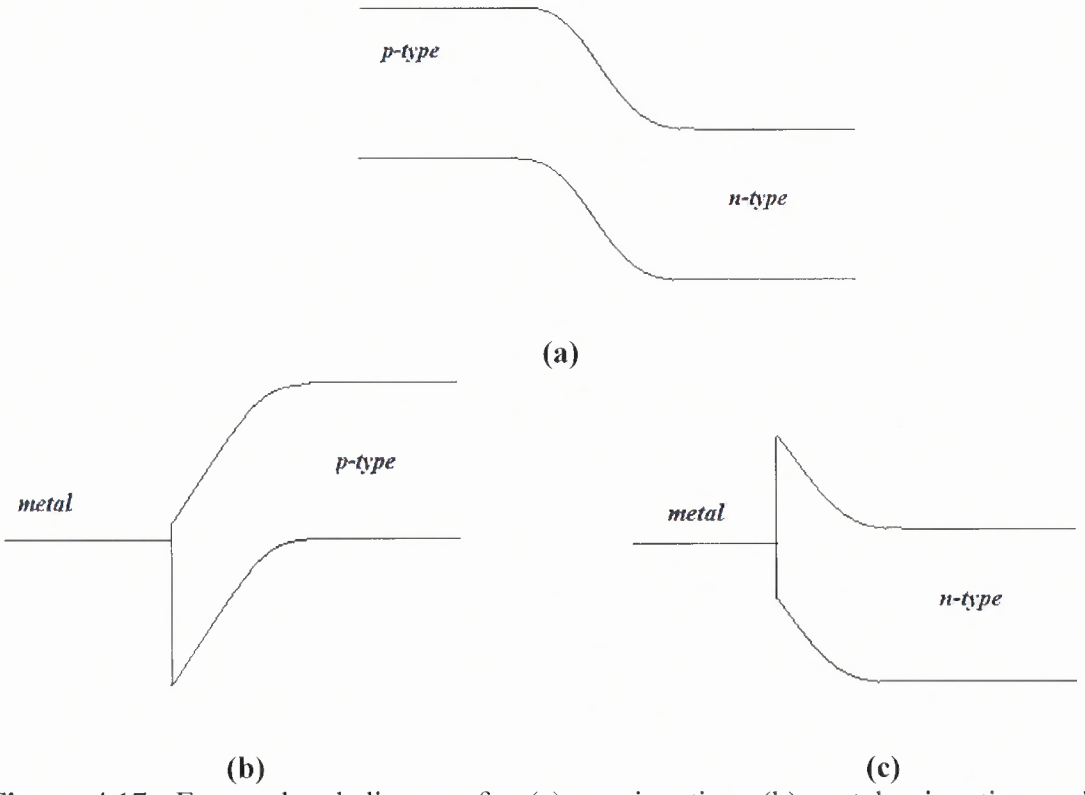

Figure 4.17 Energy band diagram for (a) *p-n* junction, (b) metal-*p* junction and (c) metal-*n* junction. (For electrolyte/semiconductor interface see Section 1.4).

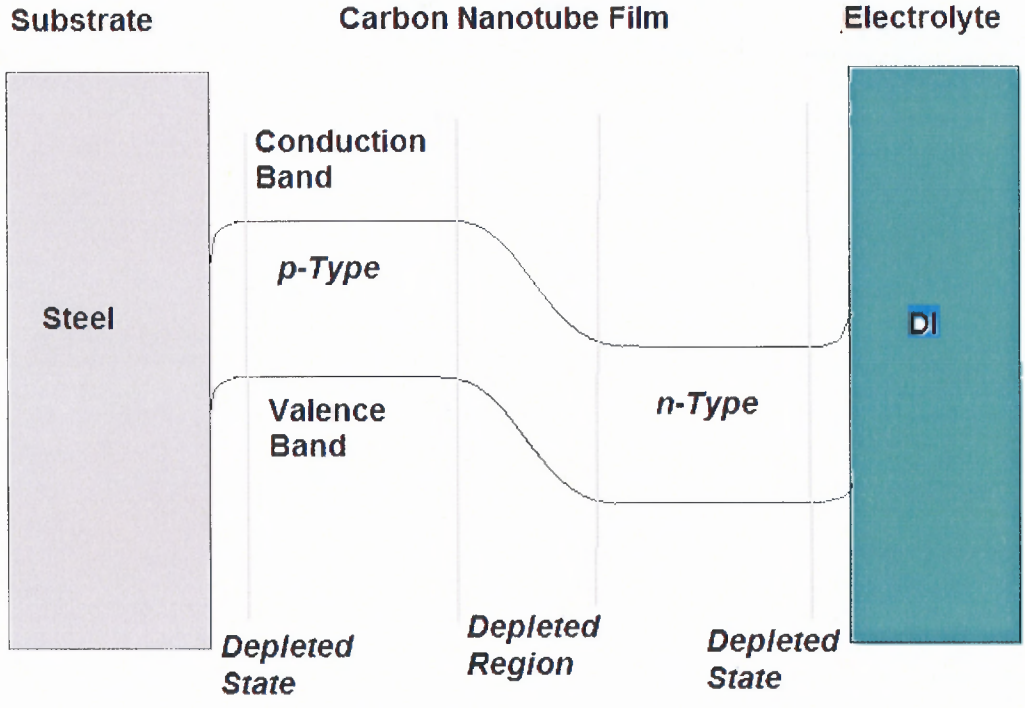

Figure 4.18 Overall band diagram of a steel-*p-n* working electrode in contact with electrolyte.

CHAPTER 5

TRANSISTOR-LIKE ELECTRONIC STRUCTURE COATINGS

5.1 Introduction

Control scheme of ionic currents in a new semiconductor-ionics concept is proposed. This is achieved by introducing a permeable, multi-layered structure which has electronic doping, of *p-n-p* or *n-p-n* between the typically two biasing electrodes in a three terminal electrochemical cell. Ionic currents were controlled by applying a fixed base voltage between the middle layer and an outer (working) electrode and varying the potential between the two outer electrodes (or by varying the overpotential of the working electrode). Corrosion processes were demonstrated for this configuration; however, such construction may be useful for other membrane type applications also.

Imbedding microelectronic concepts in electrochemistry and biochemistry has been implemented mainly by two common concepts: 1. a gate potential is used to control ions in an isolated and inherently charged, nano-channel or, 2. ions in the solution are affecting the gate potential of an otherwise pure electronic device (for example, Ion Selective Field-Effect Transistor, or, ISFET [52, 59-60]). In contrast, here a different approach is proposed whereby ionic current is driven across a (permeable) structure similar to the construction of bipolar junction transistor (BJT). The control over the ionic current is made by applying electronic current at the base of the BJT thus, changing the *electronic* band structure.

5.2 Experiment

5.2.1 Current-Voltage Tests

The schematic of the *n-p-n* junction on a glass slide is shown in Figure 5.1. The base voltage was varied from 0 V to 1 V in steps of 0.1 V. For each base voltage the potential between the collector and the emitter was scanned between 0 V to +5 V and the corresponding values of current were recorded.

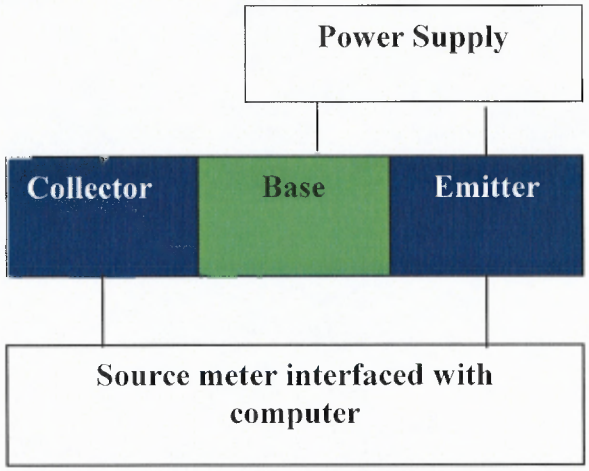

Figure 5.1 Schematic for measuring current-voltage characteristics for transistor structure.

5.2.2 Substrate Preparation

The substrate was prepared as described in Section 4.2.1 to obtain steel-*p-n-p* and steel-*n-p-n* structures. Schematic of the experimental setup is shown in Figure 5.2. The experiment method is as described in Section 4.2. The base voltage was applied in steps of 0.1 V between 0 V and 1 V. The leads to and from the transistor structure were isolated from the electrochemical reaction in the cell.

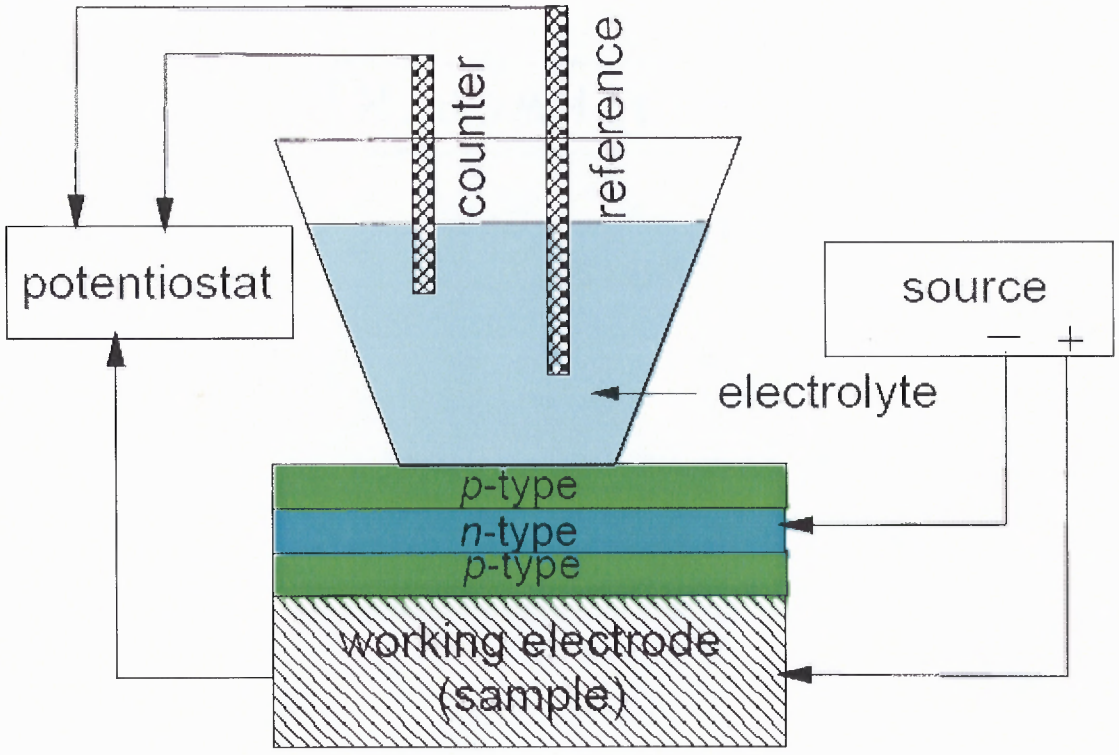

Figure 5.2 Schematic of the experimental setup for a transistor-like structures on a steel substrate. The bias was applied to the base of the transistor as shown.

5.3 Results

The current-voltage characteristics of a *n-p-n* transistor is shown in Figure 5.3. With an increase in the base voltage, the current between the collector and emitter has increased.

The Tafel plots for metal-*p-n-p* and metal-*n-p-n* samples are shown in Figure 5.4. With an increase in the base voltage, the metal-*p-n-p* corrosion potential shifted positively. The metal-*n-p-n* corrosion potential shifted negatively upon applying a positive base voltage.. These shifts were repeatable and reversible.

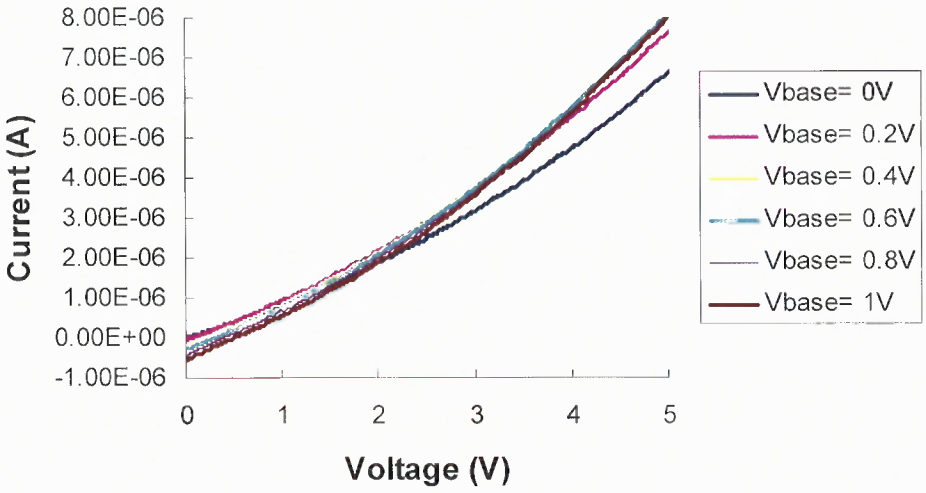

Figure 5.3 Current-Voltage characteristics of n-p-n characteristics at different base voltages. The current increases with increasing base voltage. No saturation has been observed, though.

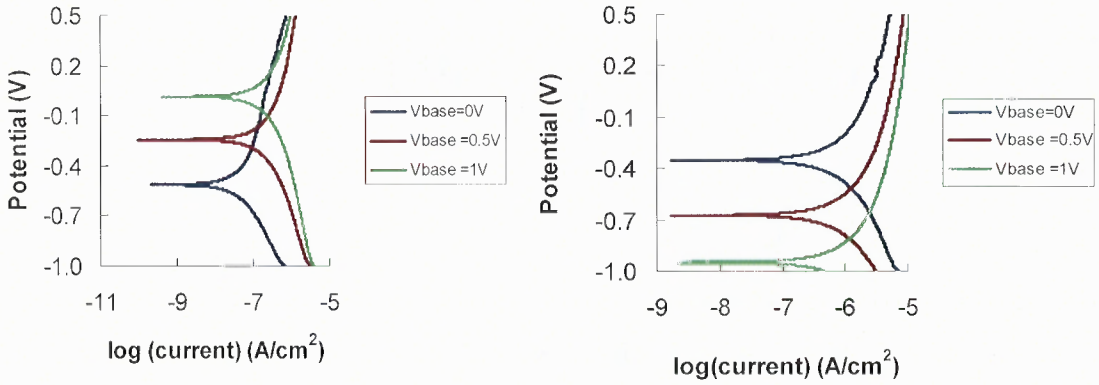

(a) **(b)**

Figure 5.4 Tafel plots of (a) steel-*p-n-p* (steel-CNT/Polyurethane-CNT/PEI/PMMA-CNT/Polyurethane) and (b) steel-*n-p-n* (steel-CNT/PEI/PMMA-CNT/Polyurethane-CNT/PEI/PMMA) in DI water. The corrosion potential of steel-*p-n-p* shifts positively for increasing base voltage. The corrosion potential of steel-*n-p-n* shifts negatively with an increase in the base voltage.

Optical microscope pictures and SEM/ EDX results are shown in Figures 5.5-5.6. Optical microscope images of steel-*p-n-p* indicate lesser corrosion than steel-*n-p-n* samples.

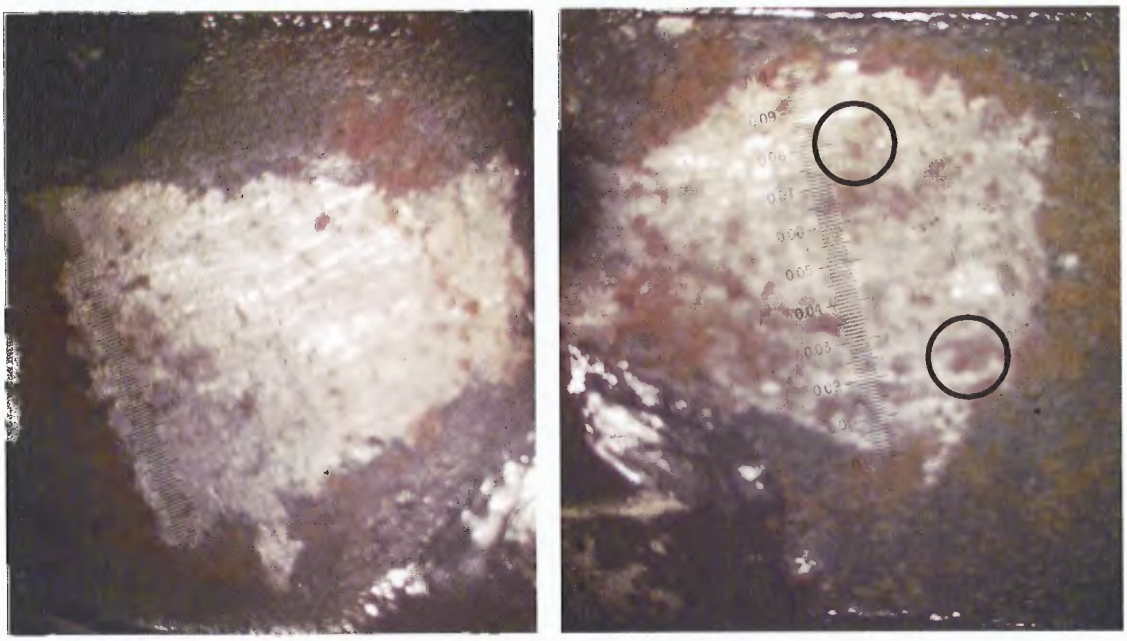

(a) **(b)**

Figure 5.5 Optical microscope pictures of (a) steel-*p-n-p* (steel-CNT/polyurethane-CNT/PEI/PMMA- CNT/polyurethane) and (b) steel-*n-p-n* (steel-CNT/PEI/PMMA-CNT/polyurethane- CNT/PEI/PMMA) in DI water. Heavier corrosion spots on steel-*n-p-n* are marked by circles. (Scale 0.01 division =1 mm).

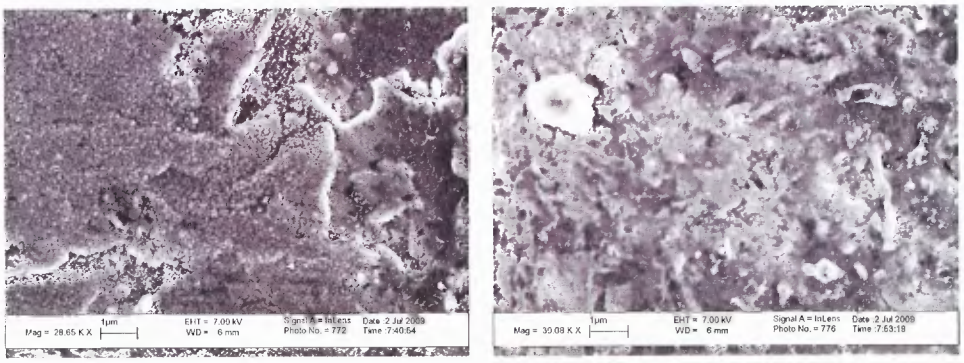

Steel-*p-n-p*		
Element	Weight%	Atomic%
C	2.73	7.20
O	26.54	52.62
Fe	70.74	40.18
Total	100.00	

(a)

Steel-*n-p-n*		
Element	Weight%	Atomic%
C	4.91	12.54
O	25.79	49.41
Fe	69.30	38.05
Total	100.00	

(b)

Figure 5.6 SEM and EDX results of (a) steel-*p-n-p* (steel- CNT/polyurethane – CNT/PEI/PMMA- CNT/polyurethane) and steel-*n-p-n* (steel- CNT/PEI/PMMA – CNT/polyurethane- CNT/PEI/PMMA) in DI water.

5.4 Discussion

A corrosion protection coating, forming a bipolar junction transistor-like structure between the electrolyte and metal has been considered. The control of the corrosion potential by the base potential has been demonstrated. The larger content of oxide in the transistor-like film in comparison with the diode-like structure is puzzling (Figure 5.6): it may indicate a larger passivation by the base voltage. That means that in effect, the base voltage affected the local Fermi-level of the *p-n* junction, situated between the base and metal. The difference between the *p-n-p* and the *n-p-n* structures alludes to the existence of junctions thus corroborating the effect of space-charge layers.

The transistor-like structure did not exhibit full current-voltage characteristics of a BJT. While the collector-emitter current did increase as a function of the base voltage, as expected, the transistor-like film did not reach the saturation current which is typically observed for a common-emitter configuration. This may be due to the large resistance of the various CNT-based layers.

The Tafel plot for steel-*p-n-p* at base voltage, Vb=0 V indicates a more negative voltage for the corrosion potential (-513 mV) compared to steel-*n-p-n* case (-352 mV). This is opposite to the effect that the diode-like structure had, where the steel-*p-n* structure had a more positive corrosion potential than the steel-*n-p* sample (Section 4.3). This indicates that the surface potential is not determined by the immediate layer next to the metal but the entire structure, only a few microns thick, affects the corrosion potential.

Summarizing, it is shown that the surface potential of a metal coated with transistor-like semiconducting carbon nanotube structures may be controlled by an

external base voltage. This might help us in choosing a surface potential for the steel substrate under different environments.

CHAPTER 6

GRAPHENE COATINGS ON STEEL SUBSTRATE

6.1 Introduction

Previously, electronic *p-n* junctions were considered as protectors of steel from corroding. Here graphene is added between the electronic barrier and the metal surface in an effort to study the effect of graphene on the corrosion process. Previous results are compared to metal-graphene-electronic structures. While graphene occupies only a few monolayers of carbon it has a noticeable effect on the surface potential of the metal.

Graphene is a monolayer of graphite sheet having hexagonal lattice symmetry with carbon atoms at the corner of each hexagon. Graphene has many remarkable properties such as mechanical robustness, large thermal conductivity and remarkable electronic properties. It is also known to be chemically inert [53]. It has been shown that graphene can be deposited on any surface by a process similar to lapping as described in the experiment section [54].

6.2 Experiment

AISI 4340 steel substrates were polished and cleaned as described in Section 4.2.2. Highly oriented pyrolitic graphite (HOPG) from SPI supplies was chemical-mechanically polished onto the steel substrate. It was then annealed in an inert Argon gas environment at 500^0 C. The annealed samples were subjected to an acetone sonicator bath to remove multiple layers of graphene formed. The sample was washed in DI and dried.

Three different sample surfaces were studied. The first surface tested comprised of only graphene on steel. In the second case, CNT *p-n* junctions were deposited on graphenated steel using drop casting to obtain steel-graphene-*p-n* and steel-graphene-*n-p* structures. In the third case, polypyrrole was deposited by either drop casting or, spinning at 1000 rpm to obtain steel-polypyrrole and steel-graphene-polypyrrole structures. The substrates served as the working electrode and were subjected to electrochemical tests as described in Section 4.2.3. The schematic of the experimental setup is shown in Figure 6.1

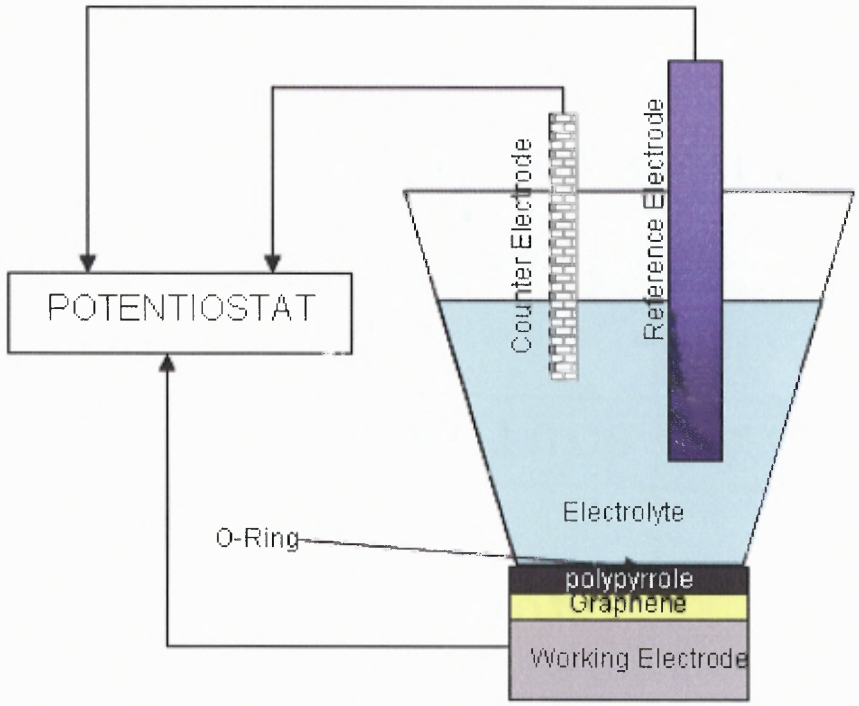

Figure 6.1 Schematic of electrochemical cell. Polarization characterizations were performed using a computerized potentiostat.

6.3 Results

Raman data of graphene is shown in Figure 6.2. The graphene exhibited two main peaks: 1594 cm^{-1} and 2667 cm^{-1}. The latter is indicative of a single layer graphene. The peak at 1310 cm^{-1} is indicative of the large number of domains in the sample.

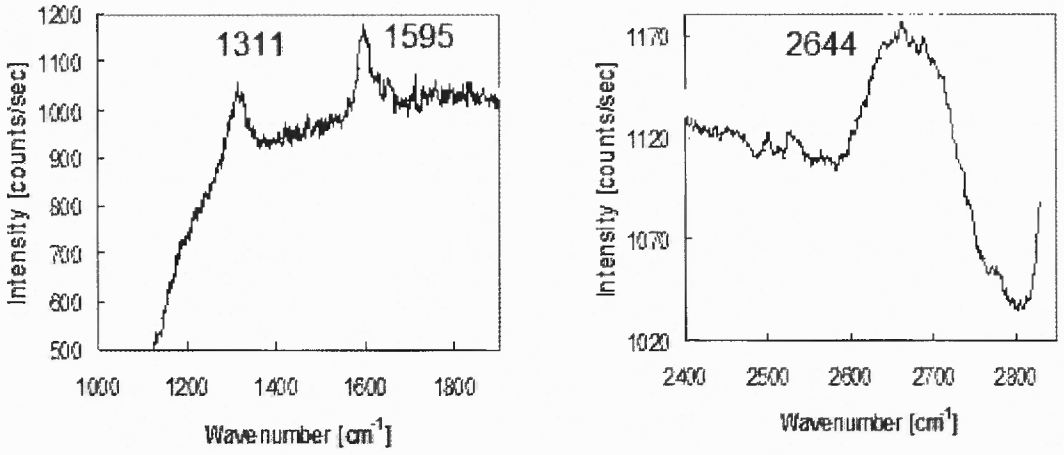

(a) **(b)**

Figure 6.2 Raman data of graphene on steel substrates. (a) The ~1600 cm^{-1} and (b) the ~2700 cm^{-1} lines. The ~1300 cm^{-1} line is indicative of domains. The ~2700 cm^{-1} line is indicative of the number of graphene layers: here a monolayer graphene is demonstrated.

Tafel plots for graphene on steel and graphene as an intermediate layer between metal/CNT junctions are shown in Figure 6.3. The corrosion potential has shifted positive in the case of steel-graphene-*n*-*p* (by +450 mV) compared with steel-*n*-*p*. On the other hand the corrosion potential shifted negative in the case of steel-graphene-*p*-*n* junction (by −100 mV) compared with steel-*p*-*n*. Also to be noted is that graphene shifted the corrosion potential of bare steel (-440 mV) positive by +300 mV.

Figure 6.4 shows Tafel plots for steel-polypyrrole and steel-graphene-polypyrrole structures. The intermediate graphene layer has shifted the metal-polypyrrole surface potential positively (by +50 mV).

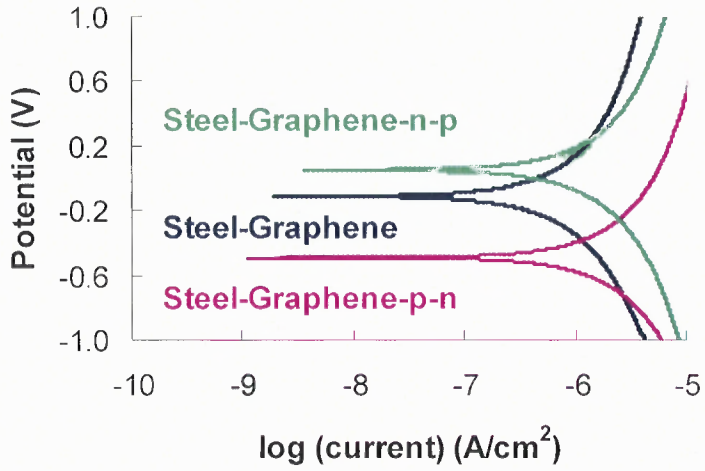

Figure 6.3 Tafel plots of steel-graphene, steel-graphene-*p*-*n* CNT junction and steel-graphene-*n*-*p* CNT junction structures. Presence of graphene has shifted the surface potential of bare steel and steel-*n*-*p* positive and steel-*p*-*n* negative.

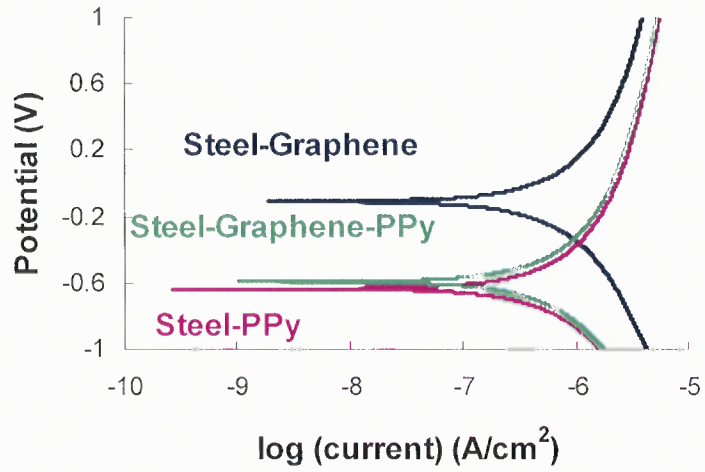

Figure 6.4 Tafel plots of steel-graphene, steel-polypyrrole and steel-graphene-polypyrrole structures. Presence of graphene shifted the surface potential of steel-polypyrrole positive.

Visual inspection by optical microscope (1X magnification) of steel and steel-graphene clearly shows larger corrosion on bare steel compared to graphenated steel (Figure 6.5).

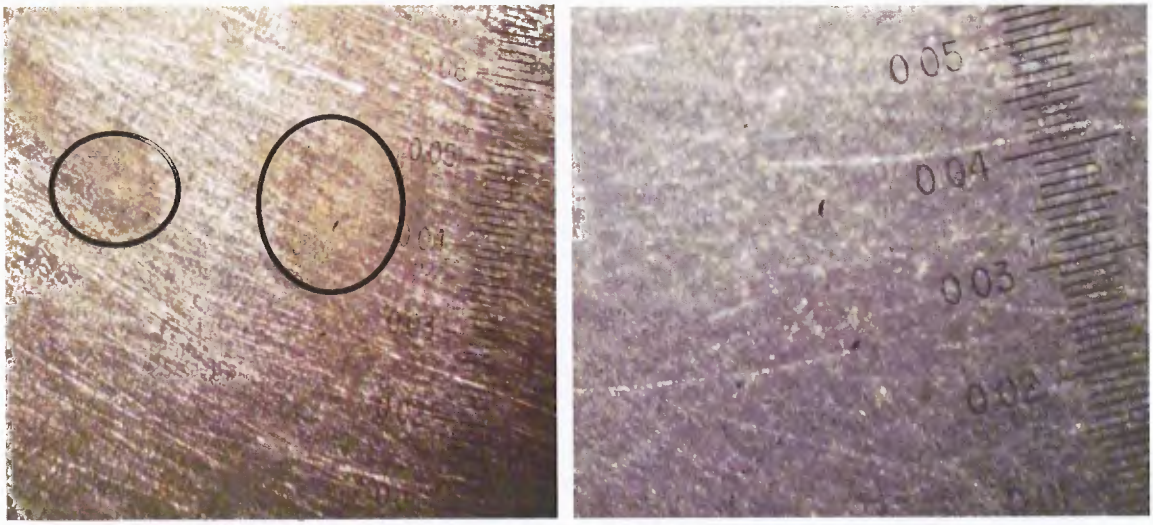

(a) (b)

Figure 6.5 Optical Microscope pictures of (a) bare steel and (b) steel-graphene: electrolyte was DI water. Corrosion spots are marked by circles. (Scale 0.01 division =1 mm).

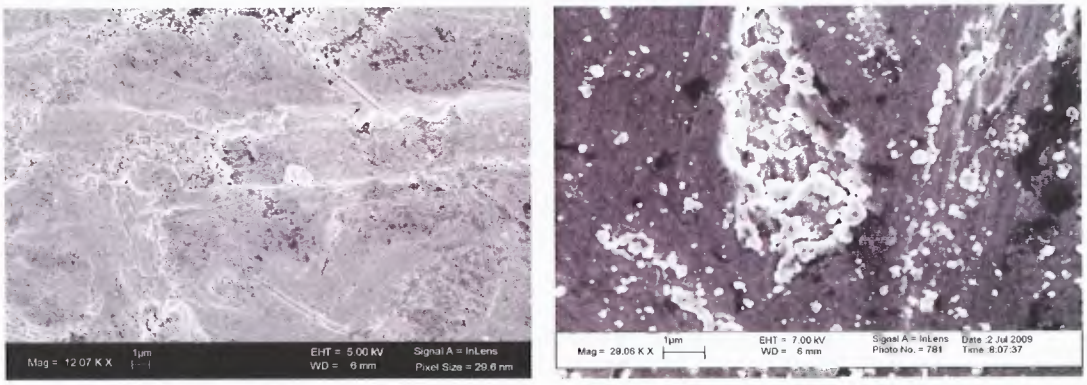

Bare Steel		
Element	Weight%	Atomic%
C	10.15	24.80
O	21.36	39.20
Fe	68.49	36.00
Total	100.00	

(a)

Steel-graphene		
Element	Weight%	Atomic%
C	11.28	30.75
O	11.80	24.15
Fe	76.92	45.10
Total	100.00	

(b)

Figure 6.6 SEM and EDX results of (a) bare steel and (b) steel-graphene: electrolyte was DI water. Bare steel EDX indicates a larger percentage of oxygen.

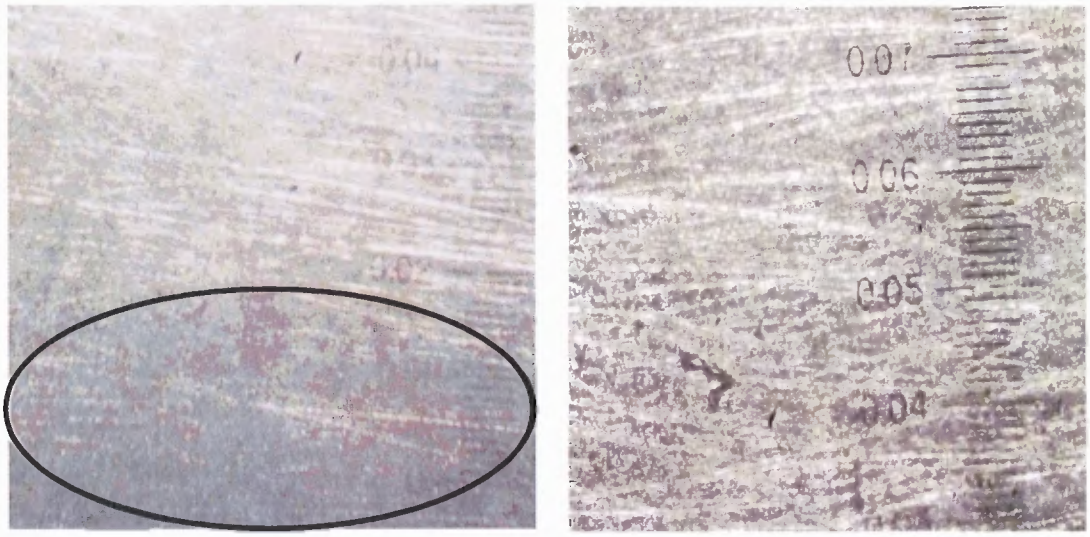

(a) **(b)**

Figure 6.7 Optical Microscope pictures of (a) steel-graphene-p-n (steel-graphene-CNT/polyurethane-CNT/PEI/PMMA) and (b) steel-graphene-n-p (steel-graphene-CNT/PEI/PMMA-CNT/polyurethane): electrolyte was DI water. Heavier corrosion spots on steel-graphene-p-n indicated by the arrow.

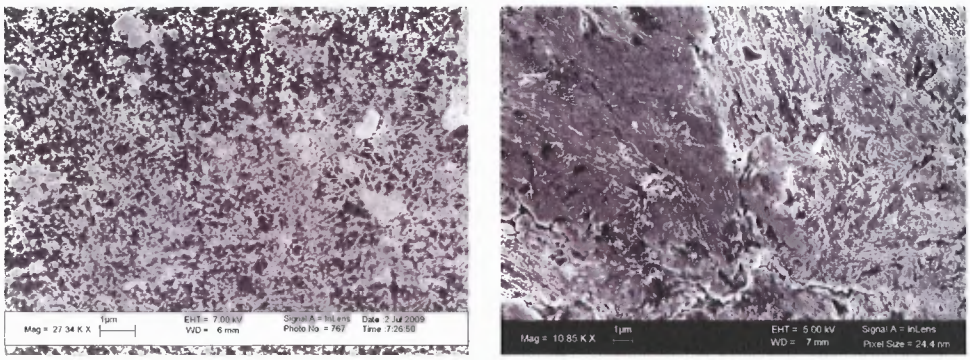

Steel-graphene-p-n		
Element	Weight%	Atomic%
C	3.36	11.95
O	7.47	19.93
Fe	89.16	68.12
Total	100.00	

(b)

Steel-graphene-n-p		
Element	Weight%	Atomic%
C	8.64	22.10
O	20.18	38.75
Fe	71.18	39.15
Total	100.00	

(b)

Figure 6.8 SEM and EDX results of (a) steel-graphene-p-n (steel-graphene-CNT/polyurethane-CNT/PEI/PMMA) and (b) steel-graphene-n-p (steel-graphene-CNT/PEI/PMMA-CNT/polyurethane): electrolyte was DI water.

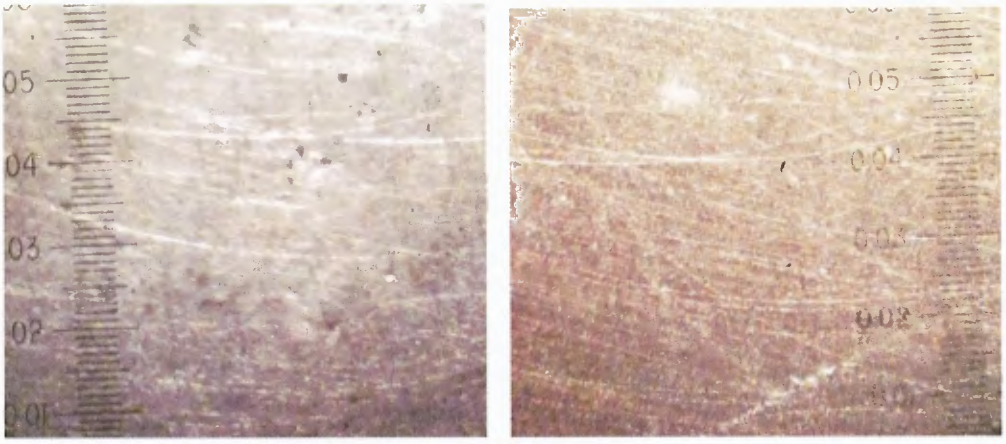

(a) **(b)**

Figure 6.9 Optical Microscope pictures of (a) steel-polypyrrole and (b) steel-graphene-polypyrrole: electrolyte was DI water. Heavier uniform corrosion on steel-graphene-polypyrrole is indicated by the orange coloration.

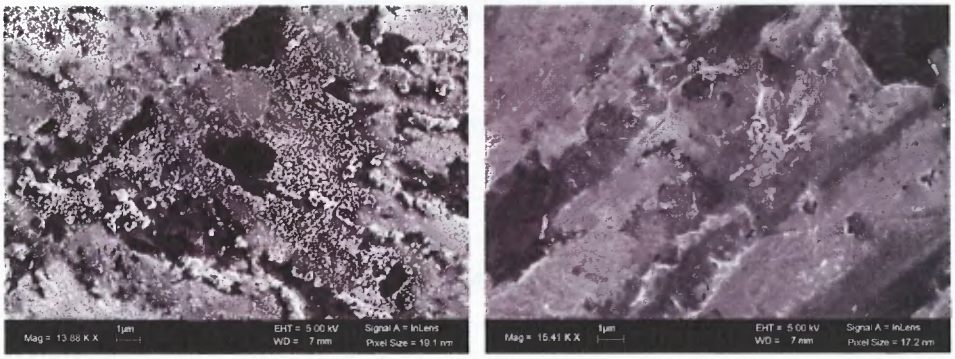

Steel-polypyrrole		
Element	Weight%	Atomic%
C	3.65	13.77
O	4.02	11.36
Fe	92.33	74.87
Total	100.00	

(a)

Steel-graphene-polypyrrole		
Element	Weight%	Atomic%
C	2.62	7.05
O	25.32	51.21
Fe	72.06	41.74
Total	100.00	

(b)

Figure 6.10 SEM and EDX results of (a) steel-polypyrrole and (b) steel-graphene-polypyrrole: electrolyte was DI water. Higher oxygen percentage in steel-graphene-polypyrrole.

The EDX results indicate lesser oxygen content for graphenated steel compared to bare steel. Optical microscope pictures of metal-graphene-*n*-*p* junction shows lesser degree of corrosion compared to metal-graphene-*p*-*n*. In effect, presence of graphene

reversed the effect of only *p-n* junctions on steel mentioned in section 4.3. Figures 6.7 - 6.8 show optical microscope images and SEM/EDX results for metal-graphene-CNT junctions. Optical microscope images for steel-graphene-polypyrrole shows heavier corrosion compared to steel-polypyrrole, shown in Figure 6.9. The corresponding SEM/EDX results indicate a higher oxygen percentage in steel-graphene-polypyrrole compared to steel-polypyrrole (Figure 6.10).

6.4 Discussion

Table 6.1 Corrosion Current and Corrosion Rate Comparison with Graphene as an Intermediate Layer

	Corrosion current Icorr (in nA/cm^2)	**Corrosion rate CR (in µm/y)**
Bare Steel	57.66	0.67
Steel-graphene	25 (121.83)	0.3 (1.4)
Steel-graphene-p-n	51 (277.64)	0.6 (3.21)
Steel-graphene-n-p	33 (180.15)	0.4 (2.1)
Steel-polypyrrole	90.12	1.04
Steel-graphene-polypyrrole	-13 (84.03)	-0.2 (0.97)

Note: The uncorrected values are indicated in the parentheses.

The effect of graphene – monolayer thick graphite – is quite profound on the surface potential and on the corrosion rate (Table 6.1). Equations 4.1, 4.2 and 4.3 were used in the calculation. The corrosion currents and corrosion rates obtained without any correction is indicated in parentheses of Table 6.1. The correction to the Tafel slopes were made as indicated in Section 4.4. Since, polypyrrole is an active coating, such

corrections are not relevant. The corrected values indicate that graphene coatings on bare steel reduced the corrosion rate. The corrosion rate of steel-graphene-*n*-*p* is smaller than steel-graphene-p-n which is corroborated by optical microscope pictures. The surface potential of steel-graphene was shifted positively compared to bare steel (Figure 6.3). From Figure 6.5 it appears that a monolayer of graphene on steel protects it from corroding. In that respect, the grapheme acted as a 'normal' barrier between the electrolyte and the metal. Such behavior is also corroborated by the corrosion rates provided in Table 6.1. This is not the case when graphene becomes an intermediate layer between the steel substrate and the CNT junction. The presence of graphene reversed the behavior of CNT *p*-*n* junctions noted in Section 4.4: Corrosion of steel-graphene-*p*-*n* was larger than for steel-graphene-*n*-*p*. Here again, the corrosion rates of Table 6.1 are corroborating the optical pictures. Tafel plots (Figure 6.3) show that the corrosion potential for steel-graphene-*n*-*p* was shifted positively by +450 mV compared to steel-*n*-*p*, indicating better corrosion barrier. Moreover, the corrosion potential for steel-graphene-*p*-*n* has shifted negatively indicating a worsening corrosion protection, as indeed is the case. To a limited degree, these results may be explained by the positively doped graphene which nullifies the negative carriers in both the metal and the *n*-type CNT. By comparison, the graphene is pin-hole free and its effect is more profound than the permeable, highly dispersive CNT film on the surface potential of the steel.

The corrosion potential for steel-polypyrrole (Figure 6.4) has shifted positively by +50 mV in the presence of graphene. Heavier corrosion rate was also noted for steel-graphene-polypyrrole compared to steel-polypyrrole (Figure 6.7). The corrosion currents provided in Table 6.1 should imply better protection by the graphene polypyrrole layers.

Yet, the case here is a bit different from the case for graphene-CNT since the polypyrrole protects metals through self-oxidation whereas the CNT are not electrochemically reactive. One may postulate that the addition of graphene changed the oxidation potential of the polypyrrole, leading to a larger degree of corrosion for the metal.

Such enhanced activity of graphene maybe explained by the formation of a double layer (polarization effect) across it. For example, the pore resistance and the double-layer resistance (see Chapter 8) are smaller for steel-graphene than for bare steel, meaning that the diffusion of iron away from the metal surface is larger. The double-layer capacitance has increased substantially when graphene was coating the steel substrate, almost by a factor of two. This was true either with the CNT *p-n* junction, or, with the polypyrrole coatings. For the CNT it resulted in a reversal of the junction role. In the case of polypyrrole it decreased the effectiveness of the protective film.

In summary, while graphene occupies only a few monolayers of carbon on the steel substrate it has a noticeable effect on the surface potential and the corrosion of steel.

CHAPTER 7

BIO-ELECTRONIC STRUCTURES AS PERMEABLE COATINGS

7.1 Introduction

In this part of the study, electronic and bio-electronic concepts in the control of ionic currents to and from a surface are employed. Deoxyribonucleic Acid (DNA) is a naturally occurring polymer found in genome coding. It is made of strongly bound double helix. Π-stacking interaction between bases and CNTs, which has prompted many studies on electronic applications of DNA. Single stranded DNA can be used to build a large molecular library, which can then be used to fabricate artificial and bio-inspired structures. Biophysical properties of such a polymer could be in principle ascertained by monitoring its role in the diffusion of ionic species.

CNTs have many potential applications due to their remarkable mechanical and electronic properties. However obtaining a well separated and dispersed SWCNTs is a challenge. Single stranded DNA (ssDNA) assisted dispersion and separation of CNTs in a solution have been studied in detail and analyzed by others [55]. This enabled a wide range of applications which combines the properties of ssDNA and CNTs.

7.2 Experiment

The AISI steel pieces were polished and cleaned as described in Section 4.2.1. The *n*-type suspension with DNA was obtained as described in Section 3.1. The *p*-type suspension used was CNTs functionalized with polyurethane. The different layers were drop casted

on a substrate to obtain steel-*p*-*n* and steel-*n*-*p* structures. The schematic of the experimental setup is as shown in Figure 4.2.

7.3 Results

The thermo electric test (Table 4.1) showed that the DNA wrapped CNT indeed exhibits an *n*-type semiconductor property. Optical microscope pictures show that the metal-*p*-*n*(CNT/polyurethane- CNT/DNA) provides better corrosion protection compared to metal-*n*-*p*(CNT/DNA- CNT/polyurethane) (Figure 7.1). Also, the DNA wrapped CNT as *n*-type CNT performed much better than the PEI wrapped *n*-type CNT as seen in Figure 7.2. The corresponding Tafel plot shown in Figure 7.3 indicates a lesser current for bio-electronic junction compared to the regular polymer wrapped junction.

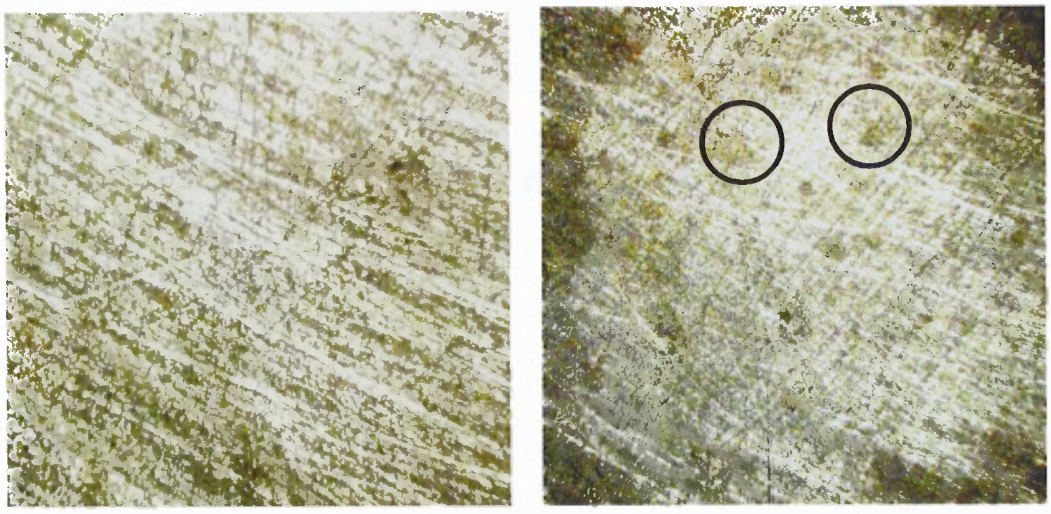

(a) **(b)**

Figure 7.1 Optical microscope pictures of (a)steel-*p*-*n* (CNT/polyurethane-CNT/DNA) and (b)steel-*n*-*p* (CNT/DNA- CNT/polyurethane) tested in DI water. Steel-*n*-*p* has heavier corrosion spots are marked by circles.

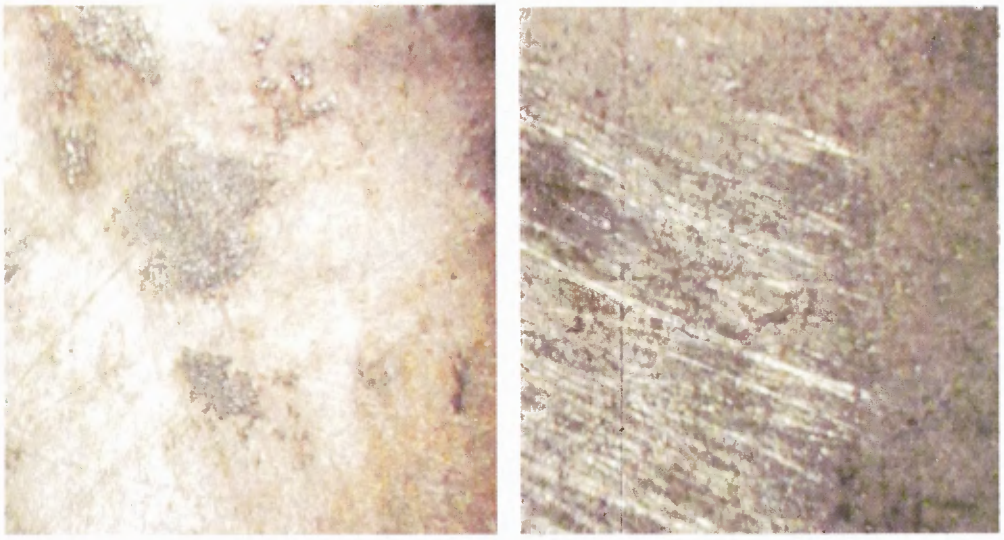

(a) **(b)**

Figure 7.2 Optical microscope pictures of (a) steel-*n*-*p* (CNT/PEI-CNT/polyurethane) and (b)steel-*n*-*p* (CNT/DNA- CNT/polyurethane) tested in DI water. Heavier corrosion on the steel-*n*-*p* with *n*-type CNT functionalized with PEI.

7.4 Discussion

Table 7.1 Corrosion Current and Corrosion Rate Comparison of Bio-electronic Structures

	Corrosion current Icorr (in nA/cm^2)	**Corrosion rate CR (in µm/yr)**
Bare Steel	58	0.7
Steel-p (CNT/polyurethane)-n (CNT/DNA)	224	2.6
Steel- n(CNT/DNA)-p(CNT/polyurethane)	257	2.9

The corrosion current and corrosion rate calculations using Equations 4.1 and 4.2 are shown in Table 7.1. Peeling-off of layers on glass prevented us from correcting the data along the procedure indicated in Equation 4.3. One may observe that as before, the steel-*n*-*p* structure seems to portray a better corrosion protection than the steel-*p*-*n*

sample. Both were showing inferior protection compared to bare steel. As argued earlier, such behavior may be attributed to the non-Faradaic effects.

The *p-n* junction with *n*-type CNT obtained by wrapping DNA has similar effect as polymer wrapped *p-n* junctions discussed in Section 4.4. With ssDNA wrapping, a vast set of molecular library is possible, which can be used in bio-applications, such as precise placement of conjugated molecules [55]. This structure may be used to protect prosthetics as well

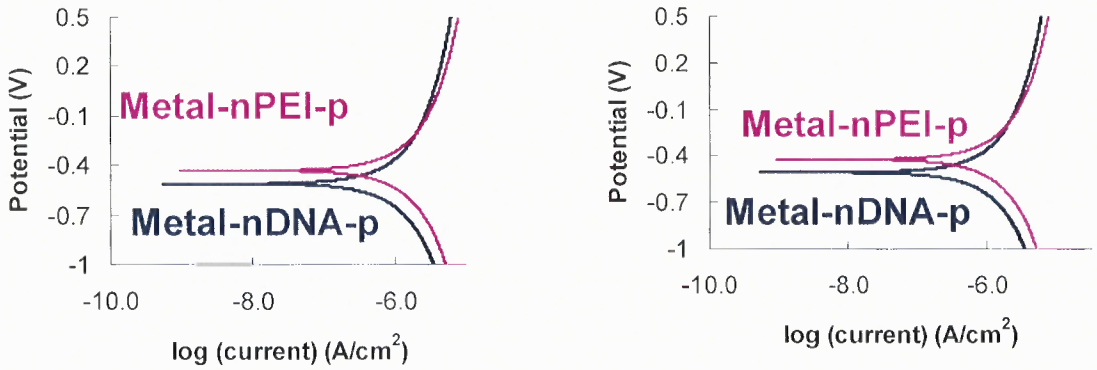

Figure 7.3 Tafel plot of (a) steel-*p-n* and (b) steel-*n-p* for both the regular *n*-type CNT wrapped with PEI and DNA wrapped *n*-type CNT. The bio-junctions exhibit lower corrosion current compared to the electronic junction.

.

CHAPTER 8

MODEL

8.1 Introduction

Graphical methods provide the first step towards analyzing and interpreting EIS data. Indicated in the flow chart of figure 2.3, the approach of equivalent circuit to analyze experimental EIS data is taken. A possible equivalent circuit can be estimated. The reactive systems can be represented by a Randles circuit shown in figure 8.1. The impedance and phase angle of the circuit is given by

$$Z(f) = Rs + \frac{Rp + Z_d(f)}{1 + j \cdot 2\pi \cdot f \cdot \left[Rp + Z_d(f) \right]} \qquad [8.1]$$

$$\Phi = \tan^{-1}\left(\frac{Z_j}{Z_r}\right) \qquad [8.2]$$

Where Rs is solution resistance, Rp is polarization resistance, Cdl is the double layer capacitance and Zd(f) is the diffusion impedance, specific to a system. However this expression is not accurate. For electrochemical systems exhibiting ohmic or electrolyte resistance, the use of phase angle plots are uncorrelated. If an accurate electrolyte resistance (Rs,est) is available then the modified bode plot calculation would be as shown in the equation below[49]. In the corrected bode plot, the current and voltage are in phase at low frequencies and out of phase (90 deg) at high frequencies.

$$\Phi = \tan^{-1}\left(\frac{Z_j}{Z_r - R_{s,est}}\right) \qquad [8.3]$$

$$|Z_{adj}| = \sqrt{(Z_r - R_{s,est})^2 + (Z_j)^2} \qquad [8.4]$$

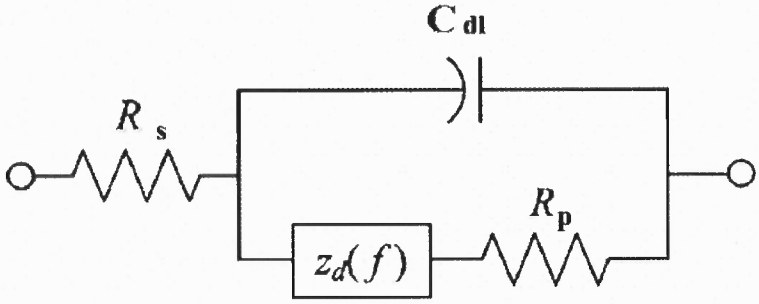

Figure 8.1 Randles circuit.

Randles circuit can be modified to obtain typical equivalent circuits for coated substrates either in DI or, NaCl solutions as electrolyte (Figure 8.2) where there are two time constants: One set of R-C for the coating and the other R-C for the electrolyte-working electrode interface as described in Section 2.2.

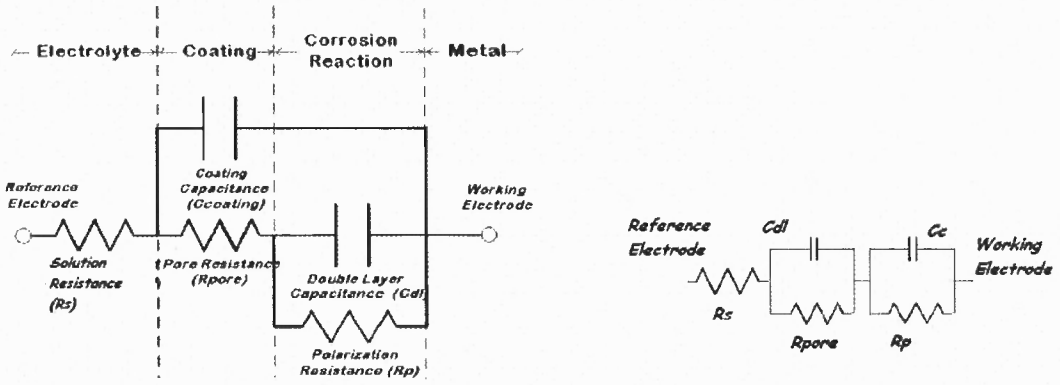

(a) **(b)**

Figure 8.2 Equivalent circuits of coatings in (a) DI and (b) NaCl solutions

8.2 EIS Calculations of Diode-Like Electronic Structure Coatings

The Bode plots for steel substrate coated with electronic p-n junction are indicated in Figure 8.3 for regular polymers. For enhanced polymer imbedded junctions, Bode plots are shown in Figure 8.4. The circuit elements calculations are tabulated in Table 8.1.

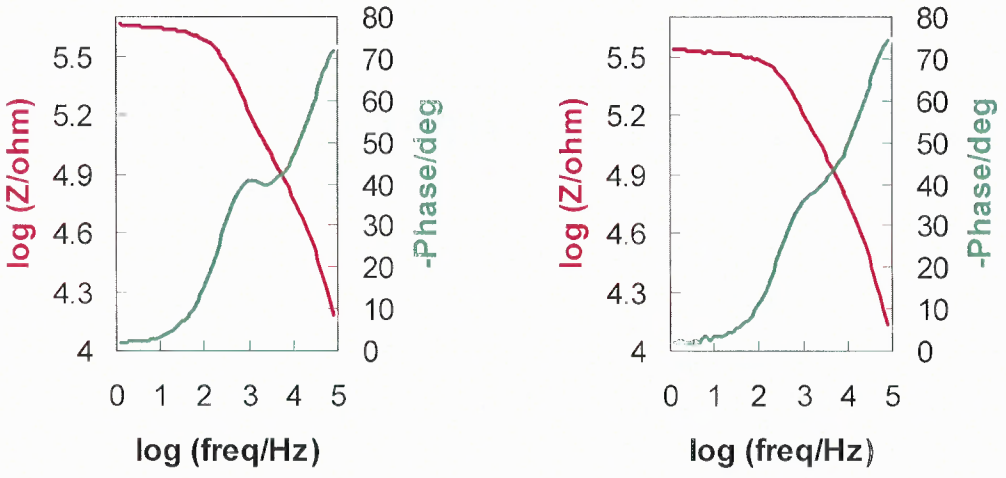

(a) (b)

Figure 8.3 Bode plot of (a) steel-polyurethane-PMMA and (b) steel-PMMA-polyurethane in DI water.

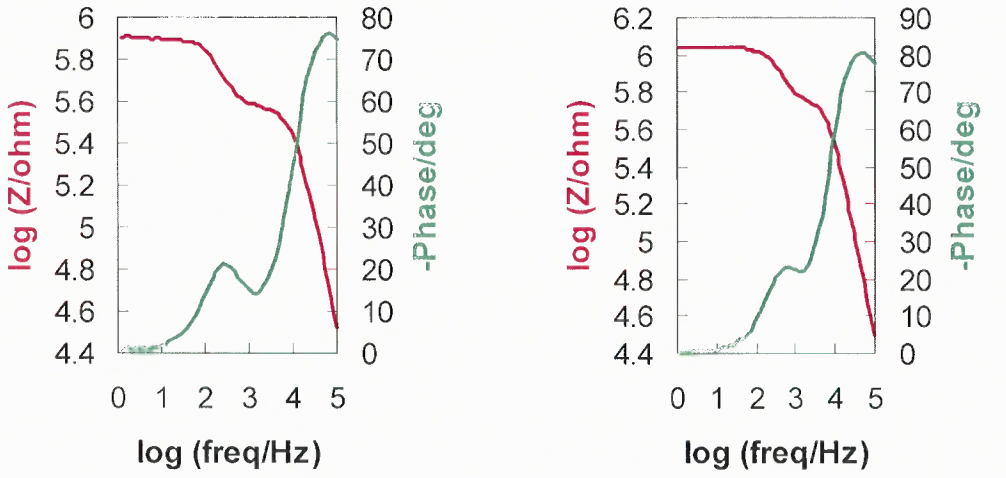

(a) (b)

Figure 8.4 Bode plot of (a) steel-p-n (steel-CNT/PVP-CNT/PEI) and (b) steel-n-p (steel-CNT/PEI-CNT/PVP) in DI water.

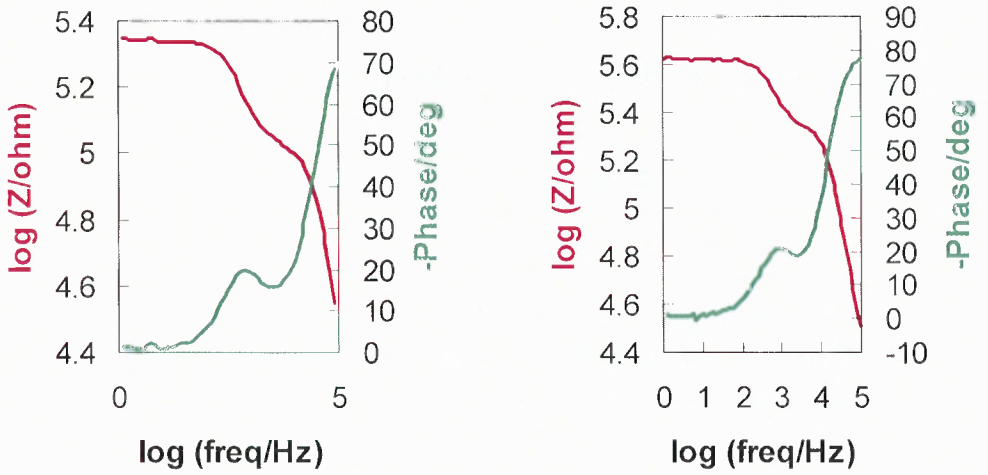

(a) (b)

Figure 8.5 Bode Plots for (a) steel-p-n (steel-CNT/polyurethane-CNT/PEI/PMMA) and (b) steel-n-p (steel-CNT/PEI/PMMA-CNT/polyurethane) in DI water.

Table 8.1 Calculated and Fitted Equivalent Circuit Elements for p-n Junctions in DI Water

	Solution resistance Rs (in kΩ)	Polarization resistance Rp (in kΩ)	Pore resistance Rpore (in kΩ)	Double layer capacitance Cdl (in nF)	Coating capacitance Ccoating (in pF)
Bare Steel	36.9	626	557.1	3.21	50
Steel-p (PVP/CNT)-n(PEI/CNT)	36.9	400	380	2.3	40
Steel-n(PEI/CNT)-p(PVP/CNT)	36.9	539	600	1	42
Steel-p(Polyurethane/CNT)-n(PMMA/PEI/CNT)	36.9	110	110	2.8	47
Steel-n(PMMA/PEI/CNT)-p(Polyurethane/CNT)	36.9	207	210	1.4	50

The fitted graphs for bare steel, steel-p-n(CNT/PVP-CNT/PEI), steel-n-p(CNT/PEI-CNT/PVP), steel-p-n(CNT/polyurethane-CNT/PEI/PMMA) and steel-n-p(CNT/PEI/PMMA-CNT/polyurethane) tested in DI water are shown in Figures 8.5-8.11. The sum of square of errors with respect to double layer capacitance Cdl and coating capacitance Cc was minimized for all the cases. A typical MathCAD program file for bare steel is shown in the appendix.

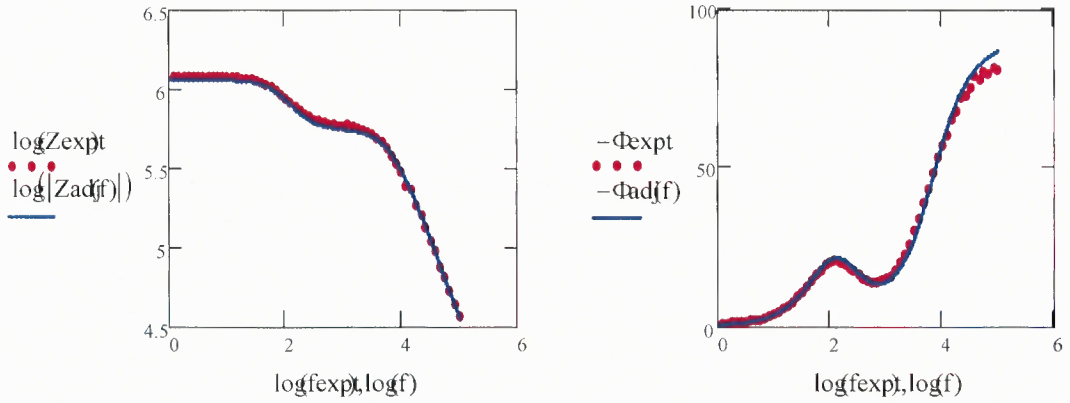

(a) (b)

Figure 8.6 Curve fitting for (a) impedance and (b) phase curves of the equivalent circuit parameters for the case of bare steel.

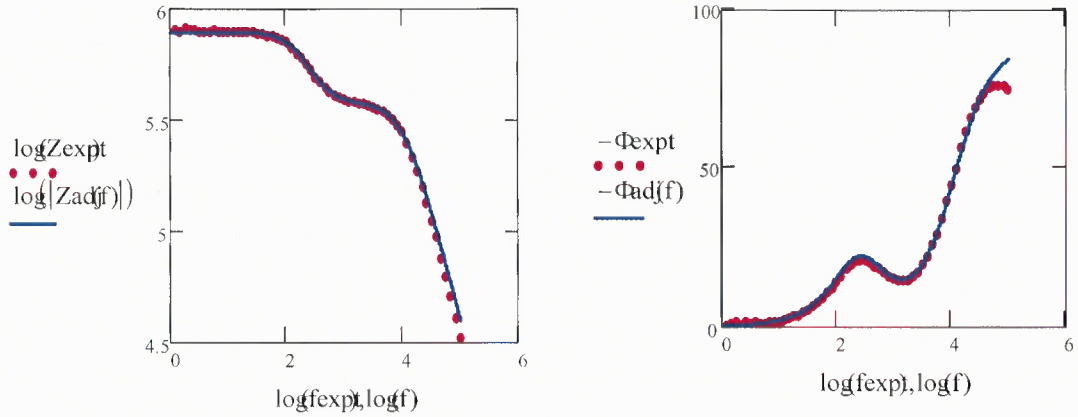

(a) (b)

Figure 8.7 Curve fitting for (a) impedance and (b) phase curves of the equivalent circuit parameters for the case of steel-p-n(CNT/PVP-CNT/PEI).

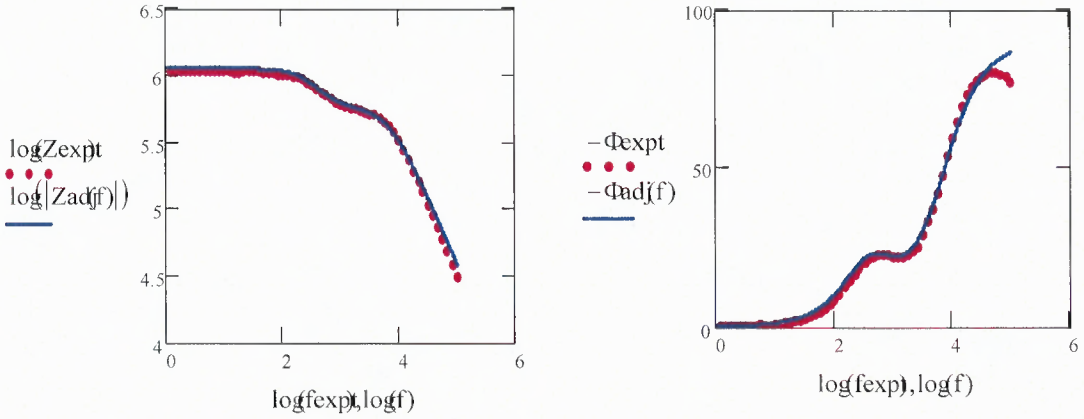

Figure 8.8 Curve fitting for (a) impedance and (b) phase curves of the equivalent circuit parameters for the case of steel-n-p(CNT/PEI-CNT/PVP).

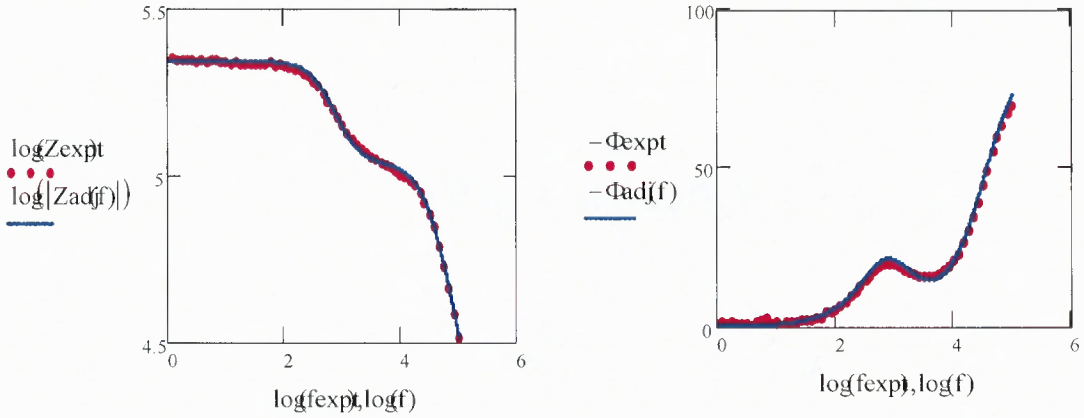

Figure 8.9 Curve fitting for (a) impedance and (b) phase curves of the equivalent circuit parameters for the case of steel-p-n(CNT/polyurethane -CNT/PEI/PMMA).

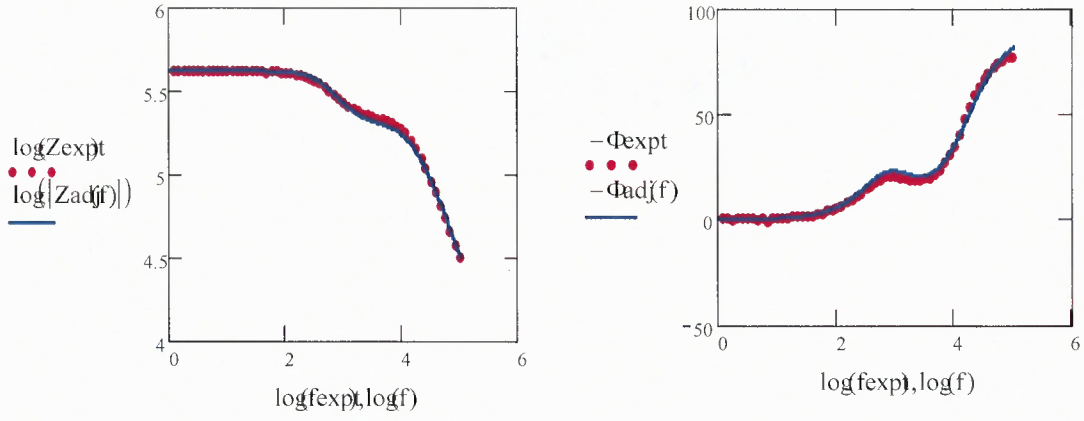

Figure 8.10 Curve fitting for (a) impedance and (b) phase curves of the equivalent circuit parameters for the case of steel-n-p(CNT/PEI/PMMA -CNT/polyurethane).

The situation for NaCl immersed films is used is more complex. Iin addition to the adhered hydrous ferric oxide, there exists ferric chloride, as well. The optical images indicate that the junction potential barrier is not sufficient to fully withstand corrosion. Modeling such multi-component kinetics is beyond the scope of this thesis.

8.3 EIS Calculations of Transistor-Like Electronic Structure Coatings

The bode plots for transistor like structures at different base voltages are in indicated in figures 8.10 and 8.11. The effect of base potential on the circuit at high frequencies is small.

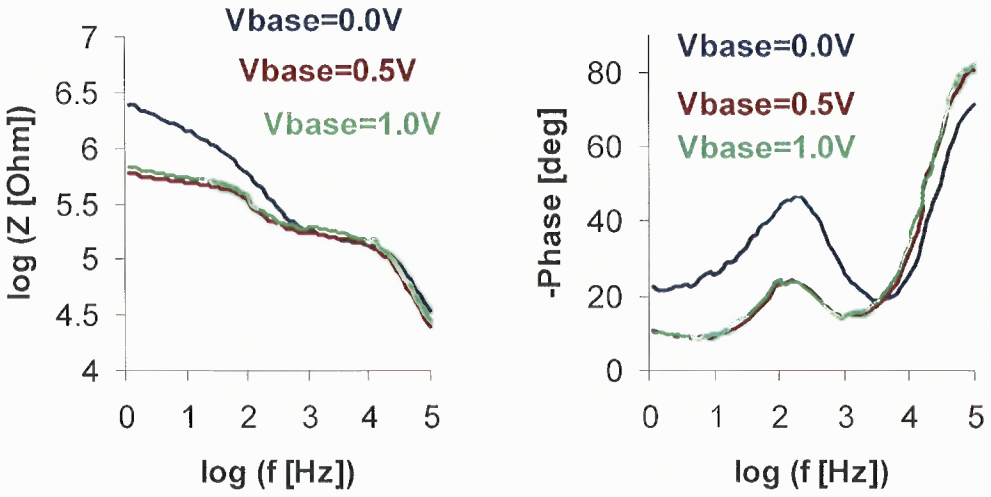

(a) **(b)**

Figure 8.11 (a) Impedance and (b) Phase Bode plots of steel-*p*-*n*-*p* transistor like structure at different base voltages.

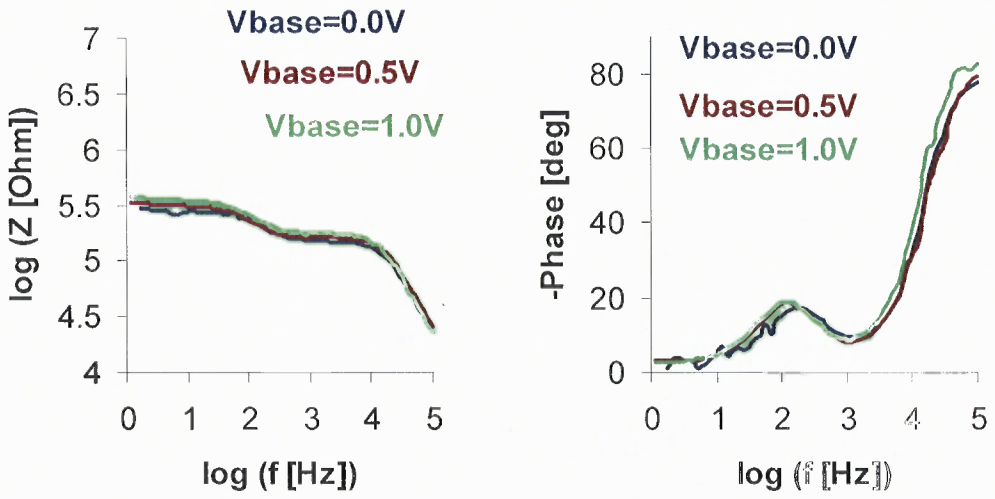

(a) **(b)**

Figure 8.12 (a) Impedance and (b) Phase Bode plots of steel-*n*-*p*-*n* transistor like structure at different base voltages.

8.4 EIS Calculations of Graphene Coatings

Bode plot for steel-graphene is indicated in figure 8.12. The equivalent circuit shown in Figure 8.2(a) was assumed. The corresponding circuit element values for steel-graphene, steel-graphene-*p*-*n* junction, steel-graphene-*n*-p junction, steel-polypyrrole and steel-graphene-polypyrrole are tabulated in Table 8.2 and the related fitted Bode plots are shown in Figures 8.13-8.17.

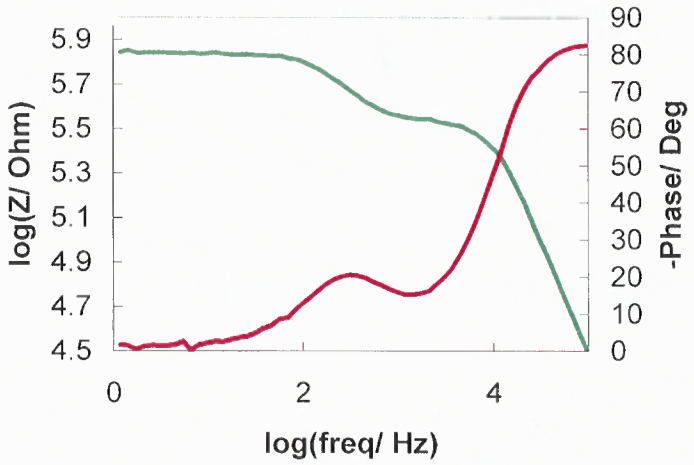

Figure 8.13 Bode plot of steel-graphene tested in DI water.

Table 8.2 Calculated and Fitted Equivalent Circuit Elements with Graphene as an Intermediate Layer

	Solution resistance Rs (in kΩ)	**Polarization resistance Rp (in kΩ)**	**Pore resistance Rpore (in kΩ)**	**Double layer capacitance Cdl (in nF)**	**Coating capacitance Ccoating (in pF)**
Steel-graphene	36.9	300	350	2.6	50
Steel-graphene-p(polyurethane/CNT)-n(PMMA/PEI/CNT)	36.9	130	170	5.3	58
Steel-graphene-n(PMMA/PEI/CNT)-p(polyurethane/CNT)	36.9	200	220	3.5	46
Steel-polypyrrole	36.9	400	420	1.7	46
Steel-graphene-polypyrrole	36.9	370	440	4.7	53

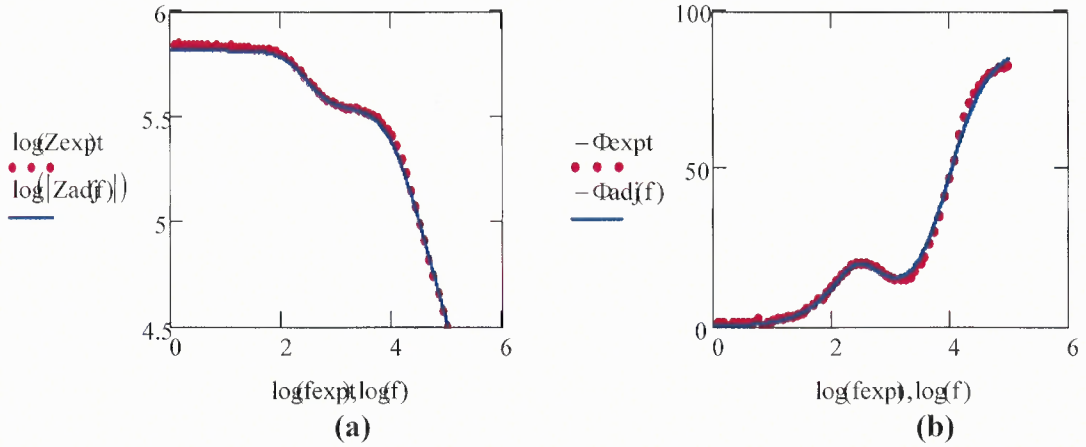

(a) (b)

Figure 8.14 Curve fitting for (a) impedance and (b) phase curves of the equivalent circuit parameters for the case of steel-graphene.

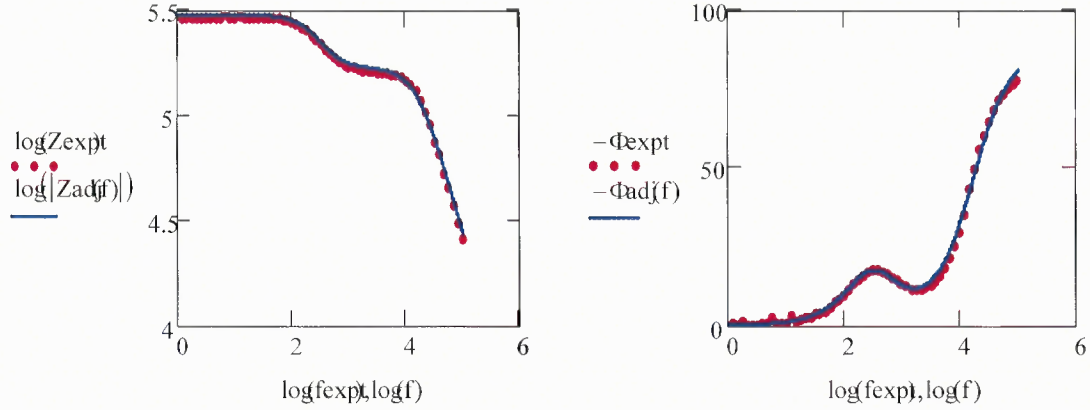

(a) (b)

Figure 8.15 Curve fitting for (a) impedance and (b) phase curves of the equivalent circuit parameters for the case of steel-graphene-p-n(CNT/polyurethane-CNT/PEI/PMMA).

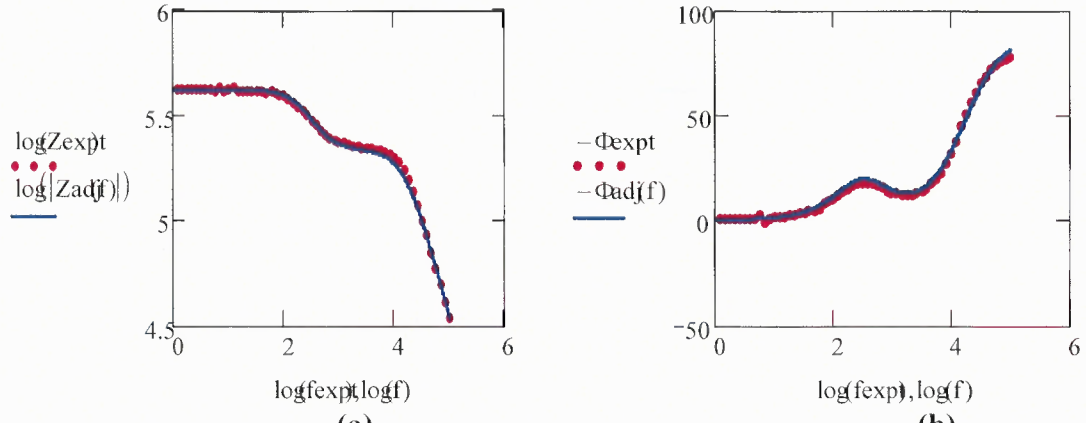

(a) (b)

Figure 8.15 Curve fitting for (a) impedance and (b) phase curves of the equivalent circuit parameters for the case of steel-graphene-n-p(CNT/PEI/PMMA - CNT/polyurethane).

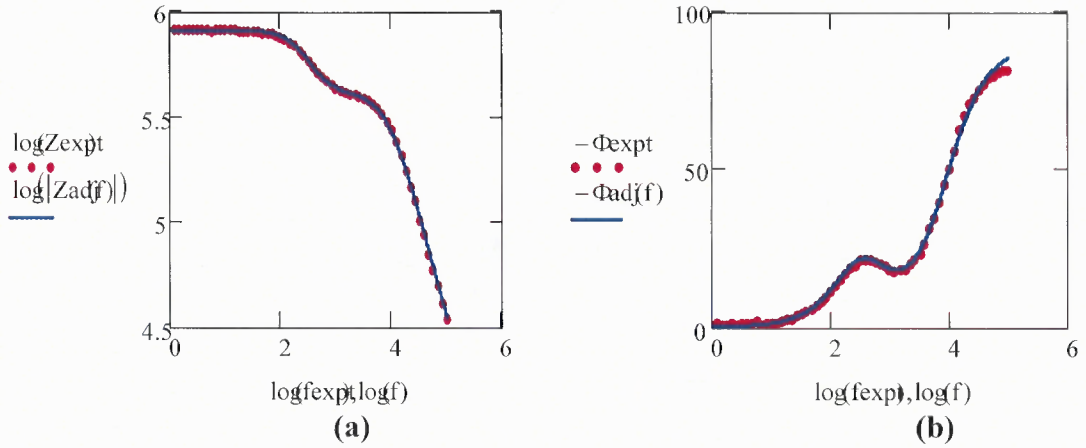

Figure 8.17 Curve fitting for (a) impedance and (b) phase curves of the equivalent circuit parameters for the case of steel-polypyrrole.

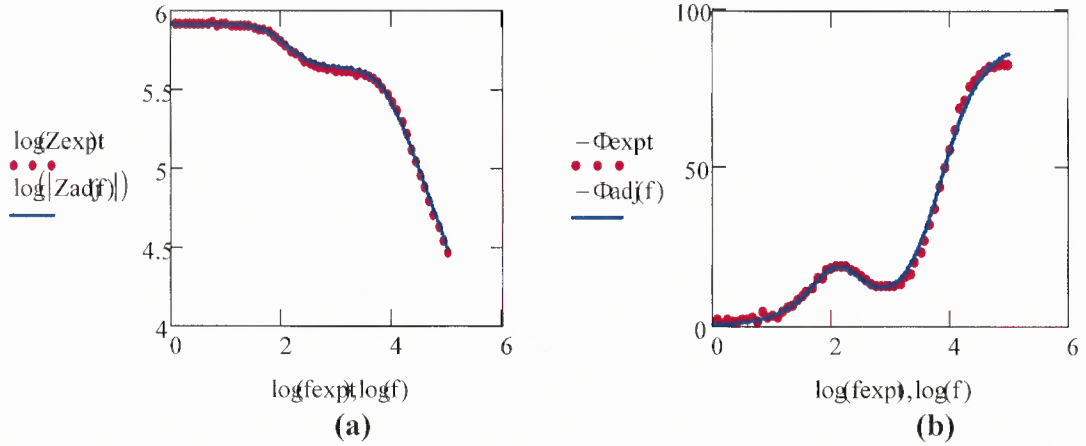

Figure 8.18 Curve fitting for (a) impedance and (b) phase curves of the equivalent circuit parameters for the case of steel-graphene-polypyrrole.

8.5 EIS Calculations of Bio-Electronic Structures

Bode plots for electronic junctions formed with DNA wrapped CNTs is shown in Figure 8.18. The equivalent circuit in Figure 8.2(a) was considered. Fitted values for the circuit elements are tabulated in Table 8.3. The fitted graphs are shown in Figures 8.19 and 8.20.

.

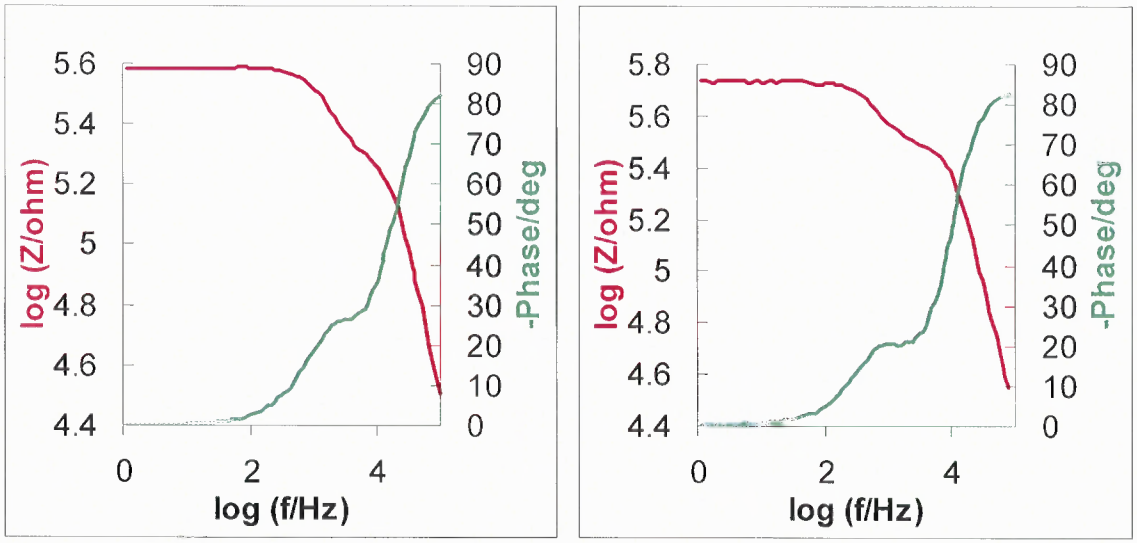

(a) **(b)**

Figure 8.19 Bode plots for (a) steel-p-n (CNT/polyurethane- CNT/DNA) and (b) steel-n-p (CNT/DNA- CNT/polyurethane).

Table 8.3 Calculated and Fitted Equivalent Circuit Elements with Graphene as an Intermediate Layer Calculated and Fitted Equivalent Circuit Elements for Bio-electronic Structures

	Solution resistance Rs (in kΩ)	**Polarization resistance Rp (in kΩ)**	**Pore resistance Rpore (in kΩ)**	**Double layer capacitance Cdl (in nF)**	**Coating capacitance Ccoating (in pF)**
Steel-p(CNT/polyurethane) – n(CNT/DNA)	36.9	161	220	0.8	49
Steel-n(CNT/DNA)-p(CNT/polyurethane)	36.9	210	330	1.5	53

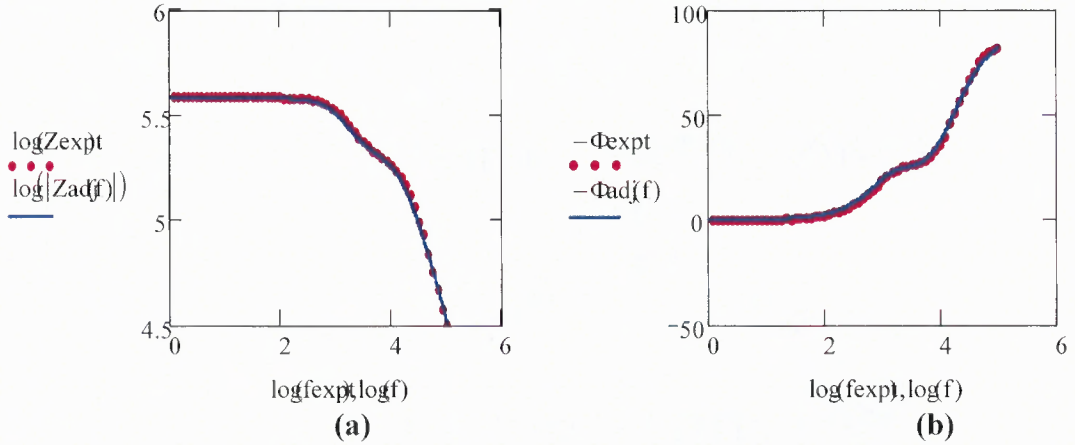

(a) (b)

Figure 8.20 Curve fitting for (a) impedance and (b) phase curves of the equivalent circuit parameters for the case of steel-p-n(CNT/polyurethane-CNT/DNA).

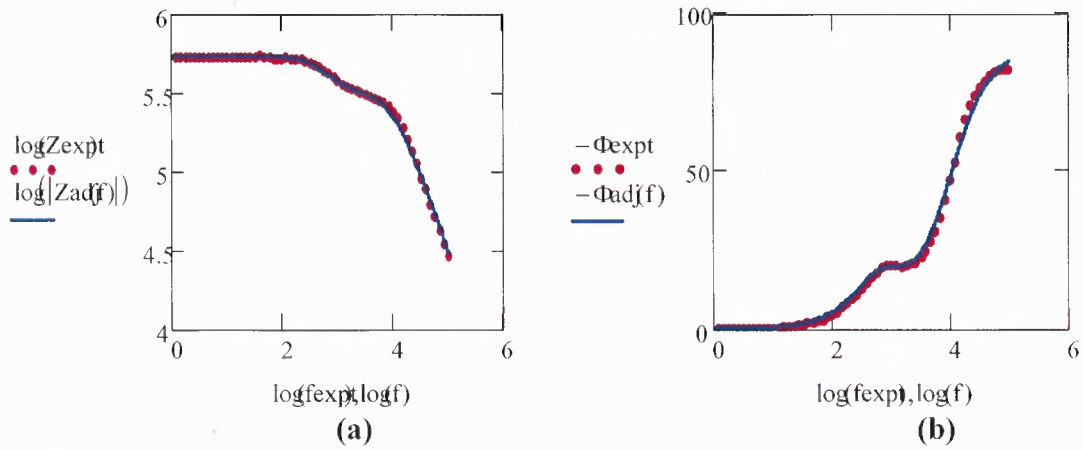

(a) (b)

Figure 8.21 Curve fitting for (a) impedance and (b) phase curves of the equivalent circuit parameters for the case of steel-n-p(CNT/DNA-CNT/polyurethane).

8.6 Discussion

The equivalent circuits used here provide with a fairly good fit to the experimental data. They also provided with an insight to the various corrosion processes. For example, the double layer capacitance of bare steel is larger than the corresponding value for steel-*p*-*n*. The double-layer capacitance of steel-*p*-*n* was larger than the related capacitance of steel-*n*-*p*, implying better protection. That may be explained by the existence of two double-layer capacitors in series in addition to the commonly used coating capacitor. This was

not true for the bio-electronic structure for which the steel-*n*-*p* exhibited a larger capacitance and lower corrosion protection than its steel-*p*-*n* counterpart. Graphene accentuated the role of the double-layer (DL) capacitor: the addition of monolayer thick graphene decreased the DL capacitance yet, increased its value when placed between the CNT junction and the metal.

CHAPTER 9

CONCLUSION

A new concept of anti-corrosion protection by introducing a potential barrier in the form of electronic structures made of semiconducting films has been introduced. In the first case study, diode-like *p-n* junctions were considered. They were formed by functionalized carbon nanotubes. Here it was demonstrated that the directionality of the potential barrier whether it is steel-*p-n* and steel-*n-p* did indeed matter for the flowing ions to and from the steel substrate. The setup was modeled and an equivalent circuit was proposed.

In the second case study, transistor-like structures were introduced. They were also formed by successive layers of functionalized CNTs. The idea here was to use the base voltage as a controlling parameter for the surface potential. It was indeed shown that the base potential controlled the surface potential and in effect, controlled the ionic species flow. At high frequencies, the DC base voltage did not impact the film response.

In the third case study, the effect of monolayer thick graphite (graphene). was explored. Not only did the graphene make a bare steel substrate more corrosion tolerant, it was also demonstrated that the semi-metal graphene altered the surface potential of the coated metal substantially. Finally, it was shown that when graphene was placed as an intermediate layer between steel and carbon nanotube based *p-n* junction, it reversed the effect of carbon nanotube *p-n* junctions on bare steel.

In the fourth case study, the electronic *p-n* junction was made bio-compatible. Here deoxyribose nucleic acid was used as a macro polymer to functionalize carbon nanotubes. This paved the way to build a large molecular library.

CHAPTER 10

FUTURE WORK

Carbon nanotube electronic junctions as anti-corrosion coatings in DI water as electrolyte has been demonstrated. Synthetic sea water or 3.5 wt% NaCl solution ionic concentration was too high for this junction. A larger potential barrier is required in order to counter large ionic concentration environments. A new material research has to be undertaken in order to achieve this goal.

A setup to perform in vitro studies of the corrosion process using spectro-electrochemistry needs to be developed. This would accurately help us determine the chemistry at the semiconductor/electrolyte interface.

The mechanical adherence of the CNT films to the metal substrate needs to be further improved: a more robust method ought to be developed. Other polymeric matrices such as epoxy could be used. In addition to the already established corrosion protection such as paints, the electronic structures could help in monitoring corrosion of the metal surface underneath it.

CHAPTER 11

APPLICATION

As an application, protection of ships is considered. Ship's hull is made of steel. When the ship hull has chipped paint, the hull corrodes excessively in sea water. A protection method called cathodic protection is used to prevent corrosion of steel. The principle here is that when two metals are coupled electrochemically, the more active metal corrodes protecting the more noble metal. Cathodic protection has been used since 1800s to protect ships from corroding. Steel is protected by sacrificing zinc or, cadmium. When properly installed and maintained, a ships protection lifespan is anywhere between 10 and 15 years. This method requires large quantities of sacrificial metal that significantly increases the weight of the hull. A side effect of improperly performed cathodic protection is the generation of hydrogen gas resulting in hydrogen embrittlement of metal joints.

Impressed current cathodic protection (ICCP) provides a current from an external power supply, thus, maintaining the potential of the sacrificial metal more negative. Fewer anodes are required because of the increased output capabilities, and a feedback control may be included to closely monitor the hull protection levels. This method is not fully effective at the water's edge and is limited to areas of 4 feet below the water surface. The design of anode placement is complicated for complex hull geometries [62, 63].

Epoxy, urethane and vinyl based coatings are commonly used along with cathodic protection. Epoxy films are easy to apply and offer good corrosion protection for steel in

water, soil and organic acids. Yet, various problems, such as low curing time and non-usability at low temperatures arise. Another major disadvantage is the inability of monitoring corrosion under the protecting film [64, 65].

In this study a smart coating was considered. The diode-like structures would be an ideal coating for corrosion prevention of metals, such as ship's hull. Carbon nanotubes are chemically stable and are less susceptible to oxidation. At the same time, the films provide protection to the metal substrate. The films are easy to apply. In addition, the CNT may be imbedded in known polymer matrices, such as polyurethane and poly (methyl methacrylate) to enhance mechanical adherence of the film to the substrate.

An underlying coat of a diode between the hull and epoxy coating may enable corrosion monitoring, along with added corrosion protection. The open circuit potential could be monitored for the coated steel. A decrease (or shift in the negative potential range) in the corrosion potential (or open circuit potential) indicates formation of rust. In addition, when non-destructive AC tests are performed, the double layer capacitance and pore resistance could be used to monitor the corrosion. In chapter 4 discussion section, it is shown that steel-*p*-*n* provides a better protection than steel-*n*-*p*. The double layer capacitance for steel-*n*-*p* was much smaller due to a larger reactivity. A similar analysis could be applied for steel-*p*-*n*. If the double layer capacitance decreases over time it may indicate that the metal is corroding. Also, the polarization resistance is expected to increase due to reduced polarizability of the metal substrate. Due to a water uptake, pore resistance of the coating is expected to decrease with an increase of corrosion. Hence, not only will the electronic *p*-*n* junction reduce the corrosion rate, it also provides means to monitor the corrosion. At any time, the open circuit potential and double layer

capacitance for the coating could be measured and the response could be used to assess the corrosion under the coating.

Drawbacks for such corrosion monitoring would be the complex design for large areas, such as a ship hull. The mechanical adherence of the CNT films needs to be improved. In this study, it was shown that the corrosion rate decreased from 987 μm/yr to 16 μm/yr in the presence of synthetic seawater. Yet, further improvements need to be made for commercial use.

APPENDIX

SAMPLE MATHCAD CODE FOR CURVE FITTING OF BARE STEEL

$f := 1, 2 .. 100000$

$j := \sqrt{-1}$

$Rs := 3.69 \cdot 10^4 \qquad Rp := 57.5 \cdot 10^4 \qquad Rpore := 55.71 \cdot 10^4$

$Cdl := 3.21 \cdot 10^{-9} \qquad Cc := 4.5 \cdot 10^{-11}$

$$Z1(f) := \frac{Rp}{1 + j \cdot 2 \cdot \pi \cdot f \cdot Cdl \cdot Rp}$$

$$Z(f) := Rs + \frac{Rpore + Z1(f)}{1 + j \cdot 2 \cdot \pi \cdot f \cdot Cc \cdot (Rpore + Z1(f))} \qquad \Phi(f) := atan\left(\frac{Im(Z(f))}{Re(Z(f))}\right) \cdot \frac{180}{\pi}$$

$$Zadj(f) := \sqrt{(Re(Z(f)) - Rs)^2 + Im(Z(f))^2} \qquad \Phi adj(f) := atan\left(\frac{Im(Z(f))}{Re(Z(f)) - Rs}\right) \cdot \frac{180}{\pi}$$

$$sumoferrorZ := \left[\sum_{i=0}^{58} \left(Zexpt_i - Zadj\left(fexpt_i\right)\right)^2\right]$$

$$sumoferror\Phi := \left[\sum_{i=0}^{58} \left(\Phi expt_i - \Phi adj\left(fexpt_i\right)\right)^2\right]$$

$sumoferrorZ = 1.383 \times 10^{11} \qquad sumoferror\Phi = 193.732$

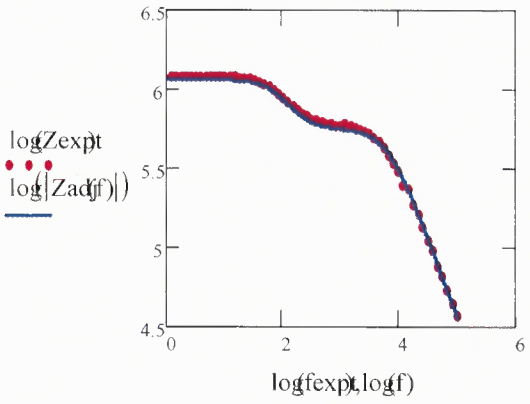

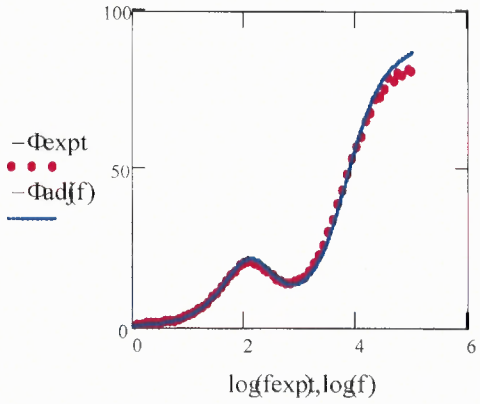

REFERENCES

1. Uhlig, H. H., Corrosion and Corrosion Control: An introduction to corrosion science and engineering, John Wiley and Sons Inc., 1971.
2. http://events.nace.org/publicaffairs/images_cocorr/ccsupp.pdf.
3. McKetta Jr, J. J., McKetta, J. J., Cunningham, W. A., *Encyclopedia of chemical processing and design*, volume 12, CRC Press, 1981.
4. Applegate, L. M., Cathodic Protection, McGraw-Hill, New York, 1960.
5. Morgan, J. H., Cathodic Protection, Hill, London, 1959.
6. Edeleanu, C., Metallurgia, 50, 113 (1954).
7. Dubois, N. A., "Protection of iron and steel by paint films", *The journal of industrial and engineering chemistry*, volume 5, number 12, 1913.
8. "A substitute of galvanized iron", *The journal of industrial and engineering chemistry*, volume 6, number 8, 1914.
9. Sudrabin, L. P., and Marks, H. C., "Cathodic protection of steel in contact with water", *The journal of industrial and engineering chemistry*, volume 44, number 8, 1952.
10. Ahmad, N. and MacDiarmid, A. G., "Inhibition of corrosion of steels with the exploitation of conducting polymers", *Synthetic metals*, number 78, pp. 103-110, 1996.
11. Fujimoto, S. and Tsuchiya, H., "Semiconductor properties and protective role of passive films of iron base alloys", *Corrosion Science* number 49, pp. 195-202, 2007.
12. Iijima, S., "Helical microtubules of graphitic carbon", *Nature*, number 354, pp. 56-58, 1991.
13. Dresselhaus, M. G., Dresselhaus, Eklund, P., Saito, R., "Carbon nanotubes", *Physics world*, January 1998.
14. http://physicsweb.org/articles/world/11/1/9/1#world-11-1-9-2 (08/2009).
15. Lee, J.U., Gipp, P. P., and Heller, C. M., *Applied Physics Letters* , volume 85, number 1, 5 July 2004.
16. Pumera, M., "Electrochemistry of carbon nanotubes", *Chemistry A European journal,* 2009.
17. Day, T. M., Watson, N. R., and Macpherson, J. V., "Electrochemical and conductivity measurements of single-wall carbon nanotube network electrodes", *Journal of American Chemical Society*, number 126, volume 51, pp. 16724- 16725, 2004.
18. Wang, J., Li, M., Shi, Z., Li, Q., and Gu, Z., "Direct electrochemistry of cytochrome c at a glassy carbon electrode modified with single wall carbon nanotubes", *Anal. Chem.*, volume 74, number 9, pp. 1993-1997, 2002.

19. Valentini, F., Amine, A., Orlanducci, S., Terranova, M. L. and Palleschi, G., "Carbon nanotube purification: preparation and characterization of carbon nanotube paste electrodes", *Anal. Chem.*, volume 75 number 20, pp. 5413-5421, 2003.

20. Zeng, Z., Yu, Y. and Zhang, J., "Electrochemical corrosion behavior of carbon nanotube doped hard chromium coatings electrodeposited from Cr (III) baths", *Journal of the electrochemical society*, volume 156, number 4, pp. C123-C126, 2009.

21. Principles of semiconductor devices, B.V. Zeghbroeck, 2004.

22. Lan, A., Iqbal, Z., Aitouchen, A., Libera, M. and. Grebel, H., "Growth of single-wall carbon nanotubes within an ordered array of nanosize silica spheres", *Applied Physics Letters*, volume. 81, number 3, 2002.

23. O'Connell, M. J., Boul, P., Ericson, L. M., Huffman, C., Wang, Y., Haroz, E., Kuper, C., Tour, J., Ausman, K. D. and Smalley, R. E., "Reversible water-solubilization of single-walled carbon nanotubes by polymer wrapping", *Chemical Physics Letters,* volume 342, issue 3-4, pp. 265-271, 2001.

24. Shim, M., Javey, A., Kam, N. W. S. and Dai, H., "Non-covalent Sidewall Functionalization of Single-walled Carbon Nanotubes for Protein Immobilization", *Journal of American Chemical Soceity.,* volume 123, article 11512, 2001.

25. Rouff, R.F. and Lorents, D.C., *Carbon*, volume 33, number 7, pp. 925-930, 1995.

26. Choi, W. B., Jin, Y. W., Kim, H. Y., Lee, S. J., Yun, M. J., Kang, J. H., Choi, Y. S., Park, N. S., Lee, N. S. and Kim, J. M., "Electrophoresis deposition of carbon nanotubes for triode-type field emission display", *Applied Physics Letters,* volume 78, number 11, 2001.

27. Lee, J.U., Gipp, P. P., and Heller, C. M., "Carbon nanotube p-n junction diodes", *Applied Physics Letters,* volume 85, number 1, 2004.

28. Liu, J., Rinzler, A. G., Dai, H., Hafner, J. H., Bradley, R. K, Boul, P. J., Lu, A., Iverson, T., Shelimov, K., Huffman, C. B., Rodriguez-Macias, F., Shon, Y., Lee, T. R., Colbert, D. T. and Smalley, R. E., "Fullerene pipes", *Science,* volume 280, pp. 1253-1256, 1998.

29. Qi, P., Vermesh, O., Grecu, M., Javey, A., Wang, Q., Dai, H., Peng, S. and Cho, K.J., "Toward large arrays of multiplex functionalized carbon nanotube sensors for highly sensitive and selective molecular detection" *Nano Letters,* volume 3, number 3, pp. 347-351, 2003.

30. Arnold, M.S., Sharping, J.E., Stupp, S.I., Kumar, P. and Hersam, M.C.," Band Gap Photobleaching in Isolated Single-Walled Carbon Nanotubes", *Nano Letters,* volume 3, number 11, pp. 1549-1554, 2003.

31. O'Connell, M. J., Boul, P., Ericson, L. M., Huffman, C., Wang, Y., Haroz, E., Kuper, C., Tour, J., Ausman, K. D. and Smalley, R. E., "Reversible water-solubilization of single-walled carbon nanotubes by polymer wrapping", *Chemical Physics letters,* volume 342, pp. 265-271, 2001.

32. Benoit, J-M, Corraze, B., Lefrant, S., Blau, W. J., Bernier, P. and Chauvet, O., 'Transport properties of PMMA-carbon nanotubes composites', *Synthetic metals*, volume 121, pp. 1215-1216, 2001.

33. Thompson, N. G. and Payer, J. H., Corrosion testing made easy: DC electrochemical test methods, NACE international, Huston, TX, 1998.

34. Electrochemistry Encyclopedia, http://electrochem.cwru.edu/ed/encycl/ (08/2009).

35. Lowe, A. M., "Estimation of electrochemical noise impedance and corrosion rates from electrochemical noise measurements", Curtin university of technology thesis, 2002.

36. Barsoukov, E. and Macdonald, J. R., Impedance spectroscopy: Theory, experiment and applications, Wiley-interscience, Hoboken, NJ, 2005.

37. Orazem, M. E. and Tribollet, B., Electrochemical impedance spectroscopy, John Wiley and sons, inc, Hoboken, NJ, 2008.

38. http://www.gamry.com/App_Notes/EIS_Primer/EIS_Primer.htm (08/2009).

39. Jeffrey Snyder, G. and Toberer, E. S., "Complex Thermoelectric Materials", *Nature Materials*, volume 7, pp. 105-114, 2008.

40. Mirza, S. M. and Grebel, H., "Thermoelectric properties of aligned carbon nanotubes", *Applied physics letters*, volume 92, issue 20, 2008.

41. Jorio, A., Pimenta, M.A., Souza Filho, A.G., Saito, R., Dresselhaus, G. and Dresselhaus, M.S., *New Journal of Physics*, volume 5, number 139, pp. 1-17, 2003.

42. Zhang, Y. and Grebel, H., "Controlling ionic currents with transistor-like structures", *ECS Transactions,* volume 2, number 18, pp. 1-18, 2007.

43. Sreevatsa, S., Zhang, Y. and Grebel, H., "Corrosion protection with transistor-like structures", *ECS Transactions,* volume 13, number 27, pp. 115-122, 2008.

44. Jorio, A., Souza Filho, A. G., Dresselhaus, G., Dresselhaus, M. S., Swan, A. K., Unlu, M. S., Goldberg, B. B., Pimenta, M. A., Hafner, J. H., Lieber, C. M. and Saito, R., "*G*-band resonant Raman study of 62 isolated single-wall carbon nanotubes", *Physical Review B*, volume 65, article 155412, 2002.

45. Montemor, M.F., Rosqvist, A., Fagerholm, H. and Ferreira, M.G.S., "A comparative study on the corrosion resistance of AA2024-T3 substrates pre-treated with different silane solutions: Composition of the films formed", *Progress in Organic coatings,* volume 51, issue 3, pp. 188-194, 2004.

46. Walaszkowski, J., Orlikowski, J. and Juchniewicz, R., "Electrochemical investigations of conducting polymer composites for cathodic protection-II", *Corrosion Science*, volume 37, number 4, pp. 645-655, 1995.

47. Scully, J. R., Silverman, D. C. and Kendig, M. W., Electrochemical Impedance: Analysis and Interpretation, ASTM publication, 1993.

48. Bard, A. J. and Faulkner, L. R., Electrochemical Methods: Fundamentals and Applications, John Wiley and Sons, 1980.

49. Orazem, M. E., Pebere, N. and Tribollet, B., "Enhanced graphical representation of electrochemical impedance date", *Journal of the Electrochemical society*, volume 153, number 4, pp. B129-B136, 2006.

50. Harrington, S. P. and Devine, T. M., "Relation Between the Semiconducting Properties of a Passive Film and Reduction Reaction Rates", *Journal of The Electrochemical Society,* volume 156, number 4, pp. C154-C159, 2009.

51. Bonora, P. L., Defloriana, F. and Fedrizzi, L., "Electrochemical impedance spectroscopy as a tool for investigating underpaint corrosion", *Electrochimica Acta* , volume 41, numbers 7/8, pp. 1073-1082, 1996.

52. Covington, A.K., "Terminology and conventions for microelectronic ion-selective field effect transistor devices in electrochemistry", *Pure & Applied Chemistry,* volume 66, pp 565, 1994.

53. Banerjee, A. and Grebel, H., "Free standing graphene and its applications", *ECS Transactions*, volume 19, number 5, pp 53-65, 2009.

54. Banerjee, A. and Grebel, H., "Depositing graphene films on solid and perforated substrates", *Nanotechnology*, volume 19, number 365303, 2008.

55. Zheng, M., Jagota, A., Semke, E. D., Diner, B. A., Mclean, R. S., Lustig, S. R., Richardson, R. E. and Tassi, N. G., "DNA-assisted dispersion and separation of carbon nanotubes", *nature materials*, volume 2, May 2003.

56. Davis, J. R., Corrosion: understanding the basics, ASM international, Materials park, OH, 2003.

57. Kavan, L. and Dunsch, L., "Chapter: Electrochemistry of Carbon Nanotubes", edited by Jorio, A., Dresselhaus, G., and Dresselhaus, M.S., Topics in Applied Physics: Carbon Nanotubes, volume 111, pp. 567–603, Springer-Verlag Berlin Heidelberg, 2008.

58. Cao, X. A., Dang, G. T., Zhang, A. P., Ren, F., Abernathy, C. R., Pearton, S. J., Van Hove, J. M., Klaassen, J. J., Polley, C. J., Wowchack, A. M., Chow, P. P., King, D. J. and Chuc, S. N. G., "Common-Base Operation of GaN Bipolar Junction Transistors", *Electrochemical and Solid-State Letters,* volume 3, number 7, pp. 333-334, 2000.

59. Nilsson, D., Kugler, T., Svensson, P., and Berggren, M., "An all-organic sensor-transistor based on a novel electrochemical transducer concept printed electrochemical sensors on paper", *Sensors and Actuators B,* volume 86, pp. 193-197, 2002.

60. Tan, C. K. and Blackwood, D. J., "Corrosion protection by multilayered conducting polymer coatings", *Corrosion Science*, volume 45, issue 3, pp. 545-557, 2002.

61. Chandra, D. and Daemen, J., *Quarterly technical report no.11*, Task No: ORD-FY04-019 and Document No: SIP-UNR-040 (2007).

62. Wagner, C., "Contribution to the Theory of Cathodic Protection, II", *Journal of electrochemical society,* volume 104, pp. 631-637, 1957.

63. Ateya, B. G. and Pickering, H. W., "On the Nature of Electrochemical Reactions at a Crack Tip during Hydrogen Charging of a Metal", *Journal of electrochemical society*, volume 122, pp. 1018-1026, 1975.

64. Sathiyanarayanan, S., Jeyaram, R., Muthukrishnan, S. and Venkatachari, G., "Corrosion Protection Mechanism of Polyaniline Blended Organic Coating on Steel", *Journal of electrochemical society*, volume 156, pp. C127-C134, 2009.

65. Scully, J. R., "Electrochemical Impedance of Organic-Coated Steel: Correlation of Impedance Parameters with Long-Term Coating Deterioration", *Journal of electrochemical society*, volume 136, number 4, pp. 979-990, 1989.